From Finite Fault Slip to Seismic Moment Tensor: Simulating Induced Earthquakes in Groningen

Ruan, J.

DOI
10.4233/uuid:0bc78ed8-ce42-4bd6-a08f-17745b3bb2bb

Publication date
2025

Document Version
Final published version

Citation (APA)
Ruan, J. (2025). *From Finite Fault Slip to Seismic Moment Tensor: Simulating Induced Earthquakes in Groningen*. [Dissertation (TU Delft), Delft University of Technology]. https://doi.org/10.4233/uuid:0bc78ed8-ce42-4bd6-a08f-17745b3bb2bb

FROM FINITE FAULT SLIP TO SEISMIC MOMENT TENSOR: SIMULATING INDUCED EARTHQUAKES IN GRONINGEN

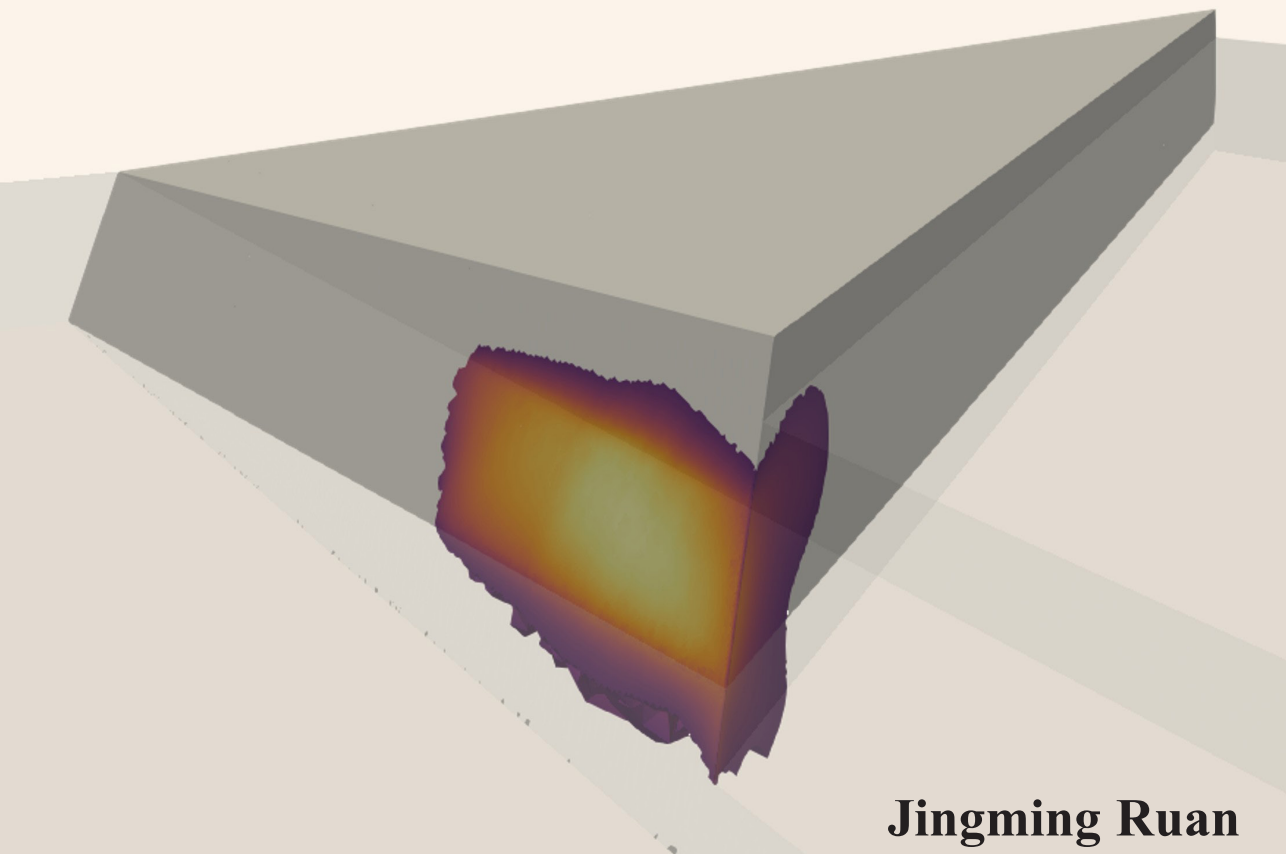

Jingming Ruan

From Finite Fault Slip To Seismic Moment Tensor: Simulating Induced Earthquakes In Groningen

From Finite Fault Slip To Seismic Moment Tensor: Simulating Induced Earthquakes In Groningen

Dissertation

for the purpose of obtaining the degree of doctor
at Delft University of Technology
by the authority of the Rector Magnificus, prof. dr. ir. T.H.J.J. van der Hagen,
chair of the Board for Doctorates
to be defended publicly on 3 December 2025 at 12:30

by

Jingming Ruan

Master of Science in Earth Structures and Dynamics, Utrecht University,
born in Guangdong, China.

This dissertation has been approved by the promotors.

Composition of the doctoral committee:

Rector Magnificus,	chairperson
Dr. R. Ghose	Delft University of Technology, promotor
Em. Prof. dr. W. A. Mulder	Delft University of Technology, promotor
Independent members:	
Prof. dr. ir. M.B. van Gijzen	Delft University of Technology
Em. Prof. dr. ir. J.D. Jansen	Delft University of Technology
Em. Prof. dr. ir. C.P.A. Wapenaar	Delft University of Technology
Prof. dr. M. van der Meijde	University of Twente
Dr. L. Buijze	TNO
Prof. dr. S. Geiger	Delft University of Technology, reserve member

This research was part of the "DeepImage" project, funded by NWO Science domain (NWO-ENW), project DEEP.NL.2018.048.

Keywords: Geomechanics, induced seismicity, numerical modelling, finite-element method, finite-difference method, seismic-moment-tensor inversion

ISBN 000-00-0000-000-0

An electronic version of this dissertation is available at
http://repository.tudelft.nl/.

致我的父母
To my parents

CONTENTS

SUMMARY

This thesis investigates the mechanism of an induced earthquake associated with subsurface reservoir depletion, focusing on numerical simulations that incorporate the real-world reservoir geometry of the Groningen gas field in the Netherlands. It begins with a review of the poroelastic theory and its relevance to stress changes induced by reservoir depletion. The study then examines how fault offset and three-dimensional structural complexities, particularly fault intersections and horst formations, influence stress localisation and fault reactivation. While earlier studies typically consider a single fault in simplified reservoir settings, this work demonstrates that accurate modelling of the full 3-D fault system is critical for capturing realistic rupture behaviour of induced earthquakes.

To quantify these effects, we perform 3-D geomechanical simulations incorporating a faulted reservoir model based on the Groningen field, including two intersecting faults and the resulting horst structure. The study specifically focuses on the 2018 M_L 3.4 Zeerijp earthquake, using numerical simulations to calculate the stress evolution over the reservoir's production history and the fault slip during the induced earthquake. Synthetic seismic data are generated and benchmarked against field observations, including event magnitude, depletion level at reactivation, waveforms and the inverted focal mechanism.

The results demonstrate that the fault intersection angle influences not only the depletion level required for reactivation, but also the location of the slip initiation and the resulting rupture pattern. In the subsequent simulation of the 2018 Zeerijp earthquake, we observed a rupture pattern consistent with that seen in the sensitivity study for a similar intersection angle. The model also reproduces similar depletion levels, local magnitude, waveform characteristics, and focal mechanisms. These results demonstrate that current poroelastic models, when combined with realistic geological and structural representations, are capable of capturing key features of induced seismicity.

We also investigate the relationship between the inferred hypocentre location and the frequency content of the input waveforms used in inversion. This analysis is based on the simulated rupture of the 2018 Zeerijp earthquake, using both synthetic and field-observed waveforms. We observe that the estimated hypocentre shifts from the centre of the slip patch to the initial slip area when higher frequency components are included. This shift is attributed to the fact that faster slip during the rupture generates higher frequency seismic waves, a behaviour previously observed in large tectonic earthquakes. Our results show that this effect is also detectable in moderate-magnitude induced events, suggesting the potential of frequency-dependent waveform analysis to resolve rupture histories and source dynamics of reservoir-depletion-induced earthquakes.

SAMENVATTING

Dit proefschrift onderzoekt het mechanisme van een geïnduceerde aardbeving als gevolg van drukverlaging in een ondergronds reservoir, met de nadruk op numerieke simulaties waarin de realistische reservoirgeometrie van het Groningse gasveld in Nederland is opgenomen. Het begint met een bespreking van de poro-elasticiteitstheorie en de relevantie daarvan voor spanningsveranderingen door reservoirdepletie. Vervolgens wordt onderzocht hoe breukverschuivingen en driedimensionale structurele complexiteiten—met name breukintersecties en horststructuren—de spanningslokalisatie en breukreactivering beïnvloeden. Waar eerdere studies vaak uitgaan van een enkele breuk in een vereenvoudigde context, laat dit werk zien dat een nauwkeurige modellering van het volledige 3D-breuksysteem cruciaal is voor het realistisch simuleren van het breukgedrag bij geïnduceerde aardbevingen.

Om deze effecten te kwantificeren, voeren we 3D-geomechanische simulaties uit met een gemodelleerd reservoir gebaseerd op het Groningenveld, inclusief twee kruisende breuken en de resulterende horststructuur. De studie richt zich specifiek op de M_L 3,4 aardbeving bij Zeerijp in 2018. We berekenen de spanningsontwikkeling gedurende de productiegeschiedenis van het reservoir en de breukslip tijdens deze geïnduceerde aardbeving. Synthetische seismische data worden gegenereerd en vergeleken met veldwaarnemingen, waaronder de gemeten magnitude, het depletieniveau bij reactivering, golfvormen en de geïnverteerde focale mechaniek.

De resultaten tonen aan dat de intersectiehoek tussen de breuken niet alleen het benodigde drukverlies voor reactivering beïnvloedt, maar ook de locatie van de slipinitiatie en het resulterende breukpatroon. In de simulatie van de Zeerijp-aardbeving van 2018 zien we een breukpatroon dat overeenkomt met dat in de gevoeligheidsstudie voor een vergelijkbare intersectiehoek. Het model reproduceert bovendien vergelijkbare depletieniveaus, lokale magnitude, golfvormkarakteristieken en focale mechanismen. Deze bevindingen tonen aan dat poro-elastische modellen, wanneer ze worden gecombineerd met realistische geologische en structurele invoer, in staat zijn om belangrijke kenmerken van geïnduceerde seismiciteit vast te leggen.

We onderzoeken ook de relatie tussen de afgeleide hypocentrumlocatie en de frequentie-inhoud van de seismische golfvormen die in inversie worden gebruikt. Deze analyse is gebaseerd op de gesimuleerde breuk van de Zeerijp-aardbeving van 2018, met zowel synthetische als veldgemeten golfvormen. We zien dat het geschatte hypocentrum verschuift van het centrum van het slipgebied naar de initiële slipzone wanneer hogere frequentiecomponenten worden meegenomen. Deze verschuiving is te verklaren door het feit dat snellere slip tijdens de breuk hogere frequenties genereert—een gedrag dat eerder is waargenomen bij grote tektonische aardbevingen. Onze resultaten tonen aan dat dit effect ook detecteerbaar is bij geïnduceerde aardbevingen van gematigde sterkte, wat wijst op het potentieel van frequentie-afhankelijke golfvormanalyse om de breukgeschiedenis en bronmechanismen van aardbevingen door reservoirdepletie beter te begrijpen.

1

INTRODUCTION

1

1.1. INDUCED SEISMICITY IN GRONINGEN

The Groningen gas field, located in the Netherlands, is one of the largest natural gas fields in Western Europe. Discovered in 1959, gas production began in 1963. Over the decades, continuous extraction has led to a significant drop in the reservoir's pore pressure. Induced seismicity was first recorded in the Groningen region in 1991. Since then, the frequency and magnitude of these earthquakes have increased, correlating with ongoing gas production activities.

Induced seismicity is not limited to underground gas production; it has been observed worldwide in association with various subsurface activities. Arguably, the largest known M 6.3 induced earthquake occurred in the Koyna-Warna region of India on December 1967 due to impoundment of a water reservoir. In the 5 decades since water impoundment, more than 100,000 earthquakes of M 1.0 – 6.3 occurred in this region (Das and Mallik, 2020). For a recent example, waste-water injection in Oklahoma has led to a significant increase in seismic activity in the region, with recorded earthquakes rising from fewer than two per year before 2008 to hundreds annually in subsequent years (Hincks et al., 2018). Similarly, hydraulic injection by the Pohang Enhanced Geothermal System triggered a significant earthquake of magnitude 5.5 in 2017 in Pohang, South Korea (Woo et al., 2019).

The induced seismic events have caused substantial damage in the region of Groningen gas field, affecting numerous local buildings and infrastructure. By 2024, over 3,300 buildings in Groningen had to be demolished after suffering from the earthquake damage. The damage led to the decision by the Dutch government to reduce and stop the gas extraction. Moreover, a large sum of money was spent by numerous committees, advisory boards, and the government, paid by NAM (Nederlandse Aardolie Maatschappij), to reinforce the buildings in the region. Most importantly, the induced seismicity in Groningen causes significant social and individual impacts to the local residents, as well as to the political situation in the Netherlands. Additionally, the government had to allocate €22 billion over the next 30 years to repair and reinforce the buildings in the region.

As the Netherlands and most of the world aim for carbon neutrality by 2050, cleaner energy sources such as geothermal and hydrogen are gaining momentum in the global energy market. However, these emerging energy technologies often rely on subsurface reservoirs, involving geothermal injection and extraction, hydrogen storage, and CO_2 sequestration. These applications alter underground pressures and can potentially induce earthquakes, similar to the effects observed in underground gas extraction.

It is vital to learn from the induced seismicity in the Groningen gas field in order to avoid similar issues in future underground reservoir applications. Numerous studies, both theoretical and numerical, have been conducted to investigate the causes of the induced seismicity in Groningen.

One of the primary contributors to seismic activity in the Groningen region is the poroelastic stress from the depleted reservoir, along with reservoir offset along the faults (Buijze et al., 2019; Candela et al., 2019; Jansen & Meulenbroek, 2022). In addition to these linear effects, nonlinear processes—such as reservoir creep and shrinkage—are critical for explaining the time-dependent nature of the induced seismicity.

1.2. POROELASTIC STRESS AND FAULT OFFSET

Poroelastic stress due to gas reservoir depletion is the main contributor for induced seismicity in the Groningen region. Both effective horizontal and vertical stresses change due to pore-pressure changes caused by gas extraction. This relationship can be explained by linear poroelasticity (Biot, 1941).

For a laterally extensive reservoir overlain by a homogeneous, flat layer of overburden, the vertical total stress is typically assumed constant and governed by the weight of the overburden. Under this assumption, Engelder and Fischer (1994) derived the expression for the incremental horizontal stress resulting from changes in pore pressure, based on the theory of linear poroelasticity (Biot, 1941). The relationship is given by:

$$\frac{\Delta\sigma_h}{\Delta P} = \alpha \frac{1-2\nu}{1-\nu}, \tag{1.1}$$

where α is the Biot-Willis coefficient and ν is Poisson's ratio. $\Delta\sigma_h$ is the incremental horizontal stress. ΔP is the incremental pore pressure. From this, the corresponding change in effective horizontal stress is:

$$\Delta\sigma'_h = \Delta\sigma_h - \alpha\,\Delta P = -\alpha \frac{\nu}{1-\nu}\Delta P, \tag{1.2}$$

assuming no change in vertical total stress ($\Delta\sigma_v = 0$). Similarly, the change in effective vertical stress is:

$$\Delta\sigma'_v = \Delta\sigma_v - \alpha\,\Delta P = -\alpha\,\Delta P. \tag{1.3}$$

The difference between the vertical and horizontal effective stresses is therefore:

$$\Delta\sigma'_v - \Delta\sigma'_h = -\alpha\,\Delta P \frac{1-2\nu}{1-\nu}. \tag{1.4}$$

Since $\Delta P < 0$ during fluid extraction, this difference increases with continued depletion, leading to a growing differential stress. As the differential stress increases, the Mohr circle—which represents the stress state on a fault—expands and may eventually reach the failure envelope defined by the Mohr–Coulomb criterion. Once this envelope is reached, fault slip is likely to occur, potentially resulting in a seismic event.

Zbinden et al. (2017), Van den Bogert (2018), and Buijze et al. (2019) investigated the build-up of poroelastic stress in Groningen along faults within the reservoir interval caused by pore-pressure depletion. They also examined the subsequent seismic rupture triggered during these events. Their simulations highlighted the effects of stress concentration due to fault offsets in the reservoir. In a laterally extended reservoir with uniform reservoir depletion, the fault offset creates variation in the development of the aseismic slip patches. This results in different fault reactivation patterns during seismic events. Faults with offsets were found to trigger seismic ruptures at significantly lower levels of reservoir depletion compared to faults without offsets.

Additionally, Jansen and Meulenbroek (2022) explored the aseismic growth of slip patches and nucleation length (Uenishi & Rice, 2003). They also provided an analytical description of the incremental stress field as induced by uniform reservoir depletion at displaced faults.

1.3. SEISMIC OBSERVATION AND GEOMECHANICAL MODEL

Numerous studies were conducted to investigate the focal mechanisms of the induced earthquakes in the Groningen region. Moment-tensor inversion is a widely used method to analyse the earthquake focal mechanisms based on seismic observations. Several studies (Li et al., 2016; Spetzler & Dost, 2017; Willacy et al., 2019) assumed a fixed depth of 3000 m for the earthquakes in their inversion. Others utilized advanced techniques combining 3-D seismic velocity models, probabilistic methods, and full waveform inversion (Dost et al., 2020; Masfara & Weemstra, 2024; Masfara et al., 2022) to estimate the depth of the hypocentre.

These studies consistently concluded that the event locations strongly correlate with the major faults in the Groningen reservoir. Additionally, the double-couple (DC) component of the source mechanisms generally aligns with the fault orientation and explains the normal faulting. However, the largest source of error in earthquake locations is associated with inaccuracies in the depth estimation. While the hypocentre locations are quite accurate in latitude and longitude, their depth accuracy is limited. This discrepancy arises from the dense lateral distribution of seismic receivers in the region, but a lack of deep borehole receivers.

Seismic moment-tensor inversion offers valuable insights into the rupture mechanism by fitting the observed seismic waveforms with the synthetic ones. However, this approach has its own limitations, as it cannot capture the full rupture process from the initiation to the conclusion of a seismic event. Additionally, it does not provide an explanation of the causal relationship between gas production and the resulting induced seismicity.

Physical models, such as geomechanical models, on the other hand, take into account the stress history from the gas production records and the dynamic stress changes during the seismic event. By creating a geomechanical model based on the underground reservoir model (NAM, 2020), induced seismicity was simulated by Wentinck (2018).

1.4. RESEARCH OBJECTIVES

From past research, we can have a clear understanding of the factors that contribute to induced earthquakes in Groningen, such as poroelastic stresses and the reservoir displacement at the fault. However, our current knowledge remains insufficient for fully explaining and predicting the induced seismicity, highlighting the need for further investigation. To validate previous findings on induced seismicity in the Groningen region and to address the gaps in our understanding, it is necessary to conduct numerical simulations of past induced earthquakes.

This thesis focuses on applying prior insights to actual induced seismic events in the Groningen gas field, particularly the M_L 3.4 Zeerijp earthquake of 2018. The objectives of this research are:

1. To implement and validate an established underground reservoir model within a geomechanical simulation framework tailored to the Zeerijp area. The target is to simulate the stress evolution on the main fault from the onset of production up to the occurrence of the main event and derive the relative slip on the fault, along with synthetic seismic data at borehole receivers near the hypocentre.

2. To compare our simulation results with field observations, including event magnitude, depletion values at triggering, seismograms, and hypocentre locations, in order to gain comprehensive insights into the occurrence of induced earthquakes in the Groningen region.

3. To benchmark the centroid moment-tensor inversion using synthetic seismograms, validating our approach by comparing the results with those from KNMI (1993) and Dost et al. (2020).

The overarching goal is to improve the feasibility of simulating reservoir-depletion-induced earthquakes while satisfying the field observations.

1.5. THESIS OUTLINE

To address the research objectives, the thesis is organized into the following chapters.

Chapter 2 explores the effect of a 3-D reservoir structure—a horst structure formed by two intersecting faults—on induced seismicity. Building on the prior understanding of how reservoir offset impacts the induced stress field and the dynamic rupture behaviour, we extend the analysis to 3-D geomechanical simulations including more realistic conditions. Our findings are validated through a simulation of the 2018 M_L 3.4 Zeerijp event using a detailed 3-D underground reservoir model.

Chapter 3 investigates whether the fault intersections can lead to the migration of rupture from a primary fault to a secondary fault during the induced earthquake. We adapt the crosslink constraint method to simulate the rupture propagation mechanics at the fault intersection. This approach is tested and validated also using the 2018 M_L 3.4 Zeerijp event.

Chapter 4 concentrates on simulating the seismic waves generated by the geomechanically modelled rupture at Zeerijp. The results are verified against field seismic observations for the 2018 M_L 3.4 event. Additionally, seismic moment-tensor inversion is performed using both synthetic and field-observed seismograms at seven nearby borehole receivers that are positioned at a depth of 200 m. This leads to further validation of our Zeerijp geomechanical model.

Chapter 5 explores the correlation between hypocentre distribution derived from the probabilistic moment-tensor inversion and the dynamic rupture process. Waveform fitting is performed employing various filters with different upper frequencies in order to evaluate this relationship. The correlation is analysed using synthetic data, followed by validation using field-observed seismic data.

In Chapter 6 we summarize our key findings, highlighting the importance of incorporating 3-D reservoir geometry in assessing the risks caused by induced earthquakes. This chapter also discusses the prospects of advancing our understanding of the underground rupture processes through new developments based on the results achieved in this research.

2

3-D GEOMECHANICAL MODELLING OF INDUCED SEISMIC SLIP CONSIDERING A REALISTIC 3-D RESERVOIR GEOMETRY WITH INTERSECTING FAULTS

Geomechanical simulations of induced seismicity generally involve a simple 2-D reservoir geometry in terms of reservoir structure and fault distribution. The depletion of the reservoir controls the incremental stress field. The geometry of the reservoir has a substantial influence on the occurrence of induced earthquakes. We develop geomechanical models based on realistic, 3-D geological structure of the reservoir in the Groningen gas field. The model captures the main characteristics of the reservoir structures in the Zeerijp region. Through quasi-static and dynamic simulations, we observe that a smaller intersection angle between the two normal faults in the Zeerijp region causes an increase in the incremental Coulomb stress at the lower reservoir juxtaposition adjacent to the intersection. As a result, this intersection angle strongly affects the location of the initial seismic slip, the rupture pattern, and the location of the maximum slip. Our simulation produces an earthquake of magnitude M_W 3.0, due to fault reactivation occurring at a reservoir depletion value of 26 *MPa. These values are consistent with those observed for the 2018 Zeerijp earthquake ($M_L = 3.4$), considering that M_W and M_L are approximately equal for events with $M_W > 2$ in Groningen. The location of the simulated rupture is close to the inverted hypocentre location for the 2018 earthquake. Our results suggest that it is crucial to incorporate realistic, 3-D reservoir structures when simulating induced seismicity in a specific region.*

Parts of this chapter have been submitted as a journal article and published as a preprint in Ruan et al. (2023).

2.1. INTRODUCTION

Earthquakes are sometimes caused by human activities, such as fluid extraction from or injection into the subsurface, inducing changes in the reservoir properties including changes in pore pressure that cause various mechanical responses in the reservoir and its surroundings. Production activities in a region with pre-existing faults can reactivate those faults and generate earthquakes. There are various physical processes behind induced seismicity. In Groningen, the Netherlands, gas production is considered to be the main cause. There are numerous studies involving laboratory experiments on the frictional behaviour of faults (Hunfeld et al., 2017) and numerical modelling based on geomechanics (Buijze et al., 2019; DeDontney & Lele, 2018; Van den Bogert, 2018; Van Wees et al., 2017), which try to explain the physical processes behind the induced seismicity in the Groningen region.

Kühn et al. (2022) reviewed several source models, including statistical and physical models, in order to investigate the cause of the induced seismicity in Groningen. Geomechanical simulation is widely used to investigate the physical process behind induced seismicity. The pore-pressure variation in the reservoir induces poroelastic stress which, according to the Mohr-Coulomb theory, promotes the failure of the fractures in the reservoir. Apart from the poroelastic stress, the differential compaction due to faults with non-zero offset can concentrate the incremental stresses caused by reservoir depletion, including shear stress and normal stress. This effect has been observed in numerical modelling by Van den Bogert (2018) and Buijze et al. (2019). Jansen and Meulenbroek (2022) derived an analytical expression for a homogeneous medium.

In general, a simple 2-D or 3-D geometry has been used in most earlier geomechanical simulations of induced earthquakes in Groningen. These simulations essentially consider a horizontally-layered model with zero- or non-zero fault offsets. The effect of more realistic, 3-D reservoir geometry on the generated induced earthquakes has been mostly ignored. One of the main features of the reservoir geometry is the fault system. Since faults, in general, occur as parts of a fault system, the reservoir is split by the fault system into multiple compartments, with fault offsets in the reservoir interval. Most earlier modelling studies on incremental stress fields in a depleted reservoir consider only reservoir compartments formed by a single fault with a non-zero offset. Such simple geometrical assumptions neglect the effect of fault intersection and the distribution of reservoir compartments. Maerten et al. (1999) numerically computed the irregular slip distributions caused by the interaction between the intersecting faults. The results were confirmed by seismic surveys and sandbox experiments. In this research, our goal is to gain insights into the relationship between fault intersection and the induced seismicity caused by reservoir depletion.

This chapter is structured as follows. In Section 2.2 we will first introduce the workflow of our simulation of induced earthquakes and the governing equations in each stage. We will discuss the methods involved in model construction, such as mesh design (geometry), discretization, boundary conditions, and assignment of material/fault parameters. In Section 2.3, we will present the 2-D models used for benchmarking, with and without an offset at the reservoir. In Section 2.4, we will illustrate the design of 3-D models. The results on three-block models considering different intersection angles between the two normal faults will be presented, primarily focusing on the induced

stress field and the dynamic rupture patterns. In Section 2.5, we will show how we constructed a realistic 3-D model of the reservoir geometry in the Zeerijp region located in the Groningen province. The relevance of this model to simulate the 2018 M_L 3.4 Zeerijp earthquake will be discussed. Section 2.6 will summarize our findings.

2.2. NUMERICAL SIMULATION AND MODEL SETUP

To simulate the induced seismicity in the Groningen gas field, we consider the poroelastic problem of reservoir compaction due to gas extraction, where the strain field is coupled with the pore-pressure field. For numerical simulations, the finite-element method (FEM) is widely used for stress and strain analyses in continuum mechanics. We have adapted the open-source finite-element code `Defmod` developed by Meng (2017) to simulate the strain, stress, and the resulting rupture at a uniformly depleted reservoir. `Defmod` is capable of both quasi-static and dynamic simulations, which are combined in our research to simulate the evolution of the induced seismicity. To investigate the effect of the fault intersection and the distribution of the reservoir compartments on induced seismicity, we develop a set of 3-D models with two intersecting normal faults and another realistic 3-D model based on the Petrel geological model of the Groningen gas field (NAM, 2020), concentrating on the Zeerijp reservoir geometry.

2.2.1. QUASI-STATIC LOADING

Gas extraction and the resulting pore-pressure change in a reservoir can be regarded as a gradual loading process. Therefore, during this slow process, the inertial force can be neglected. We apply quasi-static loading to simulate the incremental stress field at a depleted reservoir. The time step is set in the order of days, months or years for each iteration of the quasi-static simulation.

For quasi-static loading, `Defmod` considers a linear constitutive law applied to small-strain problems, and solves the (quasi-)static state of the linear system

$$\begin{aligned} \mathbf{K}_n \mathbf{U}_n &= \mathbf{F}_n \text{ (absolute)}, \\ \mathbf{K}_n \Delta\mathbf{U}_n &= \Delta\mathbf{F}_n \text{ (incremental)}, \end{aligned} \tag{2.1}$$

where $\mathbf{K}$ is the system stiffness matrix, $\mathbf{U}$ the solution vector, and $\mathbf{F}$ the nodal force including a fluid source. The subscript n is the time index. When solving a poroelastic problem such as reservoir depletion, the solution $\Delta\mathbf{U}_n$ includes the nodal displacement and pressure, where $\Delta\mathbf{U}_n = \left[\Delta\mathbf{u}_n, \Delta\mathbf{p}_n\right]^{\mathrm{T}}$.

When solving the poroelastic problem, the stiffness matrix $\mathbf{K}_n$ and the right-hand-side vector $\mathbf{F}_n$ are

$$\mathbf{K}_n = \begin{bmatrix} \mathbf{K}_e & \mathbf{H} \\ -\mathbf{H}^{\mathrm{T}} & \Delta t\,\mathbf{K}_c + \mathbf{S}_p \end{bmatrix}, \quad \mathbf{F}_n = \begin{bmatrix} \Delta\mathbf{f}_n \\ \mathbf{q}_n - \Delta t\,\mathbf{K}_c \mathbf{p}_{n-1} \end{bmatrix}, \tag{2.2}$$

with elastic stiffness matrix $\mathbf{K}_e$ depending on the elastic constants of the solid. The fluid stiffness matrix $\mathbf{K}_c$ depends on the fluid-flow conductivity. The coupling matrix $\mathbf{H}$ depends on Biot's coefficient and is responsible for coupling the displacement and the pressure fields. The storage matrix $\mathbf{S}_p$ depends on the compressibility and porosity of

the solid, as well as on the compressibility of the fluid. The solution of the system provides an equilibrium between the displacement and the pressure fields.

In this study, we consider a highly permeable reservoir located in a relatively small part of the area of interest. Therefore, during the simulation, we could assume uniform depletion in the reservoir and keep the pore pressure outside the reservoir the same as the initial hydrostatic pressure. To this end, unlike Meng (2017), we manually define $\Delta\mathbf{p}_n$ in equation (2.2), multiply it with the stiffness matrix $\mathbf{K}_n$, and move the result to the right-hand-side function $\Delta\mathbf{F}_n$. Then, the solution of the system provides the displacement field $\Delta\mathbf{u}_n$ caused by the assumed uniform depletion or by any manually assigned $\Delta\mathbf{p}_n$. In our case, the governing equation (2.2) becomes

$$\mathbf{K}_e\Delta\mathbf{u}_n = \Delta\mathbf{f}_n - \mathbf{H}\Delta\mathbf{p}_n. \tag{2.3}$$

With this assumption, the quasi-static time step $\Delta\mathbf{t}$ does not affect the simulation, as $\Delta\mathbf{t}$ as well as the terms for fluid flow are no longer present in the governing equation. The unknown $\Delta\mathbf{u}_n$ is now related to the imposed depletion $\Delta\mathbf{p}_n$.

In `Defmod`, the fault constraints are implemented via a Lagrange Multiplier (LM) capping method. For a model containing a fault, each node except the edge nodes of the fault is split into a node pair sharing the same coordinates. Then, the node pairs are assigned separately to the elements that contained the same fault node before the split, based on which side the elements are located—either the positive side or the negative side of the fault in relation to its normal vector. These constraints control the displacement and the pressure of the node pairs. As an example, Eq. (2.4) illustrates a locked and permeable fault by constraining tangential and normal displacements as well as the pressure on the split fault nodes:

$$\begin{bmatrix} n_x & n_z & 0 & -n_x & -n_z & 0 \\ t_x & t_z & 0 & -t_x & -t_z & 0 \\ 0 & 0 & 1 & 0 & 0 & -1 \end{bmatrix} \begin{bmatrix} u_x^{(+)} \\ u_z^{(+)} \\ p^{(+)} \\ u_x^{(-)} \\ u_z^{(-)} \\ p^{(-)} \end{bmatrix} = 0. \tag{2.4}$$

Here, $u_x^{(+)}$ and $u_x^{(-)}$ are the x-axis displacements of the separated node pairs from the positive side and the negative side of the fault, respectively, depending on the normal vector $\mathbf{n}$ of the fault. The nodal pressures are $p^{(+)}$ and $p^{(-)}$, and $\mathbf{t}$ is the tangent vector of the fault. By combining the governing equation and the constraint equation, the system becomes

$$\begin{bmatrix} \mathbf{K} & \mathbf{G}^{\mathrm{T}} \\ \mathbf{G} & \mathbf{0} \end{bmatrix} \begin{bmatrix} \Delta\mathbf{U}_n \\ \boldsymbol{\lambda}_n \end{bmatrix} = \begin{bmatrix} \Delta\mathbf{f}_n \\ \mathbf{I}_n \end{bmatrix}, \tag{2.5}$$

where $\mathbf{G}$ is the constraint matrix, and $\boldsymbol{\lambda}_n$, the vector with Lagrange multipliers, contains the nodal forces and the pressure sources needed to satisfy the constraints, and thus becomes a proxy for the stress field of a fault. At each quasi-static time step, the stress field is calculated. Then, depending on the applied friction law, the state of the fault is evaluated. In this study, we apply the slip-weakening friction law. If the shear stress on a fault exceeds the fault strength, we switch to the dynamic solver.

2.2.2. DYNAMIC LOADING

When the fault reaches a critical state, where the shear stress exceeds the fault strength, the fault is reactivated and an acceleration is expected. Therefore, in this phase, the model is solved with the elastodynamic equation:

$$\mathbf{M}\ddot{\mathbf{u}} + \mathbf{C}\dot{\mathbf{u}} + \mathbf{K}\mathbf{u} = \mathbf{f}, \tag{2.6}$$

$$\mathbf{u}_n = \mathbf{M}^{-1}\left(\Delta t^2\left(\mathbf{f}_n - \mathbf{K}\mathbf{u}_{n-1}\right) - \Delta t\,\mathbf{C}\left(\mathbf{u}_{n-1} - \mathbf{u}_{n-2}\right)\right) + 2\mathbf{u}_{n-1} - \mathbf{u}_{n-2}, \tag{2.7}$$

$$\begin{aligned}\Delta\mathbf{u}_n =& \mathbf{M}^{-1}\left(\Delta t^2\left(\Delta\mathbf{f}_n - \mathbf{K}\Delta\mathbf{u}_{n-1}\right) - \Delta t\,\mathbf{C}\left(\Delta\mathbf{u}_{n-1} - \Delta\mathbf{u}_{n-2}\right)\right) + 2\Delta\mathbf{u}_{n-1} \\ & - \Delta\mathbf{u}_{n-2}.\end{aligned} \tag{2.8}$$

Eq. 2.8 gives the displacement on nodes without constraints. For the simulation of a fault failure, a constrained dynamic solution is achieved via a forward incremental Lagrange Multiplier method:

$$\lambda_n = \left(\Delta t^2\mathbf{G}\mathbf{M}^{-1}\mathbf{G}^{\mathrm{T}}\right)^{-1}\left(\mathbf{G}\Delta\mathbf{u}_n - \mathbf{I}_n\right)\Delta\mathbf{u}_n = \Delta\mathbf{u}_n - \Delta t^2\mathbf{M}^{-1}\mathbf{G}^{\mathrm{T}}\lambda_n, \tag{2.9}$$

where the Lagrange multiplier λ_n can be interpreted as the nodal force required to satisfy the constraints on the solution $\mathbf{u}_n$.

When the governing equation switches to the elastodynamic equation, the dynamic simulation includes the inertia term and calculates dynamic slip of the fault and the seismic wave propagation problem. The dynamic simulation has a relatively short duration, in the order of seconds. Given this brief duration, we can assume that pore pressure variations are negligible. This justifies the use of the standard elastodynamic equation without the need of a more complex poro-elastodynamic formulation.

The (quasi-)static dynamic hybrid loading is implemented in this research to address the drawbacks and combine the advantages of both loading schemes: using the fast static solver for gradual loading and the dynamic solver for fault failure. The hybrid model is realized by updating the stress field in the dynamic simulation from the previous static solution, if the fault is unstable. At the end of each dynamic run, the slip state is evaluated, and the simulation switches back to the implicit static solver if the fault is stabilized. At the same time, the simulation updates the stress and the displacement fields from dynamic simulation for the next quasi-static iteration.

2.2.3. FRICTION, ELEMENT SIZE, AND TIME STEP

For earthquake rupture simulation, it is essential to calculate the fault's friction. This calculation can be generalized by the Mohr–Coulomb criterion:

$$\tau = \mu\sigma_n' + C, \tag{2.10}$$

where τ is the shear strength on the failure plane, μ is the friction coefficient, C is the cohesion, and σ_n' is the effective normal stress (the normal stress minus the pore pressure).

Two major friction laws are generally used to evaluate the friction coefficient. The first is the slip-weakening law, which assumes an initial friction coefficient, a residual coefficient, and a linear weakening distance. This model dictates that the friction coefficient linearly decreases with slip distance until a critical distance is reached, at which

point it becomes the residual friction coefficient. Another widely used friction law is the rate-and-state friction law, which accounts for both velocity-dependent and state-dependent factors that influence friction (Dieterich, 1979; Ruina, 1983).

In this research, we have chosen to use the slip-weakening law. This choice is based on the results of available, extensive sensitivity studies and analytical solutions showing this behaviour. Secondly, our objective is to simulate a region that has not experienced a strong earthquake for a long period prior to the gas production. Therefore, we do not need to consider the periodic behaviour of earthquakes, making the slip-weakening law better suited for this study.

For fault strength and friction calculations, we use the linear slip-weakening law described by

$$\mu = \mu_r + \max(0, 1 - D/D_c)\left(\mu_s - \mu_r\right). \tag{2.11}$$

In the 2-D benchmark model, we use the same linear slip-weakening friction law to evaluate the fault strength, with the initial friction coefficient $\mu_s = 0.6$, residual friction coefficient $\mu_r = 0.45$, and critical slip distance $D_c = 0.005$ m. According to Day et al. (2005), the resolution of the coherence length should be between 5 and 10 in order to provide an accurate simulation. Based on Uenishi and Rice (2003) and Galis et al. (2015), Wentinck (2018) derived the following critical length for 3-D simulations in the case of slip-weakening friction:

$$\frac{L_{nuc}}{D_c} = \sqrt{\frac{3.82\pi}{4}} \frac{\mu}{\sigma_n'\left(\mu_s - \mu_r\right)}. \tag{2.12}$$

Given a shear modulus $\mu = 6$ GPa, effective normal stress $\sigma_n' = 30$ MPa, $\mu_s - \mu_r = 0.15$, and critical slip distance $D_c = 0.005$ m, the critical slip patch length $L_{nuc} = 23.1$ m. In that case, an element size of 4 m is sufficient to accurately resolve the rupture.

`GMSH` (Geuzaine & Remacle, 2009) is used to generate the finite-element mesh for 2-D and 3-D simulations. We use a triangular, unstructured mesh to simulate the 2-D benchmark model. For that problem, the mesh size is smallest (0.6 m) at the reservoir interval near the fault, and increases to 40 m near the outside boundary of the model. For 3-D simulations, tetrahedral elements are used, with the element size ranging from 4 m at the reservoir offset interval near the main fault to 200 m near the model boundary. This results in a total of about 80,000 elements for 2-D models and around 1,000,000 elements for 3-D models.

As mentioned in Section 2.2.1 with regard to quasi-static loading, by manually assigning the pressure value in the solution space, the quasi-static time step Δt is no longer present in the governing equation (2.3). The depletion Δp in each quasi-static step becomes the main input for the resulting displacement field $\Delta \mathbf{u}$. As the quasi-static loading is linear while the triggering of the seismic rupture is a nonlinear process, we have extended the method of Meng (2017) by introducing a modelling strategy that searches for the depletion value for triggering and reduces the effect of overshooting. After the initialization of the model with the boundary conditions, we apply a 1-MPa depletion step for each quasi-static step to search for the triggering depletion value at which the seismic event occurs. Then, the simulation using the same model setting is repeated with a 1-MPa depletion step for the previously stable quasi-static step, and then changed to a 0.1-MPa depletion step for the previously seismic step until a seismic event occurs. If

necessary, for example when multiple seismic slip patches are initiated during the seismic rupture, the seismic step is further reduced to a smaller depletion step, until the seismic event exhibits only a single initial seismic slip patch.

2.3. BENCHMARK: 2-D POROELASTIC PROBLEM

The fault offset strongly influences the induced stress field in a uniformly depleted reservoir, as numerically shown by Van den Bogert (2018) and Buijze et al. (2019) in the 2-D case. Jansen and Meulenbroek (2022) derived an analytical expression for the poroelastic stress due to a displaced fault. The stress concentration caused by the reservoir offset strongly affects the regime of fault reactivation due to reservoir depletion. Because of the importance of stress concentration due to the reservoir offset, we at first test our results with respect to the 0- and 50-m offset models of Buijze et al. (2019).

2.3.1. MODEL DESIGN

Buijze et al. (2019) simulated the stress changes and the resulting dynamic rupture caused by reservoir depletion with a 2-D poroelastic model using the finite-element code `DIANA` (DIANA, 2016), with quasi-static and dynamic hybrid loading, similar to our work. Their simulation calculated the induced stress field from uniform reservoir depletion in a quasi-static scheme. When the shear stress exceeds the friction, the slip patch occurs and expands with further depletion. When the growing slip patch reaches the critical length, the seismic rupture occurs from the dynamic simulation.

We benchmark `Defmod` with the same 2-D induced seismicity problem, but with quasi-static loading and dynamic simulation. For the detailed model setup, we refer to Buijze et al. (2019), including material parameters, hydrostatic pressure, initial stress, and boundary conditions. Instead of the transfinite mesh, we implement the triangular mesh in our 2-D models with a mesh resolution comparable to that of Buijze et al. (2019) during the initialization of the model. In our simulations, the high resolution at the reservoir interval results in oscillations of the stress field on the fault, while such oscillations do not occur during actual reservoir depletion. The oscillation at the reservoir boundary is likely to be caused by the different ways the fault is implemented in the two models. DIANA uses interface elements to simulate stress, while Defmod employs the Lagrange multiplier method, which averages pressure values at the nodes based on the nearby elements. Therefore, we choose to import the same initial stress so that we could simulate the benchmark problem with a similar mesh size.

Note that additional differences exist in the implementation of the fault constraints despite the fact that the two codes solve both the quasi-static loading and the dynamic rupture following the same governing equations. The finite-element code `DIANA` modeled the fault with interface elements, while `Defmod` imposes fault constraints with the Lagrange Multiplier (LM) capping method without using the interface element. This difference results in different definitions of the pressure at the fault. `DIANA` directly obtains the pressure at all fault nodes from the interface elements. `Defmod` obtains the pressure at a fault node from the weighted average pressure of all elements that share the same fault node.

Both codes consider linear poroelasticity before the fault becomes critical. After the

fault becomes critical, the nonlinear rupture process occurs as the aseismic slip appears and expands with further depletion. Our study defines the aseismic slip as a stable shear slip of the fault. During dynamic simulation, the slip is stable and confined to the localized area without the expansion of the rupture. According to Buijze et al. (2019), the aseismic slip can transform into seismic slip if the length of the aseismic slip patch reaches a critical value before the slip patch is fully weakened. Therefore, capturing the transition from aseismic to seismic slip is important. Different methods are used in the two codes to capture this transition. DIANA implements the so-called arc-length method to adjust the depletion adaptively in order to address the nonlinear problem of dynamic rupture. As Defmod focuses on 3-D simulation, the computation cost for implementing such a method is prohibitively high. The convergence for the nonlinear problem becomes prominent when the aseismic slip turns into a seismic slip. Therefore, we choose to manually adjust the depletion value based on a search method discussed in Section 2.2.3. In this way, the computation cost remains low, while the overshooting effect is reduced.

2.3.2. BENCHMARK RESULTS

Fig. 2.1 shows the results for quasi-static loading and dynamic rupture from the benchmark test. Negative values in the normal stress indicate the compressive force. The results from the two different codes share the same major features on the incremental stress field. However, because of the different implementations of the fault constraints, differences are observed at the boundary of the reservoir. We believe that these are caused mainly by the use of the interface elements in DIANA.

The results show that the LM capping method for fault constraining used in Defmod offers results that are similar to those of the interface element method in DIANA for the incremental stress field. The differences mainly occur at the reservoir boundary, where the incremental pore-pressure contrast is located. The differences are caused by the fact that Defmod treats the pore pressure at a node as an element-wise average, whereas in DIANA the pore-pressure value is independent of the values in other elements. This results, in our case, in a smoother incremental pressure across the reservoir boundary, which affects the incremental stress field at the reservoir boundary. This, in turn, causes a spike for both shear stress and effective normal stress at the reservoir boundary. Consequently, the depletion value required for the seismic slip and the dynamic fault slip is lower in the case of our simulation using Defmod. This effect is most prominent for the zero-offset benchmark model.

The depletion values corresponding to triggering of the seismic slip for the model with zero-offset are different between the two approaches: with DIANA it is 30.17 MPa, with Defmod the value is 26 MPa. This difference is mainly due to the different methods for fault implementation. For the 50-m offset benchmark model, the triggering depletion values are more similar: 10.76 MPa for DIANA and 11 MPa for Defmod. In this case, the effect of the incremental stress field caused by the fault offset is more prominent than the effect of the fault-implementation method. For the zero-offset model, the lower triggering depletion value in Defmod results in a lower value of the shear capacity utilization (SCU) in the reservoir interval outside the aseismic slip patch when the seismic nucleation occurs. This causes lower amplitude and a shorter length for the slip

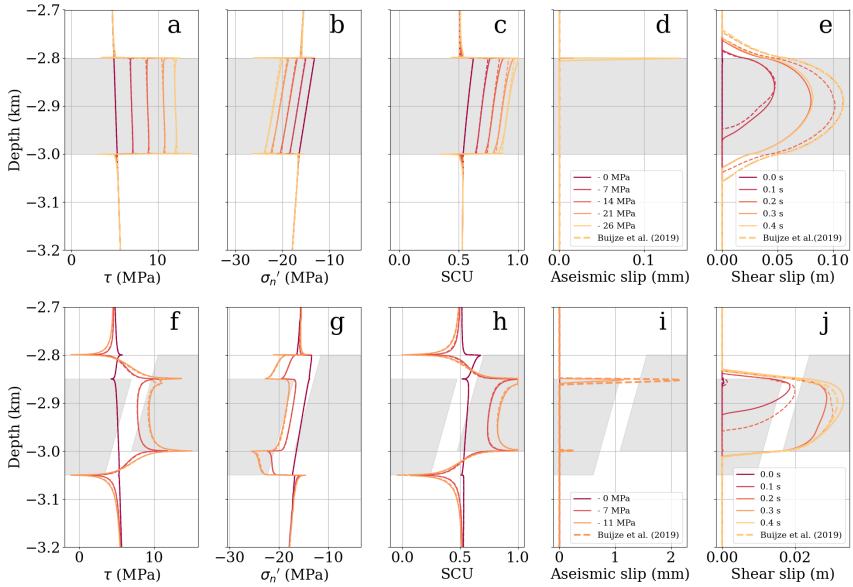

Figure 2.1: Benchmarking our 3-D modelling results using results from 2-D models of Buijze et al. (2019). a - e: benchmarking results for the zero-offset model. f - j: results for 50-m offset model. The solid lines show our results using `Defmod`. The dashed lines show the results of Buijze et al. (2019). The gray areas indicate the reservoir interval.

patch, despite the similarity in the onset of the rupture before 0.1 s. However, for the 50-m offset model, the similar triggering depletion values result in similar rupture length and slip amplitude. In this case, however, because `DIANA` implements a Newton solver and adaptively changes the depletion step until the seismic slip occurs, the result has a more substantial slip-weakening effect from the aseismic slip patch when the seismic slip occurs, compared to the result of `Defmod`. As a result, `Defmod` produces a faster acceleration and a slightly larger slip at the reservoir juxtaposition for a higher shear stress at the rupture patch. In general, `Defmod` offers comparable results to `DIANA`, capturing the same main features of induced seismicity.

2.4. 3-BLOCK RESERVOIR MODEL

After confirming that the benchmarking results shown in the previous section are satisfactory, we proceed with the simulations addressing our specific research questions. To better understand the effects of the realistic 3-D geometry of the source region on the occurrence of the induced earthquakes, we develop a set of models. These models focus on a number of prominent features of the source region that can strongly influence the generation of Zeerijp earthquake, induced by reservoir depletion. The fault-zone geometrical features include the varying offset, the intersection angle of the normal faults, and the shape of the resulting reservoir compartments. With the 3-block models, we investigate these geometrical features on the induced stress field, the fault reactivation, and the rupture evolution.

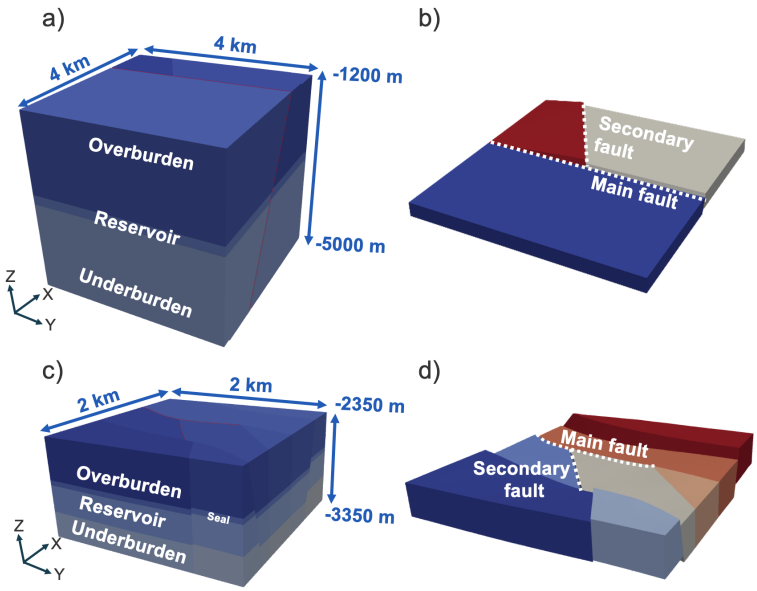

Figure 2.2: Geometry for the 3-D models. The 3-block models with a 60° intersection angle between the two faults (a) and its reservoir geometry (b). The source region geometry (c) of the Zeerijp model and its reservoir geometry (d) from the database (NAM, 2020).

2.4.1. 3-BLOCK MODEL DESIGN

In the geological model by NAM (2020), shown in Fig. 2.2d, the reservoir is split by the fault system into multiple compartments. According to Wentinck (2018), the hypocentre is located at the main fault (mFS7-Fault-54) and near the crossing with the secondary fault (mFS7-Fault-53). The effects of an offset reservoir have been extensively studied by Buijze et al. (2019). However, complicated offset patterns with, for example, the horst formed here by two intersecting normal faults, were rarely discussed so far. To investigate the relationship between reservoir geometry (horst) and induced seismicity, we create a simplified 3-block model focusing on the horst shape formed by the two intersecting faults. Furthermore, by varying the intersection angle, we change the shape of the horst and compare the induced stress field and the resulting seismic ruptures. To focus on the effect of the reservoir geometry, we choose to reduce the complexity of the model by including a similar composition (overburden, reservoir and underburden) to the benchmark model discussed above (Buijze et al., 2019).

In the 3-block model, a secondary fault is included—intersecting the main fault at its centre, consistent with the geological model. This configuration forms distinct reservoir compartments and reflects the structural complexity known for the field. The secondary fault is a vertical planar fault with a dip of 90° and an azimuth based on the intersection angle with the main fault: 90°, 60°, or 30°. The main fault has a 66° dip and cuts through the entire model, while the secondary fault ends at the intersection with the main fault. Note that we assume that the secondary fault remains stable during the entire simulation. A dip-slip rupture on this secondary fault is not favoured, given its steep dip, and

the strike direction not being supported by the orientation of the regional maximum and minimum stresses.

The reservoir is first split (offset) by the main fault, and then by the secondary fault. This results in a 3-compartment setup, shown in Fig. 2.2. The intersection angle controls the shape of the horst structure. These 3-block models with varying offsets on the main fault represent possible variations in the Zeerijp reservoir geometry. Such a structure also prevents the entire main fault from slipping due to a uniform depletion of the reservoir. The fault offset on the reservoir across the main fault changes from 0 to 100 m, from the x-boundary to the centre of the model. The faults intersect at the centre of the model, and then the offset drops by 50 m across the intersection line. The reservoir has a constant offset of 50 m across the secondary fault.

The 3-D models have the same material properties as the benchmark model (Buijze et al., 2019) discussed in the previous section. However, unlike those prior simulations, we do not impose any initial stress at the fault in our modelling, but initialize the model with gravity and gravity-based boundary traction. The boundary traction on both x- and y-boundaries are compressive. The ratio of the boundary traction to maximum vertical stress is 0.748 and 0.795 in, respectively, x- and y-direction. In this setting, the maximum horizontal stress is aligned with the strike of the main fault, and the minimum horizontal stress is aligned with the dip azimuth. After the initialization of the model, we apply roller boundary conditions at the side walls to simulate a laterally extended reservoir. Then we apply the adaptive stepping method mentioned in Section 2.2.3 to simulate the resulting seismic rupture. The 3-block models incorporate the same friction parameters as the 2-D benchmark model.

2.4.2. 3-BLOCK MODEL SIMULATION RESULTS

The simulations for the three different 3-block models clearly show the effect of the angle of intersection between two faults on the induced stress field, assuming uniform reservoir depletion. Fig. 2.3 shows the incremental stress field on the main fault, with a 30° intersection angle between two faults, after a 12.5 MPa uniform depletion of the reservoir. Note the relatively strong incremental shear stress in the strike direction. This is caused by the topography of the compartments located at the reservoir boundary next to the intersection line. This happens because the reservoir compaction has a horizontal component from the 3-step reservoir compartmentalization as a result of varying offsets of both the main fault and the secondary fault.

The reservoir offset on the main fault causes a concentration of the incremental stress from a uniformly depleted reservoir, as was also observed in previous studies on the induced stress field of a displaced fault (Buijze et al., 2019; Candela et al., 2019; Jansen & Meulenbroek, 2022; Van den Bogert, 2018). Fig. 2.3 illustrates the stress concentration at the juxtaposition boundary for the shear stress in the dip direction and for the normal stress, resulting in high SCU values at the same location. Importantly, the 3-block models have a varying fault-offset on the reservoir, where the offset changes from 0 m from one boundary to 100 m at the intersection, then drops to 50 m across the intersection line till the other boundary. The highest SCU value on the main fault is located near the area with the largest offset value. This area is close to the intersection line at both top and bottom of the reservoir juxtaposition interval. The location at the intersection

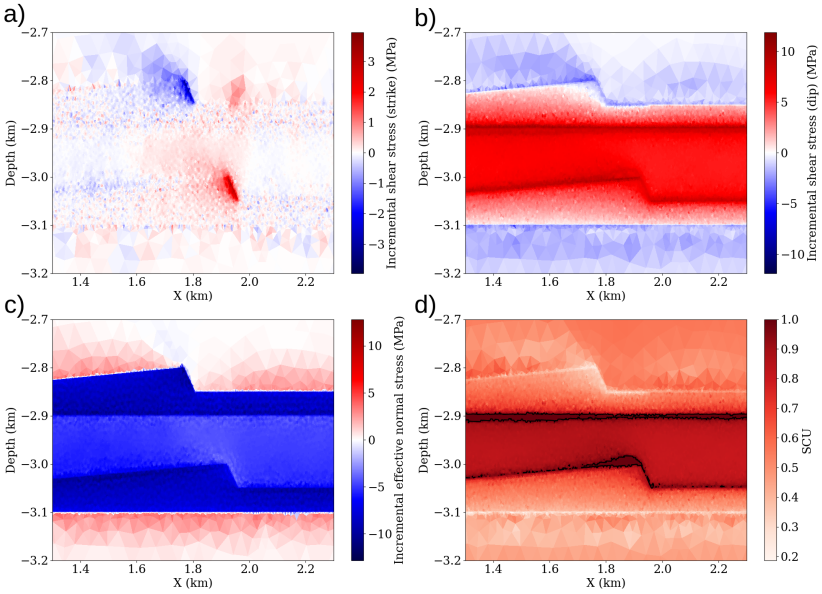

Figure 2.3: Incremental shear stress in the strike direction (a) and in the dip direction (b), incremental effective normal stress (c), and SCU (d) after 12.5 MPa uniform depletion of the reservoir for the 3-block model with a 30° intersection angle between the two faults.

line has the largest offset, but the SCU is not the highest there. The highest SCU occurs at a location with a slightly smaller offset. This is because the offset rapidly drops from 100-m to 50-m across the intersection, leading to a lower SCU value in the region of the largest offsets.

The SCU data in Fig. 2.3 show that the main fault at the top and bottom of the reservoir juxtaposition becomes critical when $SCU = 1$. The slip patches remain aseismic until the length of the patch reaches a critical value measured in the direction of the maximum shear stress, according to Uenishi and Rice (2003) and Buijze et al. (2019). However, due to the complicated structure of the fault offset, an analytical computation of such a critical length for the transition from aseismic to seismic slip is not possible.

Given the same boundary condition and the same depletion pattern, the triggering depletion values for the seismic event are similar in the three 3-block models. The values of the reservoir depletion required to trigger a seismic event for models with a 30°, 45°, or 60° intersection angle between the faults are 12.5 MPa, 12.6 MPa, and 12.6 MPa, respectively. Fig. 2.4 illustrates the result of our dynamic simulation of the seismic event for the three models. Our results indicate a change in the rupture pattern with different intersection angles. This includes important changes in the initial slip patch and in the rupture evolution.

For the 3-block model with a 60° fault intersection angle, the dynamic simulation shows that an initial seismic slip patch occurs at the top of the reservoir juxtaposition interval close to the intersection line. We refer to this location on the fault as slip patch A, as marked in Fig. 2.4c. This initial slip patch expands in both dip and strike directions.

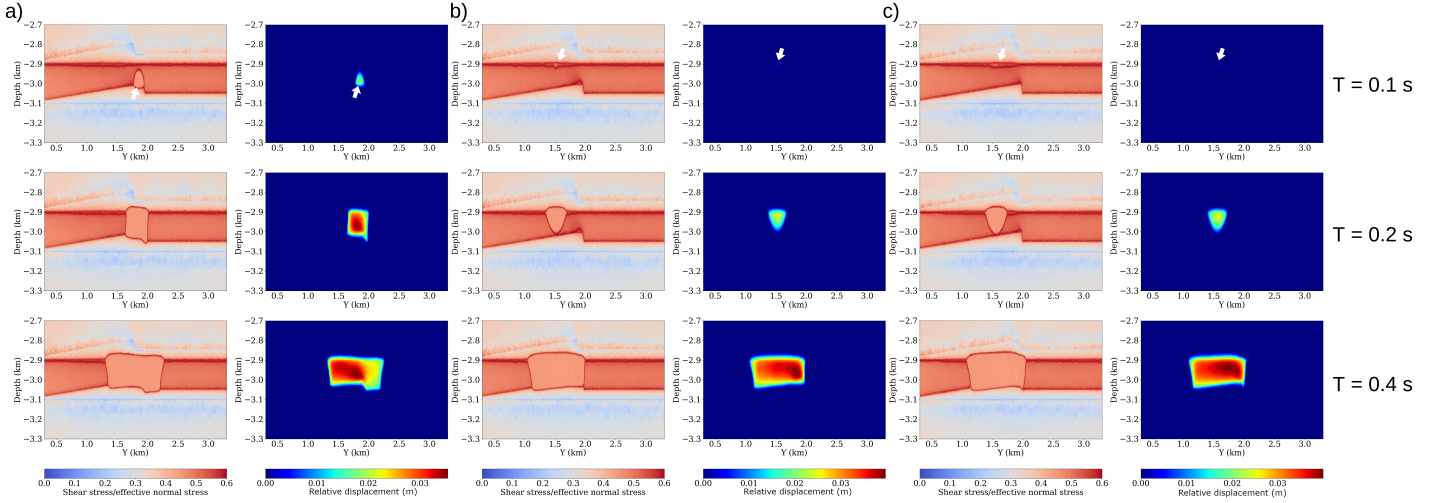

Figure 2.4: Results of dynamic simulation for each of the 3-block models, showing the temporal evolution of stress and induced slip. The arrow indicates the location of the initial slip patch. a) The seismic event at 12.5 MPa reservoir depletion for the model with 30° intersection angle between the two faults. b) The seismic event at 12.6 MPa reservoir depletion for the model with 45° intersection. c) The seismic event at 12.6 MPa reservoir depletion for the model with 60° intersection.

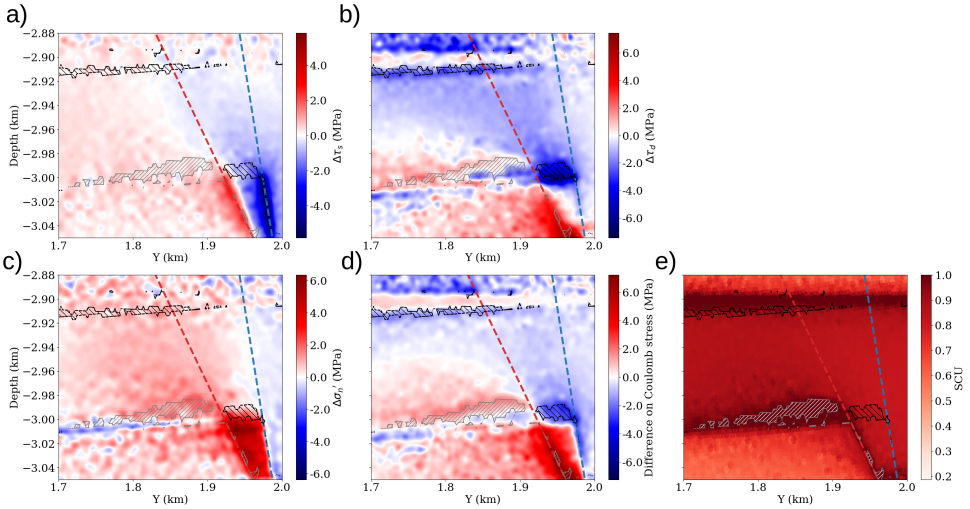

Figure 2.5: (a–d) Difference of induced stress fields at a 12.5 MPa depletion for the models with a 30° and 60° intersection angle between the faults. (e) The SCU values at the seismic events for the model with 30° fault intersection. The gray dashed area indicates the additional critical area from the model with a 60° fault intersection, and the black dashed area the reduced critical area (SCU = 1).

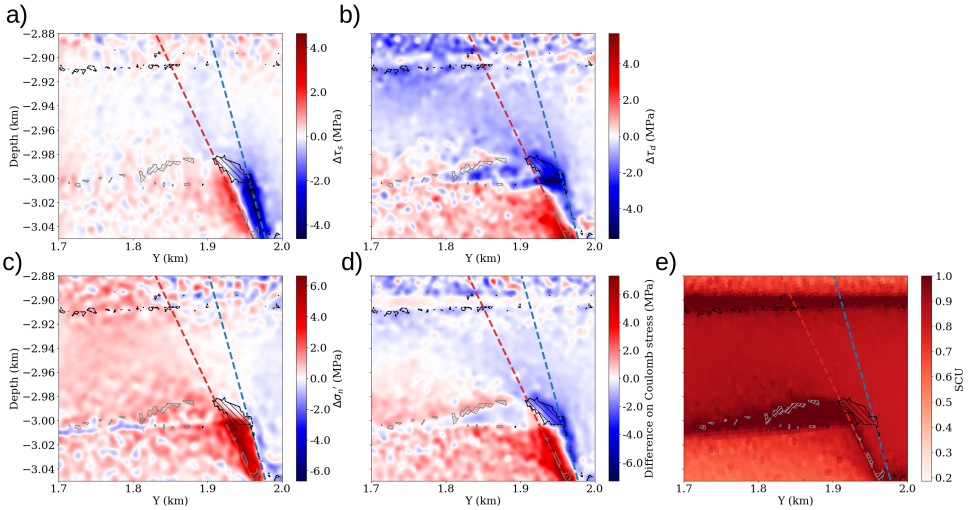

Figure 2.6: (a–d) Difference of induced stress fields at a 12.5 MPa depletion between the models with a 30° and 45° intersection angle between the faults. (e) The SCU values corresponding to the occurrence of seismic events for the model with a 30° fault intersection. The gray dashed area indicates the additional critical area for the model with a 45° fault intersection, and the black dashed area the reduced critical area.

The expansion in the dip direction stops at the boundary of the reservoir juxtaposition. In contrast, the expansion in the strike direction propagates from the initial slip patch to the whole reservoir juxtaposition. The location of the maximum slip shares its location with that of the initial slip patch.

The dynamic simulation for the 3-block model with a 30° intersection angle exhibits an initial slip patch at the bottom of the reservoir juxtaposition interval close to the intersection line. This we will refer to as slip patch B, shown in Fig. 2.4. Unlike slip patch A (60° fault intersection model), the slip patch B expands from the bottom to the top of the reservoir juxtaposition. The initial slip patch B expands in both the dip and strike directions, and then propagates within the whole reservoir juxtaposition. In this model, the maximum slip location is located at the bottom of the reservoir juxtaposition, the same as the location of the initial slip patch.

The dynamic simulation result for the 3-block model with the 45° intersection shows an intermediate pattern, compared to the earlier two models. The initial slip patch shares the same location as slip patch B, while the maximum slip is located in between the slip patches A and B, instead of at either of them.

All the seismic ruptures in the 3-block models propagate through the whole reservoir juxtaposition. The rupture not only propagates in the dip direction but also along the strike direction within the juxtaposition. The propagation in the strike direction can be explained by the fact that the 3-block models are the lateral extensions of the 2-D model, as the models have limited heterogeneity in the strike direction except for the varying offset. Furthermore, the triggering depletion for the 3-block model is similar to that of the 2-D offset model.

The difference in the initial slip patch for the 3 models with different intersection angles can be explained by their respective incremental stress field. Fig. 2.5 shows the difference in the incremental stress field between the 30° and 60° intersections at 12.5 MPa depletion. Note that the different fault intersection angle results in distinctive fault and reservoir compartment locations, thus affecting the distribution of pressure depletion on the main fault.

Fig. 2.5 shows that, after 12.5 MPa depletion, compared to the 60° fault intersection, the 30° fault intersection produces a larger incremental stress in the dip direction and a smaller effective normal stress at the lower reservoir juxtaposition. This difference corresponds to the area of the slip patch B during the seismic event. The incremental shear stress in the strike direction is not much affected by the location of the fault intersection. Fig. 2.5d shows the Coulomb stress difference between the two cases. The lower half of the reservoir juxtaposition has a positive value, indicating the promotion of slip in the area. The maximum value is observed at the fault intersection. However, this is due to the change in the location of the secondary fault.

Fig. 2.5e shows the SCU value corresponding to the occurrence of the seismic events, at 12.5 MPa depletion for the 30° intersection and 12.6 MPa depletion for the 60° intersection. Here, $SCU = 1$ indicates a critical state: the area turns into either a seismic slip patch or an aseismic slip patch. The contoured area denotes an increase and decrease in size of the slip patch compared with the 60° fault intersection. Fig. 2.6e shows the SCU value and the difference in slip patch between the models with a 30° and 45° intersection angle, corresponding to the occurrence of the seismic events. We see an intermediate

Formation	Depth to the top (m)	Density (kg/m3)	Poisson ratio (-)	Young's modulus (static) (GPa)
Zechstein	1200	2150	0.29	23.7
Anhydrite	~2800	2840	0.26	45.3
Rotliegend sandstone	~2850	2430	0.20	15.0
Carboniferous underburden	~3150	2650	0.27	18.4

Table 2.1: Material properties of the Zeerijp model, from Wentinck (2018).

difference with respect to the previous comparison, where the size of the increased and decreased slip patches are smaller than that for the model with 45° fault intersection.

In general, our results illustrate that a smaller intersection angle between the two faults promotes the slip patch to form at the lower reservoir juxtaposition due to the lateral compaction, and is more likely to initiate a seismic slip at the location of slip patch B. The maximum slip location shows the same trend in all cases.

2.5. ZEERIJP MODEL

2.5.1. ZEERIJP MODEL DESIGN

To verify our findings from the 3-block models pertaining to the relationship between the fault intersection angle and the rupture patterns, we construct a $2 \times 2 \times 1$ km^3 model focusing on the Zeerijp region in Groningen, the Netherlands. For this purpose, we make use of the Petrel geological model of the Groningen gas field (NAM, 2020). This geological model was created from stratigraphic and structural information derived from well-log and seismic data. We reconstruct the fault planes and the horizons using the point cloud data from this realistic geological model. The smoothly reconstructed fault planes and horizons are used to construct the mesh with `GMSH` for our 3-D finite-element simulation.

According to the Petrel model, the research area contains multiple formations within the reservoir interval. To focus on the effect of the 3-D reservoir geometry, we choose to include only the Zechstein overburden, the anhydrite top seal, the Rotliegend reservoir, and the Carboniferous underburden (basement). All the formations are considered to be homogeneous within the layers. The elastic moduli for these four formations are taken from Wentinck (2018), who calculated these moduli using seismic P-and S-wave velocities. Usually the laboratory-measured E_{dyn} is significantly greater than E_{sta}. Mahmoud et al. (2019) have shown that E_{dyn} can, in fact, be 1.5–3 times greater than E_{sta}. In our work, we use $E_{\text{dyn}} = 2\,E_{\text{sta}}$. Our model includes all major faults within the area of interest, together with appropriate fault offsets on the reservoir and the top seal. These fault offsets result in several reservoir compartments, which control the topography of the reservoir.

In this study, fault constraints are implemented only on the main fault mFS7-Fault-54, near the hypocentre of the 2018 Zeerijp M_L 3.4 earthquake as derived from seismic moment-tensor inversion (Dost et al., 2020). The other faults that are present in the model are considered stable and are characterized by their offsets on the reservoir, but

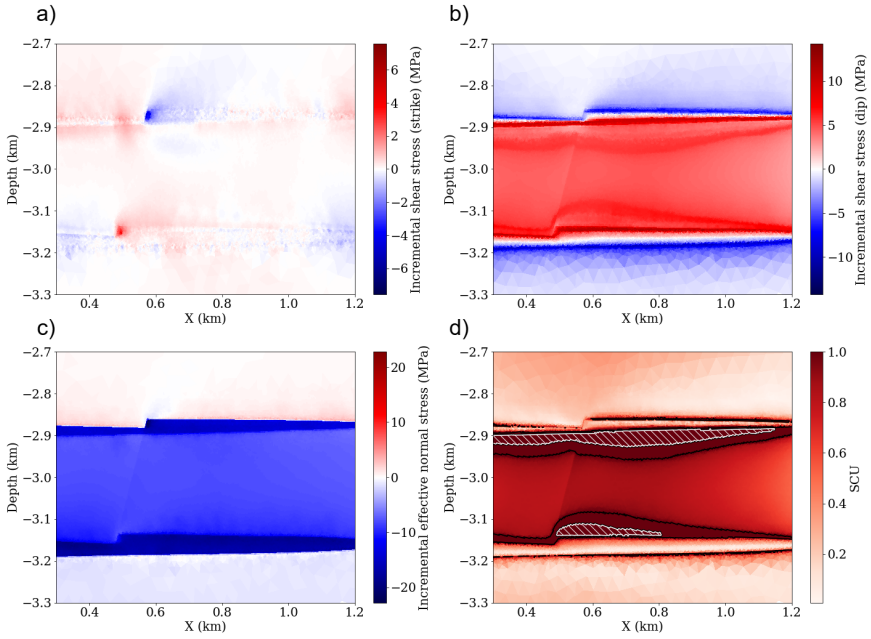

Figure 2.7: Incremental stress field for the Zeerijp model after a 26 MPa depletion. The black lines in (d) contour the critical area with SCU=1, and the white hatched areas indicate regions where the critical slip distance has been reached, thus causing full weakening.

their stress states are not distinguished. In our simulation, only the main fault is allowed to slip. The effect of fault intersections is examined in terms of their geometry. Dynamic triggering from one fault to another is not possible in this case.

The same boundary conditions as for the 3-block models discussed earlier have been considered for this model. The model is initialized with gravity and gravity-based boundary traction. After the initialization, uniform depletion is applied to the reservoir in order to simulate the induced stress field due to reservoir depletion until the first seismic slip occurs on the main fault. The friction parameters that we consider for the 3-D Zeerijp model are different from those for the 3-block models. The initial friction coefficient $\mu_s = 0.4$, residual friction coefficient $\mu_r = 0.3$, and critical slip distance $D_c = 0.2$ m. These friction parameters correspond to representative values. The friction parameter is initially set to the benchmark value, and thereafter adjusted to reproduce the seismic slip of the 2018 Zeerijp M_L 3.4 earthquake.

2.5.2. ZEERIJP MODEL SIMULATION RESULTS

To investigate how the incremental stress field and the fault rupture develop in case of a realistic, relatively complex reservoir geometry as the Zeerijp Petrel model, we perform our simulations. The reservoir geometry of the Zeerijp region is shown in Fig. 2.2. The incremental stress field at the main fault after a 16 MPa depletion of the reservoir is illustrated in Fig. 2.7. The stress field exhibits an offset-controlled stress pattern. The

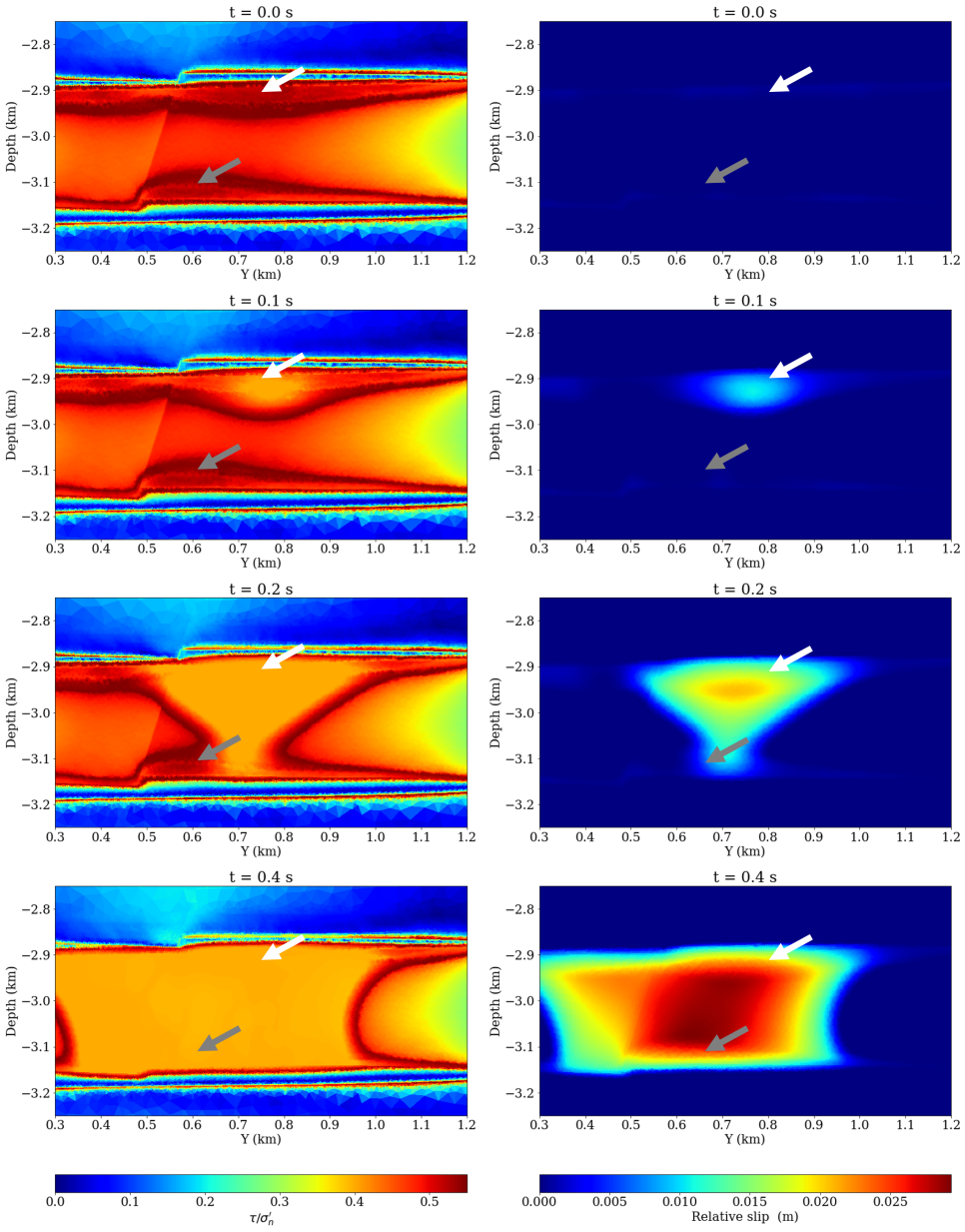

Figure 2.8: Dynamic simulation of the seismic event at a 26 MPa reservoir depletion for the Zeerijp model with a 30° intersection angle between the two faults. The white arrow indicates the location of the original seismic slip patch. The gray arrow indicates the location of the original aseismic slip patch. The pictures on the left show the ratio between shear stress and effective normal stress τ/σ'_n at different times from the onset of the fault reactivation (t = 0 s marks the beginning of the seismic rupture) and the pictures on the right show the relative displacement.

intersection between the main and the secondary faults in the Zeerijp model is 44.5°. With the fault offset having a pattern similar to the 3-block models (see Section 2.4), the location of the reservoir offset for the secondary fault exhibits a large incremental shear stress in the strike direction, with opposite directions at the top and at the bottom of the reservoir juxtaposition near the intersection. At the same location, the incremental effective normal stress is relatively weak at the bottom and strong at the top. The SCU values also show critically stressed slip patches both at A and B.

The reservoir compaction due to the distribution of reservoir compartments has a similar effect as that of the simplified models. This prevents the top of the reservoir juxtaposition at the intersection line from slipping, but promotes slipping at the bottom. This effect, together with the transition of the offset at the intersection, moves the location of the initial slip patch slightly away from the intersection line having the largest reservoir offset, as shown in Fig. 2.8.

A 50-m thick basal anhydrite layer is placed on top of the reservoir to better represent the geological structure of the gas reservoir at Zeerijp. The presence of this anhydrite layer increases the Coulomb stress on the main fault at the location of the top seal, and decreases the Coulomb stress on top of the top seal. The top seal hardly affects the incremental Coulomb stress within the reservoir interval.

From the modelled distribution of stress, we can clearly identify two major slip patches on the fault plane after a 26 MPa uniform depletion of the reservoir. In addition, these two slip patches resemble the slip patches found for the 3-block models discussed earlier. The seismic slip patch occurs at the top of the reservoir juxtaposition near the intersection, corresponding to the location of slip patch A in the 3-block model. The aseismic slip patches are located at the boundary of the reservoir juxtaposition. At the bottom of the reservoir juxtaposition, there is a major aseismic slip patch corresponding to the location of slip patch B in the 3-block model.

These slip patches remain aseismic until one patch reaches its critical length or is merged with a seismic slip patch. At the same time, the slip patch continues to be weakened with further depletion of the reservoir. Fully weakened fault nodes in the slip patch before the slip patch reaches its critical length decrease the length of slip patch, as the patches cannot be further weakened during fault reactivation.

Fig. 2.8 shows the result of dynamic simulation of the seismic event for the Zeerijp model. The seismic slip initiates at slip patch A. The initial slip patch expands and merges with the aseismic slip patch B. After the merging, the slip patch further expands in the strike direction, while the expansion in the dip direction gets halted at the reservoir juxtaposition. The area between the two slip patches has the maximum slip during dynamic simulation.

However, unlike the 3-block models, for the Zeerijp model the weakening is observed at both slip patches due to reservoir depletion—till the onset of the seismic event. This difference between the two models can be related to the model geometry and boundary conditions. Within slip patches A and B, a fully-weakened patch expands from the boundary of the reservoir juxtaposition to the centre of the juxtaposition. According to the results of 2-D simulation by Buijze et al. (2019), one of the conditions for the occurrence of seismic slip is that the slip patch cannot be fully weakened before the critical length for the seismic slip is reached. However, the situation becomes significantly more

complicated in case of 3-D simulations considering more realistic structural complexities. Our results of dynamic simulation using relatively complex 3-D models show that the fully-weakened slip patches are always located within the expanding slip patches. Although the fully-weakened slip patches are not susceptible to further weakening, their SCU values are still equal to 1. This SCU value allows the rupture front to propagate through. Therefore, in this case, the slip patch length is measured in the dip direction, and is then subtracted from the length of the fully-weakened slip patch. In our case, due to the steep dip angle of the main fault, we measure the slip patch length based on its depth interval. The analytical rupture length for the seismic event is 72.2 m when the dynamic Young's modulus $E_{dyn} = 2 \times E_{sta}$, and 36.1 m when the static Young's modulus is estimated from equation 2.12. The simulated slip patch length corresponding to the occurrence of the nucleation is 77.3 m, and 33.3 m if the fully weakened area is excluded.

The magnitude of the seismic event calculated from the slip data of our 3-D simulated seismic rupture is $M_W = 3.0$. This value matches well with the magnitude $M_L = 3.4$ obtained by inversion of observed seismological data for the 2018 Zeerijp earthquake (Dost et al., 2020), noting that in the Groningen gas field, M_W and M_L are approximately equal for events with $M_W > 2$ (Dost et al., 2018). The same assumption that the dynamic Young's modulus is twice the quasi-static Young's modulus is made for both these magnitude estimations. From our simulation, the depletion value at fault reactivation is 26 MPa, which is identical to the triggering depletion value from Wentinck (2018), calculated using the modelled depletion rate at the ZRP-3 well location. The initial slip patch and maximum slip are also close to the inverted hypocentre location, and the earthquake magnitude resembles the actual Zeerijp earthquake of 2018, according to Dost et al. (2020).

2.6. CONCLUDING REMARKS

We have performed quasi-static and dynamic simulations of induced seismicity considering realistic 3-D reservoir structure of the Groningen gas field. The results of our simulations for representative 3-block models show that the angle of the intersection between two normal faults has important additional effects on the induced stress field, compared with a single-fault scenario that is often considered for simplicity. Some of our obtained results offer insights that were hitherto unknown. Our findings allow us to draw the following conclusions:

1. Our results could quantify the incremental shear stress in the strike direction of the main fault, which is generated due to the horizontal component of the reservoir compaction at the horst structure.

2. A smaller intersection angle increases the incremental shear stress in the dip direction at a lower reservoir juxtaposition. It also slightly decreases the incremental effective normal stress on the main fault adjacent to the horst block. The incremental Coulomb stress is increased at the lower half of the reservoir juxtaposition at the horst block.

3. Consequently, when the intersection angle between the main fault and the secondary fault changes from 60° to 30°, the location of the initial slip patch changes

from the top of the reservoir juxtaposition near the intersection line to the bottom. The location of the area corresponding to the maximum slip is the same as that of the initial slip patch. For an intersection angle of 45°, we observe a transition for the location the maximum slip to be in between the location of the initial slips for the models with 30° and 60° intersection angles.

4. The triggering depletion value and the maximum slip are less affected by the fault intersection angle, despite the difference on the growth of the two major slip patches.

A relatively more realistic, 3-D model for the Zeerijp reservoir structure presents an incremental stress field which is similar to that for a representative 3-block model. The maximum slip for the seismic event is located in between the two slip patches, similar to a representative model with a 45° fault intersection angle. Our 3-D simulation produces an earthquake magnitude of M_W 3.0, due to fault reactivation occurring at a reservoir depletion value of 26 MPa. These values are similar to those for the 2018 Zeerijp earthquake of M_L 3.4 (Wentinck, 2018). The location of the simulated rupture is also close to the inverted hypocentre location for the 2018 earthquake (Dost et al., 2020).

From our results, we conclude that the reservoir geometry significantly influences the occurrence of induced earthquakes by affecting the incremental stress field, the nucleation location, the rupture pattern, and the location of the maximum slip. In the end, it plays an important role in determining the location of the hypocentre, the magnitude, and the depletion value corresponding to the triggering of a depletion-induced seismic event.

We also observe the same effects for different initial stress setups, particularly for the orientation of the horizontal stresses. In one setup, we interchange the maximum and the minimum horizontal stresses in the 3-block models during the initialisation: the minimum horizontal stress aligns with the strike of the main fault and the maximum horizontal stress aligns with the azimuth of the fault dip. In the simulated result, we observe the same effects as described above on the incremental stresses, on the growth of the initial slip patch, and on the rupture pattern. However, in this setup the triggering depletion value becomes more sensitive to the intersection angle. For the models with 30°, 45°, and 60° intersection angle, the triggering depletion value is 18.8 MPa, 19.25 MPa, and 19.4 MPa, respectively. Unlike the previous setup, the rupture is arrested at 1 km from the initial slip patch in the strike direction instead of propagating through the whole juxtaposition.

Most subsurface reservoirs, like the Groningen gas field, contain fault systems where multiple faults cut the reservoir at various intersection angles and offsets. The resulting reservoir topography and the induced stress field due to reservoir depletion are more complex than those for a single fault, even under the assumption of uniform reservoir depletion. An incorrectly estimated stress field will lead to, for instance, a wrong estimate of the triggering depletion value and wrong maximum magnitude for a possible seismic event due to the production activity. Consideration of realistic reservoir geometry is, therefore, of utmost importance during geomechanical simulation of the reservoir-induced seismicity.

In this study, we have assumed that the secondary fault at the intersection with the

main fault remains stable during the simulation. This assumption might cause underestimation of the event magnitude, as the induced shear stress in the reservoir is predominantly in the dip direction. This might result in rupture propagation from one fault to another through the fault intersection. In the following chapter of this thesis, we will discuss results of 3-D numerical simulations addressing the issue of migration of seismic rupture from primary to secondary fault.

3

SIMULATING FAULT REACTIVATION AND RUPTURE MIGRATION AT A NORMAL-FAULT INTERSECTION HORST UNDER RESERVOIR DEPLETION CONDITIONS

In geomechanical simulations of induced earthquakes, the role of fault intersections and their impact on fault reactivation are often overlooked. In a permeable reservoir such as the Groningen gas field, adjacent faults with similar dips and offsets are expected to experience a comparable induced stress field due to reservoir depletion. Therefore, it is crucial to consider the potential for rupture migration across fault intersections. In this study, we investigate the effect of fault intersections on induced seismicity resulting from reservoir depletion. We perform 3-D geomechanical simulations on a horst structure within a depleted reservoir, formed by two intersecting normal faults. The simulations capture the induced stress field from reservoir depletion, fault reactivation, and rupture migration through the intersection. Our results indicate that the seismic slip initiating on the main fault can trigger slip on the secondary fault via the intersection. The triggered slip on the secondary fault is confined to the lower offset interface near the intersection. We observe that, under identical boundary conditions, the dip of the secondary fault and the intersection angle significantly influence the size of the slip patch on the secondary fault. Furthermore, a smaller dip of the secondary fault can initiate seismic slip at the lower offset interface and subsequently induce slip on the main fault. To validate our findings, we simulate the 2018 M_L 3.4 Zeerijp earthquake in the Groningen gas field. The simulation results successfully replicate the rupture migration from the main fault to the secondary fault through the intersection at the lower offset. Additionally, our results exhibit strong

agreement with the field observations in terms of moment magnitude, hypocentre location, and depletion values at the time of the earthquake.

3.1. INTRODUCTION

The fluid extraction and injection in an underground reservoir induce pressure changes and, subsequently, stress perturbations. The poroelastic stress and the stress concentration from a displaced fault have been studied with only a single-planar-fault setup. However, in the Groningen gas field, the faults intersect with each other, forming a fault network. Dynamic faulting on a conjugate fault system has been observed in seismic data (Fukuyama, 2015), Yamashita et al. (2021) and surface deformation data (Lin & Chiba, 2017), Ross et al. (2019). These observations were mostly related to large magnitude tectonic earthquakes. In the Groningen gas field, dynamic faulting across intersecting faults is yet to be observed. This is because the induced earthquakes in the Groningen gas field generally have a magnitude below 3.5. Compared with large tectonic earthquakes, the relatively weak displacement-field of induced earthquakes requires the use of high-frequency data. Modelling such small rupture and generation of high frequencies are computationally expensive.

Forward-geomechanical simulation, on the other hand, can make use of the available geological model (NAM, 2020) and can be used to investigate the potential and impact of rupture migration in case of induced earthquakes. In Chapter 2 we discussed the effects of a fault-intersection horst on the induced stress field and dynamic rupture from a uniformly depleted reservoir considering only the main fault. The result showed that, through a horst structure, the uniform pressure depletion in the reservoir causes stress variation in the induced stress field at a location near the intersection. The localised stress variation depends on the geometry of the horst, mainly the intersection angle, which can affect the seismic rupture pattern.

In this Chapter, building on the findings reported in Chapter 2, we discuss the effect of mechanically intersecting faults adapting the crosslink constraint developed by Meng and Hager (2020). With this approach, we develop 3-D geomechanical models to investigate the rupture migration at a normal-fault-intersection horst, considering different horst geometry. To validate our findings, we simulate the 2018 Zeerijp M_L3.4 event with a detailed model based on the Zeerijp region of the Groningen gas field.

3.2. METHODOLOGY

Here, we use the finite-element simulation package `Defmod` (Meng, 2017), introduced in Chapter 2. `Defmod` simulates the induced stress field from reservoir depletion in quasi-static steps. When a fault becomes critical—meaning that the shear stress equals or exceeds the frictional resistance—`Defmod` computes the dynamic fault reactivation. The dynamic simulation provides results on rupture initiation and propagation, which continues until the rupture is arrested by friction.

3.2.1. MODEL GEOMETRY

We use similar model setting as in Chapter 2, including model geometries, boundary condition, mesh resolution, and friction parameters. Figures 2.2a and 2.2b illustrate the

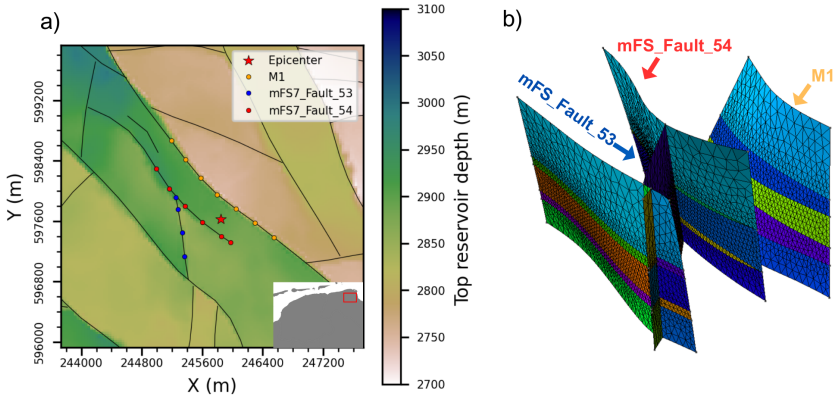

Figure 3.1: a) The location of the research area, including the epicentre of the 2018 M_L 3.4 Zeerijp event (Dost et al., 2020), and the fault map in the region (NAM, 2020). b): The geometry of the nearby faults near the epicentre.

geometry of the 3-D geomechanical model used to investigate the effect of the horst geometry on the induced seismicity. In this chapter, in addition to the intersection angle, we also investigate the effect of the dip of the secondary fault, as we focus on the rupture interaction between the two faults. Our goal is to check if a smaller dip of the secondary fault could change the order of rupture migration.

3.2.2. FAULT CONSTRAINT

`Defmod` (Meng & Wang, 2018) implements a split-node method for fracturing. Fractures are presented by pairs of overlapping nodes. The elements across the fault are separated by overlapping nodes, which are assigned depending on which side of the fault plane the element is present. These constraints on the displacement of the overlapping node pairs are used to simulate the fracturing process. Lagrange multipliers are implemented to satisfy the constraint, working as the proxy for the traction on the fault in both the tangential and the normal directions. Compared to Chapter 2, here we implement fault constraints not only at the main fault but also at the secondary fault. The simulation now calculates the stress field also at the secondary fault.

To simulate a horst structure formed by two intersecting normal faults, it is also important to consider the mechanical behaviour at the intersection. The conventional method (Fig. 3.2a) is used to calculate the initial stress from the initial loading, including the gravity and the gravity-based boundary tractions, to avoid the unrealistic opening of the intersection during the initial loading. In the conventional method, only the tip node of the secondary fault is connected to the same side of the split nodes from the main fault.

After the initialisation, the crosslink constraint method (Meng & Hager, 2020) (Fig. 3.2b) is adapted to simulate the rupture migration through the intersection. In this method, each intersection node pair consists of four overlapping nodes located on different sides of the intersection. The crosslink constraint, designed to maintain geomet-

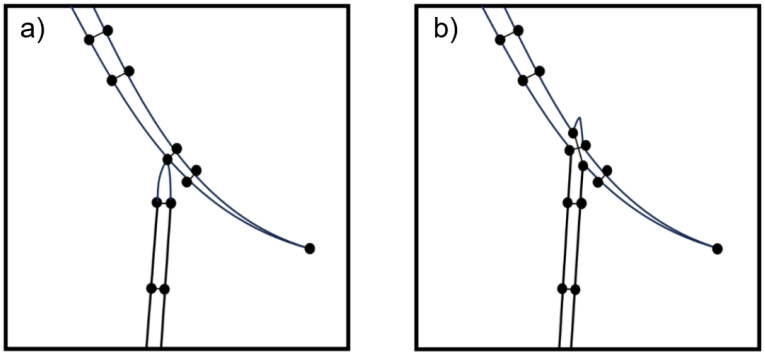

Figure 3.2: Map view illustration of the fault constraint applied at the fault intersection. a) conventional method: the tip of the branched (secondary) fault is connected to one of the split nodes from the main fault. b) crosslink constraint method: the branched fault slightly penetrates and interconnects with the main fault, in which the displacement of the four split nodes is constrained in the cross direction.

ric compatibility, can simulate the slip continuation across both faults depending on the stress state at the intersection. With the crosslink constraint method, the fault node at the intersection is first split into four nodes on each side of the intersection. We then apply the fault constraints diagonally across the intersection twice, with the tangential and normal directions of both faults respectively.

The crosslink method yields two sets of tractions at each intersection node pair, capturing the interaction between the two faults. The method enables the dynamic calculation of rupture truncation or transfer at the intersection, rather than prescribing it a priori. This is particularly important because both the initial shear stress (due to gravitational loading of the overburden) and the subsequent stress accumulation from reservoir depletion align predominantly with the down-dip directions of the faults. Therefore, implementing the crosslink constraint method allows for a physically consistent evaluation of the rupture behaviour at the fault intersection, resulting in a more realistic simulation.

3.2.3. FRICTION SETTING, BOUNDARY CONDITIONS, AND INITIAL LOADING

In Chapter 2, we simulated an induced earthquake at a horst structure using a frictional setup similar to that of Buijze et al. (2019), and obtained a comparable rupture pattern. The setting of the initial stress on faults is essential, and it directly affects the fault reactivation and rupture pattern. Top load, self-weight and hydrostatic pressure are first applied to calculate the vertical stress in the model. Then, horizontal boundary tractions proportional to the vertical stress at the boundary are applied to compute the initial fault stress. The used parameters in initial loading are chosen based on previous studies in the Groningen gas field (Van den Bogert, 2018; Wentinck, 2018). After the model initialisation, roller boundary conditions are applied at the side walls to simulate a laterally extended reservoir.

Adequate mesh resolution is needed to simulate the transition from aseismic to seismic slip. The criterion of design on the mesh size is based on Day et al. (2005) and Uenishi and Rice (2003). We assign the mesh size at a fault adjacent to the reservoir so that

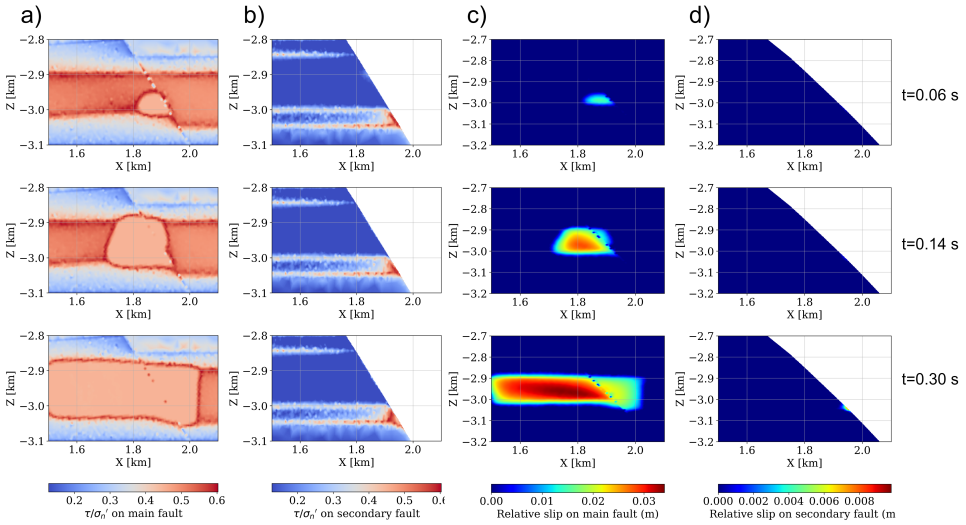

Figure 3.3: Stress field and dynamic rupture during the seismic event for the main fault and the secondary fault in the 30-degree intersection model. The ratio between shear stress τ and effective normal stress $\sigma_n{}'$ at the main fault (a) and at the secondary fault (b). The relative slip amplitude at the end of seismic event at the main fault (c) and at the secondary fault (d). t = 0 s marks the beginning of the fault reactivation.

the model has more than five elements to incorporate the analytical length of the aseismic slip patch in order to capture the spontaneous rupture, transiting from aseismic to seismic slip. The mesh size is increased going further away from the fault.

3.3. RUPTURE PROPAGATION THROUGH INTERSECTION

The inclusion of the secondary fault and the mechanical intersection has significant effects on the simulation result. Fig. 3.4 highlights two main effects of the mechanical intersection – discontinuities in rupture propagation and in slip amplitude.

For the model with the intersection, the propagation of the rupture at the main fault stops at the intersection, except at the top of the juxtaposition, where it continues through the intersection. While for the model without the intersection, the rupture propagates across the intersection line throughout the area of the juxtaposition. Additionally, the intersection model shows a sharp decrease in slip amplitude across the intersection, whereas the model without an intersection has a smooth amplitude gradient.

The discontinuities observed can be attributed to the implementation of the intersection. In Fig. 3.2, we show that the crosslink constraint method separates the main fault in the strike direction. Additionally, the boundary of the reservoir juxtaposition shows critical condition with shear-capacity utilization (SCU) > 1, while the centre remains stable. As a result, the rupture initiated on the main fault comes to a halt at the intersection. The rupture can only propagate through the intersection via the top boundary of juxtaposition on the east side where it is critically stressed.

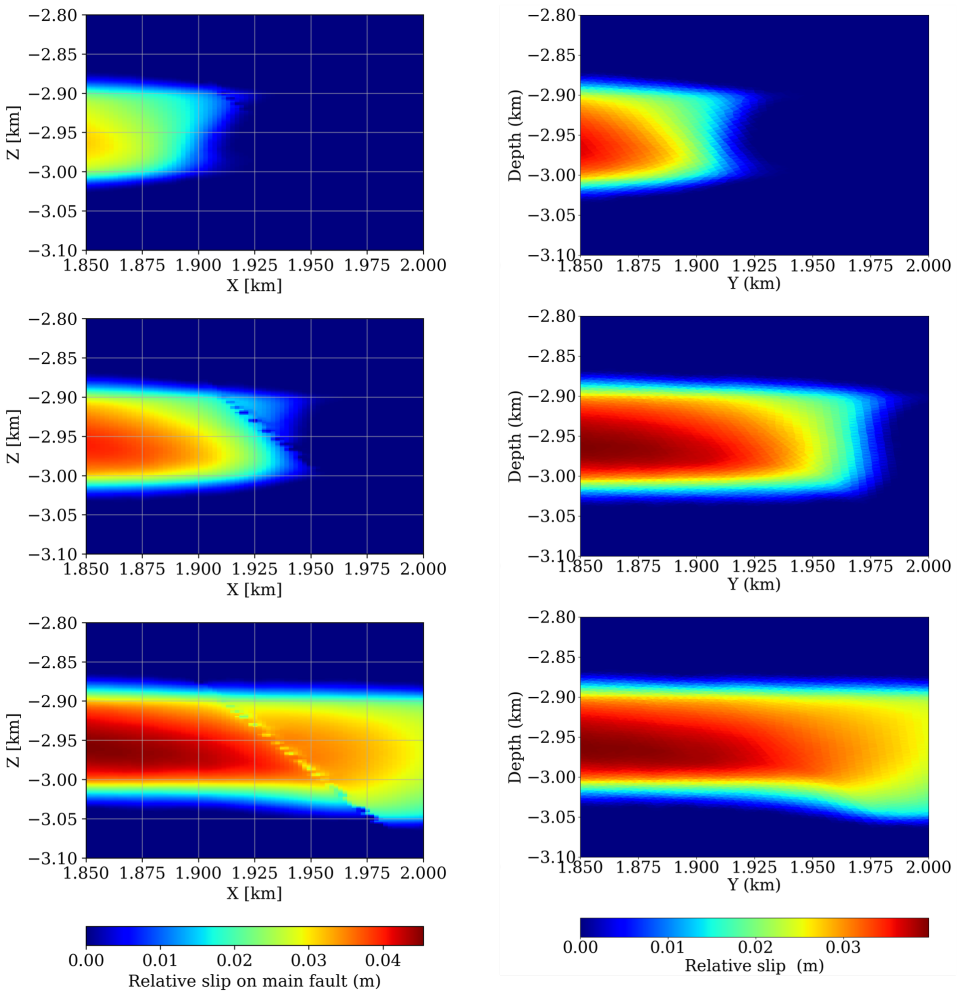

Figure 3.4: The dynamic rupture propagation across the intersection at the main fault during the seismic event shown in slip amplitude. From top to bottom, note the progression from the initiation to the termination of the dynamic rupture. Left: the slip amplitude of the model with mechanical intersection. Right: the slip amplitude of the model without mechanical intersection.

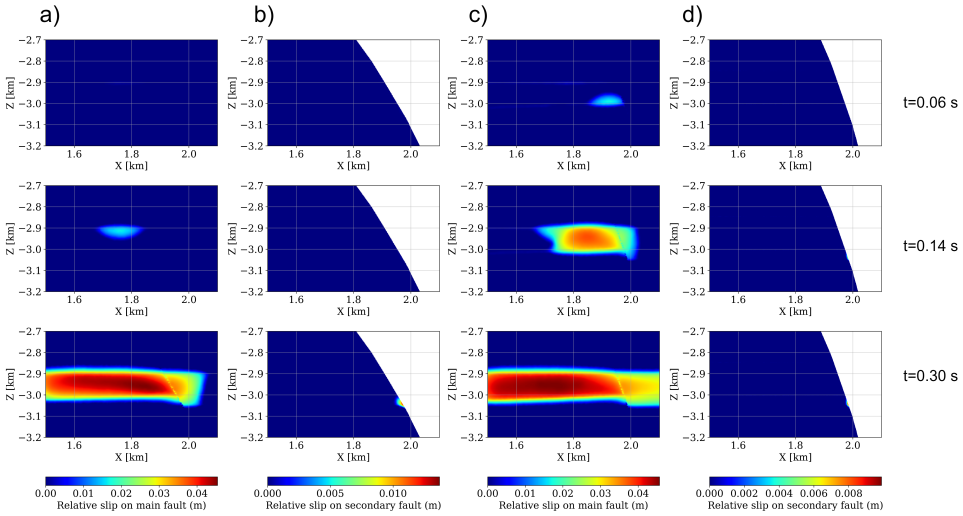

Figure 3.5: Slip amplitude on both faults during the seismic event for models with different intersection angles. From top to bottom, the progression shows the initiation to the termination of the dynamic rupture. Left: 45° intersection model—(a) main fault, (b) secondary fault. Right: 60° intersection model—(c) main fault, (d) secondary fault.

3.4. HORST GEOMETRY AFFECTING DYNAMIC RUPTURE PATTERN AT THE INTERSECTION

In this section, we show that the way a fault reactivates and ruptures is closely linked to the geometry of the horst structure, which is determined by the angle at which the two faults intersect. Moreover, we have noticed that seismic slip initiates at the secondary fault and subsequently triggers seismic slip at the main fault via the intersection if the secondary fault has a shallow dip angle.

3.4.1. INTERSECTION ANGLE

In Chapter 2, we discussed the effects of intersection angle on the induced stress field and rupture pattern during the seismic event for models with different intersection angles. In this section, we further test them with the crosslink constraint method and discuss the effect of fault intersection.

The induced stress field at the main fault follows the poroelastic Coulomb stress. The stress concentration was earlier observed and explained by Buijze et al. (2019) and Jansen and Meulenbroek (2022). With different intersection angles, 30, 45, and 60 degrees, we observe different rupture patterns, including nucleation location and slip amplitude at the final stage. The model with a 30-degree intersection shows an initial slip patch location at the lower half of the reservoir juxtaposition near the intersection and propagates along the juxtaposition. Both 45- and 60-degree intersection models show an initial slip patch at the top of the reservoir juxtaposition.

The 30- and 60-degree intersection models show maximum fault slip at the same

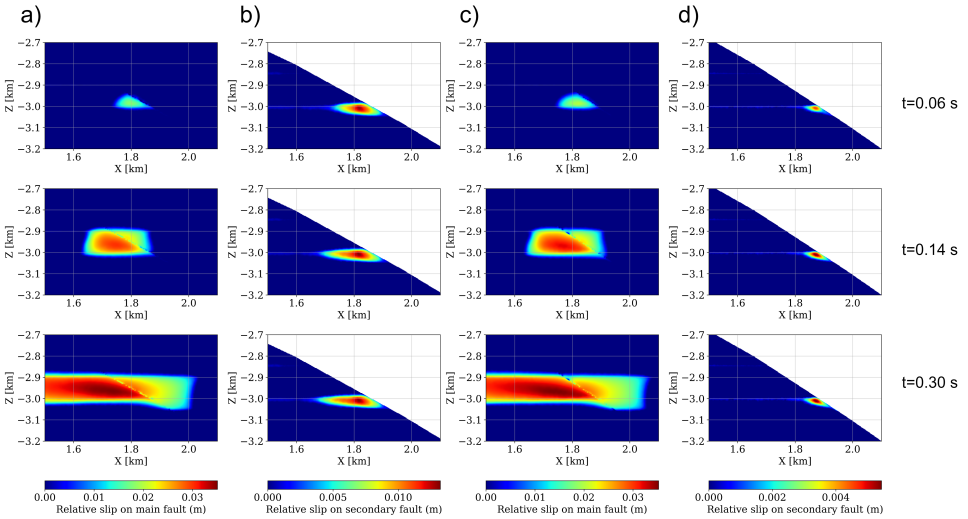

Figure 3.6: Slip amplitude on both faults during the seismic event for models with different dip angles. From top to bottom, the progression shows the initiation to the termination of the dynamic rupture. Left: 60° dip model—(a) main fault, (b) secondary fault. Right: 70° dip model—(c) main fault, (d) secondary fault.

location as the initial slip patch. The maximum slip of the 45-degree intersection is located at the centre of the juxtaposition, indicating an intermediate pattern between 30- and 60-degree intersection.

Due to the 90-degree dip of the secondary fault, the incremental shear stress is low in amplitude, except at the boundary of the reservoir juxtaposition, where the differential displacement across the fault causes the stress concentration. The stress field for the 30-degree intersection during the seismic event is illustrated in Figure 3.3. The secondary fault is only critical adjacent to the bottom of the horst structure.

As noted in Chapter 2, the smaller magnitude of the incremental normal stress at the deeper half of the reservoir juxtaposition is due to the poroelastic shrinkage of the horst structure. This particular characteristic of the horst structure increases the value of the SCU at the secondary fault located in the same area. Consequently, the secondary fault at the bottom of the horst structure accommodates minor slip patches that propagate from the main fault. Slip patches of similar size and amplitude are seen on each of the 30-, 45-, and 60-degree intersections.

3.4.2. DIP ANGLE OF THE SECONDARY FAULT

An important result obtained in our research is that the 90-degree dipping secondary fault in the Zeerijp region plays a crucial role in preventing fault slip within the reservoir juxtaposition. According to Mohr-Coulomb theory, a friction angle of 90 degrees suggests that the shear strength is infinite for any compressive normal stress. As a result, the 90-degree dipping secondary fault can prevent the fault slip. The slip patch observed at the secondary fault is mainly caused by the fault offset and a decrease in the incremental normal stress due to a compacting horst structure.

According to our findings, a secondary fault with a smaller dip angle can cause a bigger slip patch during a seismic event and can trigger the slip at the main fault. We observe that, during the seismic rupture, the smaller the dip angle of the secondary fault the larger the slip patch at the secondary fault and the higher the slip amplitude. In both 60- and 70-degree dip cases, the rupture initiates at the secondary fault and triggers the slip at the main fault through the intersection at the lower boundary of the horst structure.

The shift of the nucleation location is caused by a smaller dip angle of the secondary fault. The smaller friction angle increases the incremental Coulomb stress compared with a 90-degree fault, which contributes only to the normal stress. A smaller dip angle of the secondary fault also increases the SCU value at the fault during the initial loading.

3.5. ZEERIJP MODEL

In Chapter 2, we simulated the 2018 M_L 3.4 Zeerijp event by considering only the main fault mFS7-Fault-54. That simulation resulted in a local earthquake magnitude of M_L = 3.0. To investigate the impact of the intersecting faults on the rupture pattern, we performed a new simulation that included two faults and their mechanical intersection. This setup allowed us to evaluate whether the intersection could trigger seismic slip at the secondary fault mFS7-Fault-53, and potentially contribute to a higher magnitude of the seismic event.

According to Dost et al. (2020), the double couple component of the moment tensor derived from the ground motions of this event shows a dip angle of 62 degrees. From the geological model, Wentinck (2018) mentioned that the main fault, mFS7-Fault-54, has a dip angle between 72 to 84 degrees, while the secondary fault, mFS7-Fault-53, is a major vertical fault with a dip angle of 90 degrees. The intersection between the two faults at the intersection is 45 degrees.

Despite the presence of multiple faults in the region, our intersection model on the Zeerijp region also shows a similar pattern for both incremental stress field and dynamic rupture caused by the 45-degree fault intersection and the resulting horst structure. The model also shows the dynamic rupture propagation from the main fault to the secondary fault.

As was observed for the simplified models (Chapter 2), the implemented fault intersection has no additional impact on the incremental stress due to reservoir depletion, which is controlled by the reservoir geometry. The incremental stress in the Zeerijp model is primarily controlled by the offset on the reservoir across the fault and the horst structure, which can reduce the incremental normal stress and increase the incremental shear stress in the strike direction at the location of the horst structure close to the intersection.

Before the seismic slip, two aseismic slip patches develop at the boundary of the reservoir juxtaposition due to reservoir depletion. These slip patches continue to expand and slip within the reservoir juxtaposition, resulting in a drop in the friction coefficient at the patches. Given our assumed friction model, parts of the slip patches become fully weakened before the seismic event occurs.

When the reservoir pressure drops by 29 MPa, the slip patch located at the top of the reservoir juxtaposition increases in size and merges seismically with the slip patch

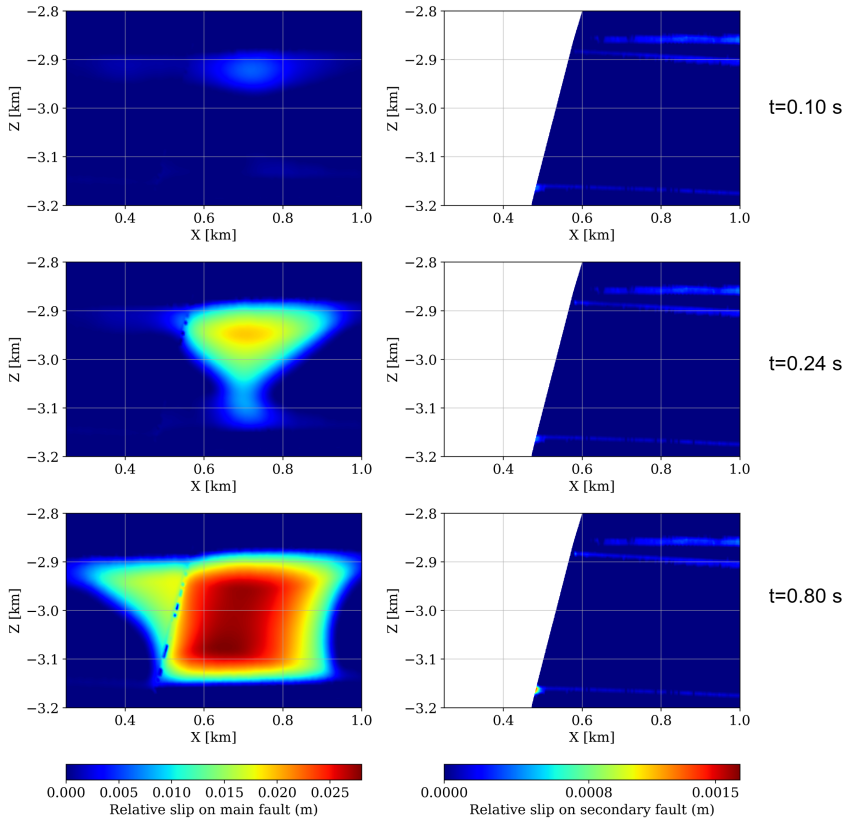

Figure 3.7: Slip amplitude at both faults in the Zeerijp model during the seismic event. Left: main fault. Right secondary fault. t = 0 s marks the beginning of the fault reactivation.

present at the lower juxtaposition. The seismic slip patch continues to expand in the strike direction before eventually stopping, resulting in a seismic event with a local magnitude M_L 2.9. Similar to the 45-degree intersection model with a 90-degree dipping secondary fault, the maximum slip occurs at the centre of the reservoir juxtaposition. The slip distribution on the main fault is discontinuous. The dynamic rupture propagates through the top of the reservoir and expands from the intersection and through the juxtaposition.

The majority of the secondary fault remains stable, despite the small aseismic slip resulting from the fault offset. The dynamic slip of the secondary fault is triggered through the fault intersection and is only limited near the intersection at the lower juxtaposition. The maximum slip at the secondary fault is also significantly smaller than that at the main fault.

Before the seismic slip, despite a small amount of aseismic slip resulting from the fault offset, the majority of the secondary fault remains stable. The seismic slip of the secondary fault is triggered by the main fault through the fault intersection and is limited only to the bottom of the horst structure at the intersection. Additionally, the maximum slip at the secondary fault is significantly smaller than that at the main fault.

Our results suggest that the 2018 M_L 3.4 Zeerijp event is mostly caused by the main fault mFS7-Fault-54 and has a possibility of dynamic triggering of the secondary fault through the intersection, although a confined slip patch with a low slip amplitude is expected in that case.

There is also a chance that the secondary faulting is triggered dynamically due to the intersection of the main fault, but it is expected to have a low slip amplitude and to be confined to a small area. However, in that case, the slip at the secondary fault would not be observable due to its low amplitude compared with the dominant slip at the main fault.

Note that, in Chapter 2, we simulated the Zeerijp model considering only the main fault, mFS7-Fault-54. In that model, the triggering depletion value was 26 MPa, which is lower than the 29 MPa required for triggering in case of the intersecting fault model presented in this chapter. Additionally, the intersecting fault model produced an induced earthquake event with a local magnitude M_L of 2.9, slightly lower than M_L of 3.0 observed in the single-fault model.

Despite these differences in triggering depletion and in local magnitude, the maximum slip amplitude and the slip pattern are remarkably similar between the two cases. In both models, the simulated slip patches are located near the hypocentre, as reported by Wentinck (2018) and Dost et al. (2020).

3.6. DISCUSSION

3.6.1. CROSSLINK CONSTRAINT METHOD

Fault intersections involve complex geometries and mechanisms that are not yet fully understood, particularly in induced seismicity settings. Laboratory observations of the stress history and the transient reactivation of intersecting fractures are currently lacking, which limits the ability to directly validate the numerical modelling results. The crosslink constraint method simulates stress patterns and truncation behaviour when

the fault slip reaches the intersection. Meng and Hager (2020) validated this approach using the benchmark provided by the Southern California Earthquake Center (SCEC). This method has been proven to be effective in modelling the intersection offset scenarios under assigned initial stress conditions and forms the basis for the numerical modelling in this study.

In our observations, the discontinuities in the rupture propagation and in the slip amplitude at the intersection appear to stem from the stress partitioning mechanics at the intersection nodes, as modelled by the crosslink constraint method. The propagation discontinuities introduced by the method increase the required nucleation length for a seismic event compared to the single-fault Zeerijp model. Consequently, the triggering depletion value for a seismic event is higher in case of the intersection model, while the resulting local magnitude of the induced earthquake is lower when compared to the model that considers only the main fault.

These differences arise from the way stress and displacement are calculated and constrained in the numerical simulations, which can lead to abrupt changes in the slip behaviour at the intersection. Similar differences have been noted in other numerical studies of induced earthquakes, suggesting that such effects could reflect inherent features of fault intersection mechanics rather than modelling artifacts. However, further laboratory and field studies are necessary to confirm whether these effects are representative of real-world fault behaviour.

The crosslink constraint method, as illustrated in Fig. 3.2, separates the main fault and the reservoir compartments at the intersection. Compared to the conventional methods, the crosslink method has a smaller relative displacement at the intersection due to reservoir compaction, and thus a lower shear stress. As a result, the intersection acts as a barrier, causing the slip distribution to become discontinuous and restricting the rupture propagation only to the top juxtaposition, where the fault remains in a critical state.

3.6.2. INITIAL STRESS SETTING

The accurate simulation of an induced seismic event requires a reliable representation of the stress field, encompassing both the initial stress prior to perturbation and the incremental stress changes caused by reservoir depletion. The resolution of the stress field becomes critical depending on the scale of the simulation, as presence of finer details allows for more accurate modelling of the local stress variations. For the Groningen gas field, the regional stress is well-documented and generally aligns with the orientation of the fault network. However, simulating specific events, such as the Zeerijp earthquake, demands a more detailed distribution of the initial stress to capture the localized fault interactions accurately.

The Groningen fault network consists of two primary fault sets with NW-SE and N-S orientations. In our simulation of the Zeerijp region, the main fault, mFS7-Fault-54, has a NW-SE orientation, while the secondary fault, mFS7-Fault-53, is oriented closer to N-S. Regional stress is predominantly aligned with the NW-SE faults, in accordance with the Mohr-Coulomb theory. However, this alignment raises uncertainties regarding the accuracy of the initial stress calculated for the N-S-oriented secondary fault using the same regional stress settings. If the stress conditions at the secondary fault are inaccurately

represented, it may lead to unrealistic triggering patterns or stress distributions at the intersection.

3.7. CONCLUSION

We have presented results of our simulation of induced earthquakes - incorporating intersecting faults in the source region, using the crosslink constraint method. We explored the combined impact of fault intersections and the intersection angle of a horst reservoir on the induced stress field at the faults and the resulting dynamic rupture patterns during induced earthquakes. Our findings can be summarized as follows:

1. The fault intersection implemented using the crosslink constraint method causes discontinuity in the lateral rupture propagation at the intersection, which leads to a discontinuity in the slip amplitude.

2. The implemented crosslink method introduces a mechanical barrier between the two faults, which affects the continuity of the rupture at the main fault and limits the slip patch size and amplitude at the secondary fault.

3. The dip angle of the secondary fault controls the stress field at that fault, and hence the rupture pattern and the slip patches. With a smaller (70 degrees) dip angle, we observe that the secondary fault initiates the seismic slip, and triggers the slip at the main fault. The lower the dip angle of the secondary fault, the larger the slip patches and the higher the slip amplitude at the secondary fault.

To verify our findings in a more realistic scenario, we simulated the Zeerijp event using the reservoir and fault geometry of the geological reservoir model. The outcome shows a depletion value, magnitude, and hypocentre location that closely resemble the 2018 M_L 3.4 Zeerijp event. This result is similar to that for a simplified model with a 45-degree intersection and a 90-degree dipping secondary fault, due to their similar geometries. The low incremental shear stress at the 90-degree dipping secondary fault results in a minor slip patch at the bottom of the horst structure, which is dynamically triggered by the seismic slip at the main fault.

From the effects of fault intersection on the stress field and the dynamic rupture, we conclude that, for the specific setting of the Zeerijp that we have simulated, the fault intersection introduces a rupture discontinuity, but it has only a minor impact on the overall characteristics of the simulated earthquake.

4

THE 2018 M_L 3.4 ZEERIJP INDUCED EARTHQUAKE: 3-D GEOMECHANICAL SIMULATION INCORPORATING SOURCE-REGION COMPLEXITY AND REPRODUCING FIELD-SEISMIC OBSERVATIONS

Constraining geomechanical simulation of previous induced earthquakes poses challenges due to uncertainties in the underground structure and in the available reservoir information. The utilisation of field seismic data of induced events for constraining geomechanical simulations is also limited. In an effort to understand the physical processes of a prior induced earthquake, we simulated the 2018 M_L 3.4 Zeerijp event in the Groningen gas field, the Netherlands, using a realistic setting. The model accounts for the regional stress and the induced stress caused by gas production. The simulation calculates the induced fault slip and the resulting seismic wavefield observed at a number of borehole receivers. To incorporate field-observation constraints, we compared the simulated waveforms with the field seismic data recorded at seven borehole receivers. In addition, we performed moment-tensor inversion on both synthetic seismograms and field seismograms at the same borehole receivers. The comparison reveals similarities not only in the waveforms but also in the inverted point sources, including the locations of the hypocentre and the moment tensor.

4.1. INTRODUCTION

To understand the process of induced seismic rupture due to gas production in Groningen, previous geomechanical simulations were mainly performed in 2-D. The induced stress field and the dynamic fault slip during aseismic and seismic events were investigated through such simulations (Buijze et al., 2019; DeDontney & Lele, 2018; Van den Bogert, 2018; Wentinck, 2018). In Chapter 2 and Chapter 3 of this thesis, we have discussed the results of 3-D geomechanical simulations, particularly focusing on the 2018 M_L 3.4 Zeerijp earthquake, also illustrating the effect of fault intersection. By incorporating realistic model settings and intersection mechanics in 3-D, we have obtained results that resemble field-data-based estimates of the triggering depletion value, the fault movement, and the slip-patch location.

Regarding the use of field-observed seismograms to address the mechanism of an induced earthquake, previous studies mostly rested on moment-tensor inversion to obtain the focal mechanism and the hypocentre location (Dost et al., 2018, 2020; Masfara et al., 2022). Such field-data-based inversions offer the point-source representation of an earthquake, generating synthetic seismograms that fit the field-observed seismograms. Contrary to the point-source assumption made in such inversion, geomechanical modelling simulates the dynamic slip of a fault that is finite both in space and time. Although geomechanical simulation may provide a better physical model for the induced earthquake (linking fault-zone structures and production geomechanics to dynamic faulting), so far these simulations have mostly been conducted in 2-D or in a quasi-static setting, and thus face difficulties in explaining the field-observed seismograms (Kühn et al., 2022).

Inversion of synthetic seismograms due to a more realistic, 3-D simulated finite faulting may connect the geomechanics of induced seismicity to field-observed seismograms and may lead to a finite-source model that is more extensive than a point-source model. However, such inversion is not a trivial task for a production-induced earthquake. A production-induced earthquake is mainly caused by fluid injection or extraction, and generally has a much smaller slip patch than a tectonic earthquake. The slip patch of an induced earthquake is usually limited by the extent of the reservoir where most of the rupture occurs, with a size in the order of 100×100 m^2. The small size of the slip patch makes finite-fault inversion challenging for the frequency bandwidth of the field-seismic data. Frequencies well above 10 Hz are necessary for sufficient resolution of the rupture zone (Woo et al., 2019). For such frequencies, seismic forward simulation becomes difficult because the elastic-wave velocity models are not accurate enough on smaller spatial scales and the computational cost is very large.

Past moment-tensor inversions of field seismograms to obtain the induced seismic rupture pattern have been restricted to frequencies below 5 Hz. Among the inversion methods, Dost et al. (2020) inverted all events with $M > 2$ in the Groningen region; their hypocentre distribution resembles those from other studies that use different methods. Willacy et al. (2019) made use of the full seismic waveform in 3-D elastic wavefield modelling to invert the moment tensor for induced seismicity. Masfara et al. (2022) developed a linearized Hamiltonian Monte-Carlo (HMC) method to invert the full moment tensors. This approach generally provides a good fit with the field-observed seismograms.

Clearly, while the moment-tensor inversion for a point source can provide a focal

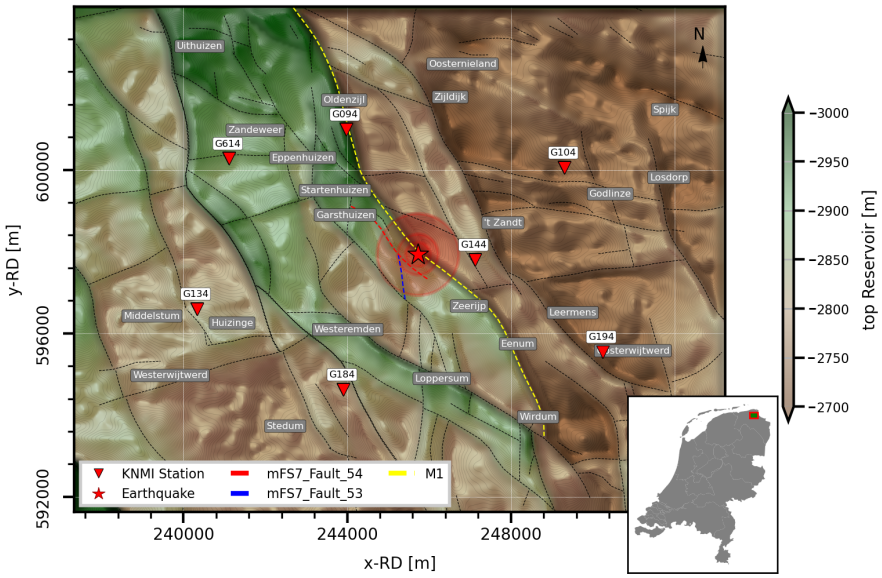

Figure 4.1: The research area, with the hypocentre of the 2018 M_L 3.4 Zeerijp event, the reservoir topography, and the locations of the Royal Netherlands Meteorological Institute (KNMI) stations with downhole seismic receivers.

mechanism of an induced earthquake, it fails to provide information on the actual faulting geomechanics. On the other hand, if the 3-D geomechanical simulation of an induced earthquake is carried out considering a realistic 3-D fault-zone structure and appropriate boundary conditions, the simulation can provide the induced stress field due to a changing reservoir pressure and, subsequently, generate the induced earthquake and seismic wavefield. Such a dynamic rupture simulation can provide an extensive mechanical description of the induced seismic source. An important constraint for the simulation can come from fitting the synthetic seismograms generated by the geomechanically simulated finite fault to the field-observed seismograms.

In this chapter, building on the results discussed in the previous two chapters of this thesis, we examine the simulated seismograms from our geomechanical simulation of the 2018 M_L 3.4 Zeerijp earthquake considering realistic fault structures in 3-D and the interaction between the main faults in 3-D — first in comparison with the field-observed seismograms and then in comparison with the inverted moment tensors.

In what follows, we first describe a new workflow comprising the geomechanical forward simulation and the formulation of an inverse problem. Next, we validate our simulation by comparing the synthetic seismograms from geomechanically simulated faulting with the field seismograms recorded in shallow boreholes in Groningen and the inverted hypocentres.

4.2. RESEARCH AREA AND WORKFLOW

Given the moderate seismic velocity in the reservoir region of the Groningen gas field and the fact that the reservoir-depletion-induced rupture in Groningen generally involves a slip patch smaller than 100 m in length and breadth, a point-source assumption is reasonable for the low-frequency seismograms available from the field. The hypocentre of the 2018 M_L 3.4 Zeerijp induced earthquake, one of the largest recorded seismic events in Groningen, is centrally located in this region (Fig. 4.1). This earthquake offers an opportunity to improve our understanding of induced seismicity in the region. This understanding is vital to mitigate damages due to similar reservoir-depletion- or reservoir-injection-induced earthquakes elsewhere.

Fig. 4.2 shows the workflow of our use of the field-observed seismograms to examine the geomechanical simulation of the finite-fault rupture occurring in the source region. The research is conducted first through forward simulation in which the rupture is simulated geomechanically, and then the corresponding synthetic seismograms are calculated. Finally, inversion is carried out to obtain a point-source representation for both field and synthetic seismograms. The two-way verification is meant to test the geomechanically simulated finite faulting using the field-observed seismograms. In the following sections, we will discuss in greater detail how each of the steps in this workflow is implemented.

4.3. SIMULATION OF FINITE RUPTURE AND THE CORRESPONDING SYNTHETIC SEISMOGRAMS

To replicate the seismic observations generated by an induced earthquake, it is important to accurately simulate the seismic source and subsequently model the resulting seismic wavefield. Induced seismicity in the Groningen gas field is a consequence of the gas extraction process, with fault slip occurring during the seismic event. Therefore, our simulation involves modelling of the dynamic fault slip due to reservoir depletion, followed by simulating the propagation of seismic waves to the receivers located at/near the surface.

4.3.1. GEOMECHANICAL SIMULATION OF SEISMIC RUPTURE

We simulate the stress field on the faults and the dynamic fault rupture with the open-source package `Defmod` (Meng, 2017). The simulation comprises two phases. First, we simulate the induced stress field due to reservoir depletion. When the fault becomes critical, as soon as the shear stress exceeds the friction, the fault slips dynamically. The dynamic fault slip can be aseismic or seismic. Here, we consider a self-sustained rupture to represent a seismic event.

The finite-fault rupture of the induced earthquake represents a seismic source that is finite in both space and time. Geomechanical simulation in a detailed setting is essential to develop a physical source model. Therefore, we perform the geomechanical simulation of a dynamic fault slip considering realistic 3-D reservoir and fault geometries.

Wentinck (2018) investigated the geomechanical process that generated the Zeerijp event. He performed 2-D geomechanical simulations for the host fault mFS7-Fault-54 (Fig. 4.1). Dost et al. (2020) suggested that this event could be caused by another fault,

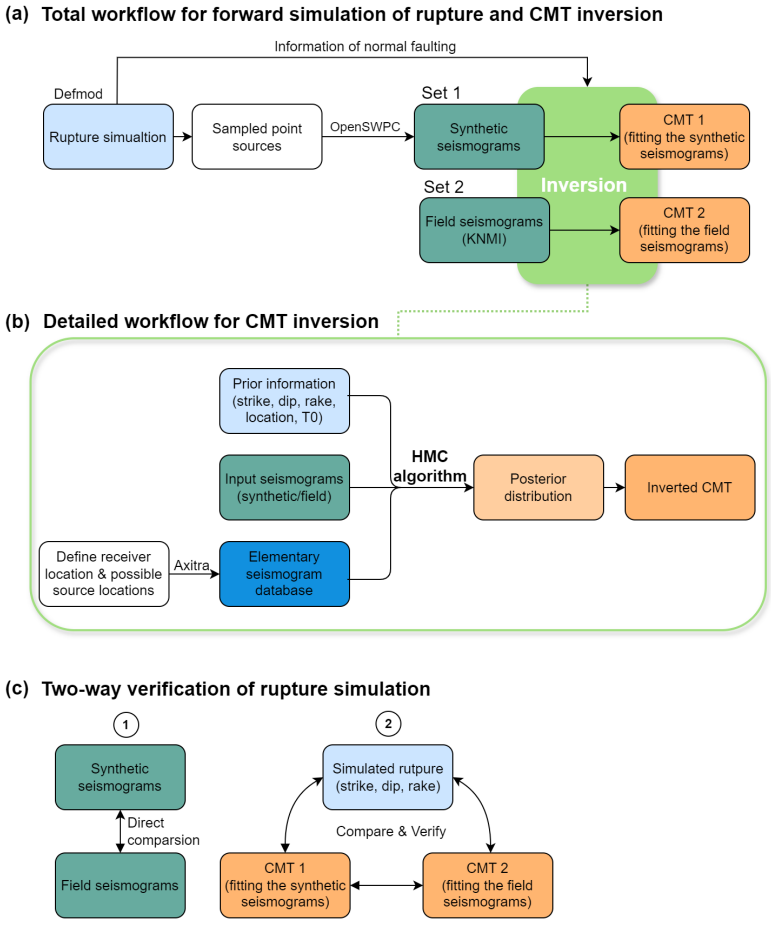

Figure 4.2: (a) Flow chart illustrating the strategy to use field-observed seismograms to improve our understanding of the source-region geomechanics of an induced earthquake in Groningen. The seismogram set 1 is simulated with an array of point sources distributed in space and time that are sampled around the simulated finite rupture. The seismogram set 2 is obtained from the KNMI database. These two sets of seismograms are used individually in the HMC inversion to search for their representative centroid moment tensor (CMT). (b) In the CMT inversion, the prior information on reservoir geometry (obtained from the Nederlandse Aardolie Maatschappij or NAM database) and on normal faulting (obtained from rupture simulation) is provided. Elementary seismograms at borehole receiver locations are calculated using the same velocity model as the one used in the geomechanical simulation. We obtain the CMTs from synthetic and field seismograms using the mean of the posterior distribution. (c) Finally, to test on field seismograms using the results of our geomechanical simulation, we directly compare the synthetic and the field seismograms. The rupture properties obtained from simulation are also verified using the two inverted CMTs.

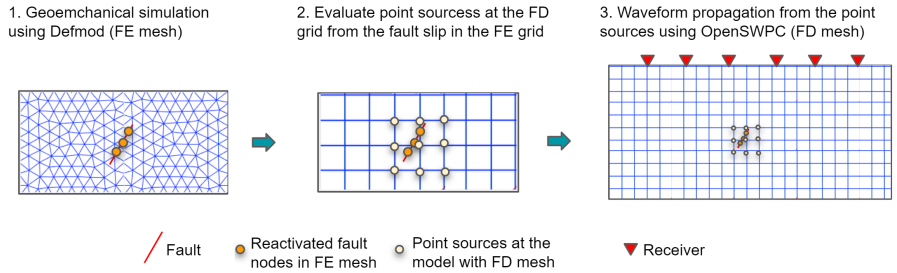

Figure 4.3: Schematic illustration of forward simulation to generate seismograms using a combination of finite-element (FE) modelling, geomechanical modelling of rupture (1 and 2), and finite-difference (FD) seismic modelling of waves propagating to the receivers (3).

not incorporated in the geological reservoir model (NAM, 2020). This fault was located between two faults — mFS7-Fault-54 and M1 (Fig. 4.1). In this study, we choose to implement the rupture simulation on mFS7-Fault-54 and mFS7-Fault-53, because these two faults were presented in the geometry database of the NAM reservoir model. The dip and the fault throw for the fault mFS7-Fault-54 and for the fault proposed by Dost et al. (2020) are similar.

The intersection between the faults mFS7-Fault-54 and mFS7-Fault-53 forms a horst structure. In Chapter 2 and Chapter 3, we simulated the induced seismicity using the geological model (NAM, 2020), which includes the horst structure formed by these two intersecting faults. We also then simulated the dynamic triggering from the main fault to the secondary fault. The results showed that the main fault mFS7-Fault-54 accommodates the majority of the fault slip, generating a seismic event of M_L 3.0 and occurring at a reservoir depletion of 26 MPa (Fig. 3.7). These values are close to those corresponding to the actual Zeerijp earthquake of 2018.

Figure 3.7 shows the relative slip on both faults during the seismic rupture. The seismic slip starts at the top of the reservoir juxtaposition and propagates along the dip direction all the way to the boundary of the lower juxtaposition. The rupture also expands in the strike direction and stops at about 100 m from the initial slip patch. The rupture process from the initial slip patch to the final stage spans approximately 0.4 s, indicating that the rupture is finite both in space and time. These results show that the rupture represents predominantly a normal faulting, and the final slip amplitude is relatively homogeneous within the central slip patch. The slip at the secondary fault is limited in size and amplitude, adjacent to the bottom of the horst structures. The uniform distribution of the slip amplitude over a regular-shaped slip patch favours a point-source approximation, which considers identical movement across a regular slip patch.

4.3.2. MODELLING SEISMIC WAVE PROPAGATION

An accurate rupture simulation requires a high mesh resolution to effectively capture the transition from an aseismic slip to a seismic slip, as discussed by Uenishi and Rice (2003) and Day et al. (2005). However, a higher mesh resolution increases the computational cost. To balance accuracy and efficiency, we confine the high mesh resolution to the

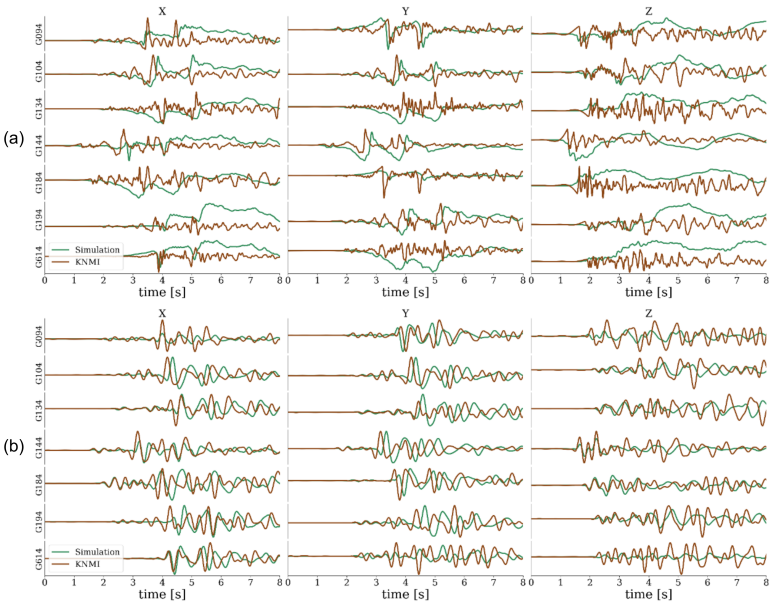

Figure 4.4: Comparison of 3-component synthetic seismograms from geomechanically simulated rupture (green) with field-observed seismograms (brown) at 200 m depth in seven boreholes in Groningen, obtained from the KNMI database. (a) Raw data. (b) Filtered (1–4 Hz) data.

fault plane within the reservoir juxtaposition and its surrounding region. Consequently, the geomechanical model is only applied to a subset of the full model, restricted to a volume close to the reservoir.

We then simulate the seismic waves propagating from the reservoir to the surface using the finite-difference simulator OpenSWPC (Maeda et al., 2017). The seismic source, the finite fault-slip obtained from geomechanical simulation, is represented by multiple point sources that are sampled on the simulated rupture in both space and time (Fig. 4.3). This workflow has been earlier successfully implemented and benchmarked by Meng and Wang (2018).

For comparing the synthetic seismic waveforms due to the geomechanically simulated finite rupture with the field seismograms, it is desirable to use a realistic 3-D velocity model. This is also true for performing the CMT inversion. However, for generation of the Green's function database for the CMT inversion, the implementation of a 3-D velocity model is very expensive. Therefore, we use a 1-D layered model for the velocity to simulate the seismic wavefield. We sample the velocity model (Romijn, 2017) at the location of the 2018 M_L 3.4 Zeerijp event as inverted by Dost et al. (2020).

Because of the low shear wave velocity in the near-surface region, a fine resolution in both space and time is required to correctly simulate the seismic wavefield. We use a maximum frequency of 5 Hz to reduce the computational time and still maintain a reasonable frequency band in the seismic data. The top 50 m of the Groningen subsurface is highly heterogeneous. The velocity model of Romijn (2017) neglected this heterogeneity. It is also computationally not feasible for us to simulate 3-D wave propagation in the top

50 m soil together with the deeper part till 3 km depth. Therefore, we calculate seismograms at receivers located at 200 m depth in seven different boreholes. This is done in order to minimise the near-surface effects. These seven borehole receiver locations are chosen because seismograms from the 2018 Zeerijp earthquake are available there.

In Fig. 4.4, the synthetic seismograms from the geomechanically simulated source are compared with the field-observed seismograms (KNMI database). The raw and filtered seismograms show comparable amplitude distributions among the receivers as well as comparable waveforms. When the data are filtered for the frequency range between 1 and 5 Hz, the waveforms become even more similar for both P and S waves. The good matching of the P waveform indicates that the simulated slip patch is located close to the hypocentre of the event as inverted from the field data.

However, if we examine the filtered X- and Y-components, we noticed a prominent misfit in the S-wave arrival time at several receivers (Fig. 4.4). This could mean that either the 1-D layered velocity model has a substantial effect on the arrival time of the S wave, or the S-wave velocity used in the forward simulation is not accurate enough.

4.4. MOMENT-TENSOR INVERSION

Next, we perform moment-tensor inversion of both sets of seismograms. The inversion of the field seismogram was done in the past using different inversion methods (e.g., KNMI (1993) and Dost et al. (2020)). For the consistency of the inversion methods on the synthetic and field seismograms, we use the inversion approach developed by Masfara et al. (2022), which provides a probabilistic distribution of the source parameters. It performs better when the uncertainty in the velocity model is large. We examine the slip-patch location, strike, dip, and rake of the fault movement in the inverted moment tensor.

4.4.1. HMC ALGORITHM AND ELEMENTARY SEISMOGRAMS

The probabilistic inversion method uses a Hamiltonian Monte Carlo (HMC) algorithm. This algorithm is highly efficient in sampling higher-dimensional model spaces (Masfara et al., 2022). The inversion strongly depends on the quality of the prior, which includes the moment tensor, centroid, and the origin time of the earthquake. For our inversions, we set up the initial models based on the fault geometry near the hypocentre as shown in the KNMI (1993) database. Thirteen initial models are evenly sampled from the nearby faults (mFS7-Fault-53, mFS7-Fault-54, and M1). We assume all initial models to have normal faulting and an origin time $t_0 = 0$ s.

The HMC algorithm inverts for 10 source parameters, viz. the centroid (three components), the origin time T0, and the moment tensor (six independent components). The algorithm delivers an estimate of the posterior probability distribution of all the source parameters. To invert the moment tensor $\mathbf{M}$ from the input seismograms, we have to calculate the elementary seismograms at the borehole receiver locations. The elementary seismograms are the displacements caused by the six independent elementary moment tensors, which together constitute the moment tensor $\mathbf{M}$. We use `Axitra` (Cotton & Coutant, 1997) to calculate the elementary seismograms, considering a 1-D layered seismic velocity structure for the Zeerijp region.

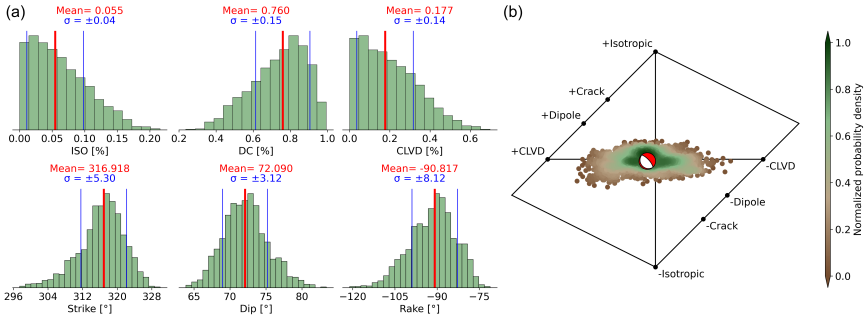

Figure 4.5: (a) Distribution of the CMT components obtained from the inversion of synthetic seismograms, showing the mean value, the standard deviation, and the strike/dip/rake of the double-couple component. ISO, DC and CLVD are, respectively, isotropic, double-couple, and compensated-linear-vector-dipole components of the CMT. (b) Hudson plot for the distribution (the coloured circles; the colour representing the normalised probability density) and the mean value (the white and red beach ball) of the CMT components.

We then perform the inversion to find the moment tensor and the hypocentre, using both synthetic and field seismograms. The field seismograms are obtained from the data portal of (KNMI, 1993).

4.4.2. INVERSION OF SYNTHETIC SEISMOGRAMS

Before inverting the synthetic seismograms, we apply a bandpass filter of 1–4 Hz to the elementary seismograms. Then, the initial models for the CMTs are assigned. Because the S-wave velocity model in this region is less accurate than the P-wave velocity model and to maintain the consistency of inversion for both synthetic and field seismograms, we fit only the P-wave data in the inversion.

Fig. 4.5 shows the posterior distribution of the inverted moment tensor: the moment tensor composition and the orientation of its double-couple component. The mean value of the CMTs shows a normal faulting with a predominant DC component in strike and dip angles, similar to the known geometry of the fault mFS7-Fault-54. The centroid and its covariance are shown in Fig. 4.6, indicating a location close to the centre of the simulated rupture. The waveform fitting for the inverted CMT is shown in Fig. 4.7. The fit with the synthetic seismograms is excellent, even though we fit only the P-wave data. Considering the good resemblance between the simulated rupture and the CMT in terms of the fault movement and the resulting seismograms, the CMT appears to serve well as a good point-source representation for the simulated rupture.

4.4.3. INVERTING FIELD SEISMOGRAMS

We then perform the same inversion for the same frequency range for the field seismograms and the elementary seismograms. Due to uncertainties in the velocity model, with the P-wave model being more accurate than the S-wave model, we conduct two separate inversions. We first invert the field seismograms by fitting only the P waveforms, and thereafter we perform inversion primarily using the S waveform. Although we use a taper before the S-wave arrivals to eliminate the P-wave information, it did not completely

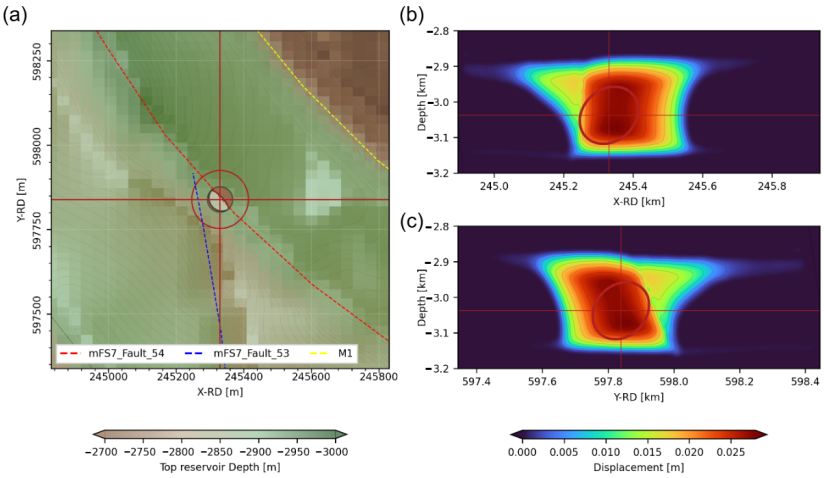

Figure 4.6: (a) The mean location (the intersection of the two red lines) and the covariance (the red ellipse) of the hypocentre inverted from the synthetic seismograms, shown in the XY-plane. X and Y are longitudinal and latitudinal coordinates, respectively. The background colour represents the depth to the top of the reservoir. (b) The same as (a) but in the XZ-plane. Z is depth. The background colour here is the relative slip of the simulated rupture. (c) The same as (b) but in the YZ-plane.

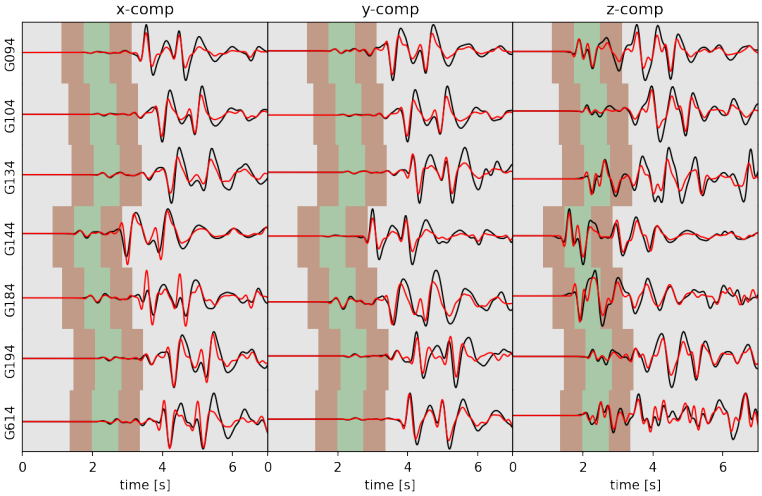

Figure 4.7: Waveform fitting for inversion using the synthetic seismograms. Red traces are waveforms corresponding to the inverted mean CMT. Black traces are the synthetic seismograms due to geomechanically simulated finite rupture. The green-shaded time windows correspond to the P waveform. In this part, the amplitude is not tapered for the input. On both sides of this window, we use tapering (the brown-shaded parts) to reduce the amplitude for the input. Data outside the colour-shaded parts are not used in the inversion. The earliest time (the beginning of the left brown-shaded part) is determined from the velocity and source-receiver location using an eikonal solver (Masfara et al., 2022).

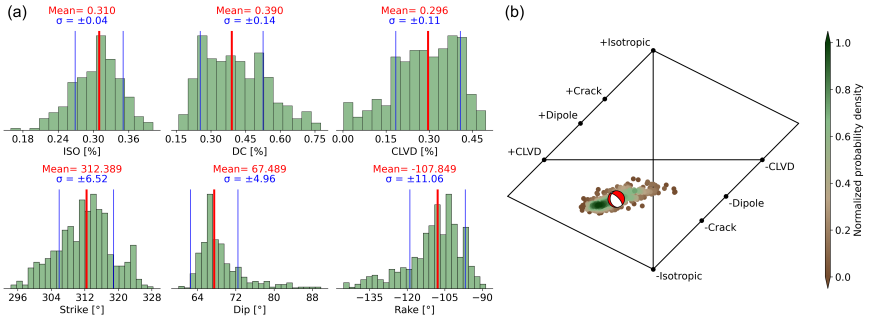

Figure 4.8: (a) Distribution of the CMT components obtained from the inversion of P waves in the field seismograms, showing the mean value, the standard deviation, and the strike/dip/rake of the double-couple component. ISO, DC and CLVD are, respectively, isotropic, double-couple, and compensated-linear-vector-dipole components of the CMT. (b) Hudson plot for the distribution (the coloured circles; the colour representing the normalised probability density) and the mean value (the white and red beach ball) of the CMT components.

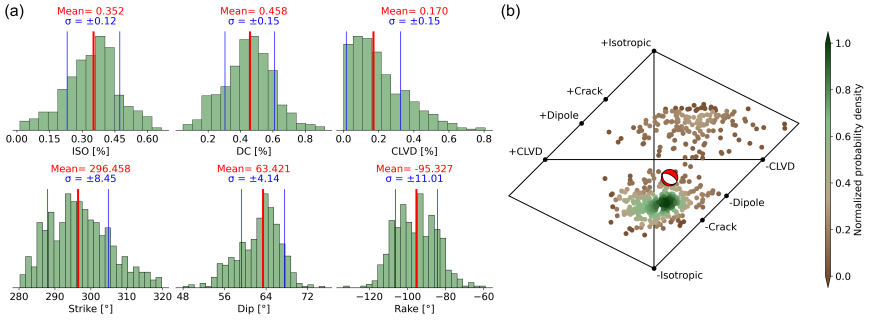

Figure 4.9: (a) Distribution of the CMT components obtained from the inversion of S waves in the field seismograms, showing the mean value, the standard deviation, and the strike/dip/rake of the double-couple component. ISO, DC and CLVD are, respectively, isotropic, double-couple, and compensated-linear-vector-dipole components of the CMT. (b) Hudson plot for the distribution (the coloured circles; the colour representing the normalised probability density) and the mean value (the white and red beach ball) of the CMT components.

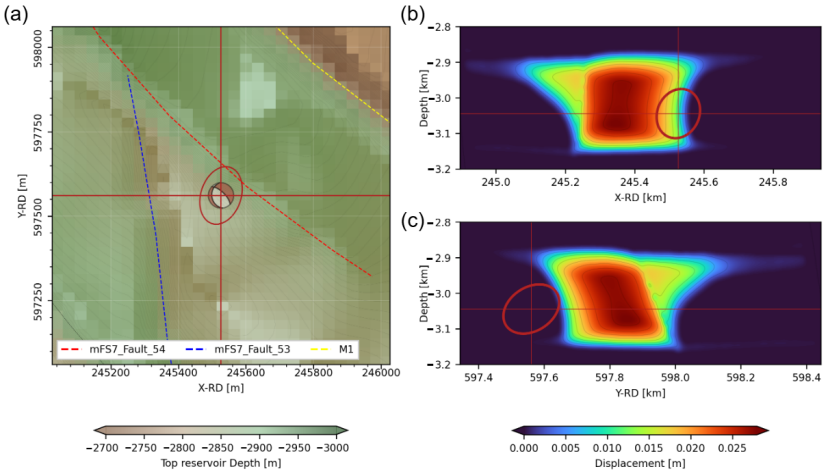

Figure 4.10: (a) The mean location (the intersection of the two red lines) and the covariance (the red ellipse) of the hypocentre inverted from the P waveforms in the field seismograms, shown in the XY-plane. X and Y are longitudinal and latitudinal coordinates, respectively. The background colour represents the depth to the top of the reservoir. (b) The same as (a) but in the XZ-plane. Z is depth. The background colour here is the relative slip of the simulated rupture. (c) The same as (b) but in the YZ-plane.

suppress P-wave energy.

Fig. 4.8 shows the distribution of the moment-tensor parameters obtained from inversion using P waveforms in the field data. For the S waveforms, the same is shown in Fig. 4.9. We see very similar moment-tensor compositions from these two inversions. The Hudson plots in both Figs. 4.8 and 4.9 indicate that the mean moment tensor has negative isotropic components, although the S-waveform result shows a wider distribution. The S-waveform result also shows a higher percentage of the DC components, a smaller dip angle, and normal faulting. The P-waveform result, on the other hand, shows a dip which is similar to the dip known from NAM data, and closer to a dip-slip event. Both CMTs show similar strike angles, which align with the strike of the fault mFS7-Fault-54.

The inverted mean hypocentre and covariance are shown in Figs. 4.10 and 4.11. The mean solution obtained from P waveforms shows an event located close to the fault mFS7-Fault-54 and also close to the simulated rupture. However, the mean solution obtained from inversion of the S waveforms yields a hypocentre that is located further to the east of the fault mFS7-Fault-54 and has a larger covariance than the P-waveform CMT. This location is also not far from the simulated rupture.

In Fig. 4.12, we show the waveform fitting for the mean CMT solution, obtained from P-waveform data, compared to the field seismograms. The P-waveform CMT offers a good fit for the P-wave arrivals in the field data. Only for receiver G104, some data misfit in the X- and Y-components exists. It is important to note that in all chosen receivers in the field, the P waves have larger amplitudes in the Z component than in the X and Y

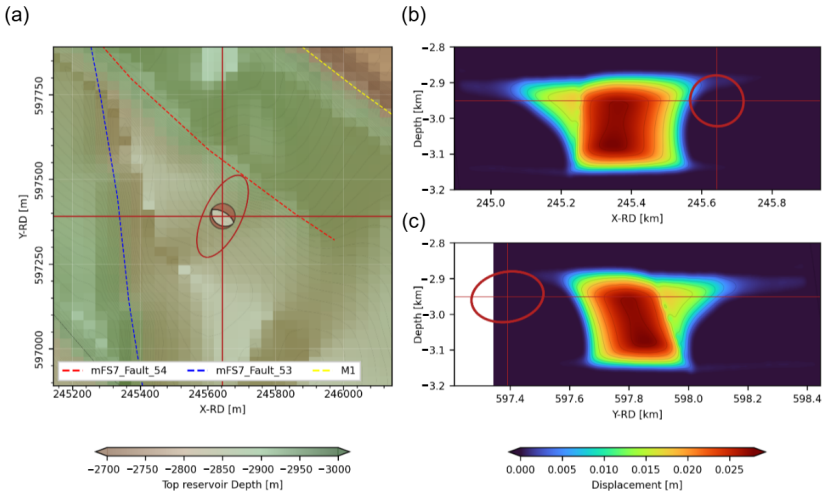

Figure 4.11: (a) The mean location (the intersection of the two red lines) and the covariance (the red ellipse) of the hypocentre inverted from the S waveforms in the field seismograms, shown in the XY-plane. X and Y are longitudinal and latitudinal coordinates, respectively. The background colour represents the depth to the top of the reservoir. (b) The same as (a) but in the XZ-plane. Z is depth. The background colour here is the relative slip of the simulated rupture. (c) As in (b), but viewed in the YZ-plane. The white background indicates the exterior of the geological model.

components. This larger amplitude for the P wave is nicely fitted by the CMT. Furthermore, although only the P waveforms are used in inversion, we observe a very good fit for the S waveforms in the field data. However, probably due to the used 1-D velocity model, the phase difference between synthetic and field S waveforms varies from receiver to receiver, as was discussed in the previous section.

On the other hand, the mean CMT obtained from inversion focusing on the S waveforms in the field data shows an excellent fit for the S waves. The phase difference between the S waveforms corresponding to the mean CMT and the S waveforms in the field data is much smaller compared to that for the P waveforms (Fig. 4.13). We observe a good fit for all three components in all receivers, except for the X and Y components at receiver G184. The S-waveform CMT also provides a good fit for the P waveforms. In comparison with the inversion using only P waveforms in the field data, the posterior distribution for the CMT derived from S waveforms is broader for the moment tensor and the hypocentre. This is because the HMC approach fits S-wave arrivals across all receivers using an inaccurate S-wave model.

Clearly, like the CMT inversion of field seismograms, we can also obtain a point-source representation from the synthetic data through CMT inversion. The resulting hypocentre is indeed located at the centre of the geomechanically simulated rupture zone. The mean moment tensor shows a predominant DC component. The strike, dip, and rake align well with those of the simulated rupture. These, in addition to the excellent waveform fitting, suggest that the inverted CMT from synthetic data can be a good approximation for the simulated rupture. The inversion of field seismic data also pro-

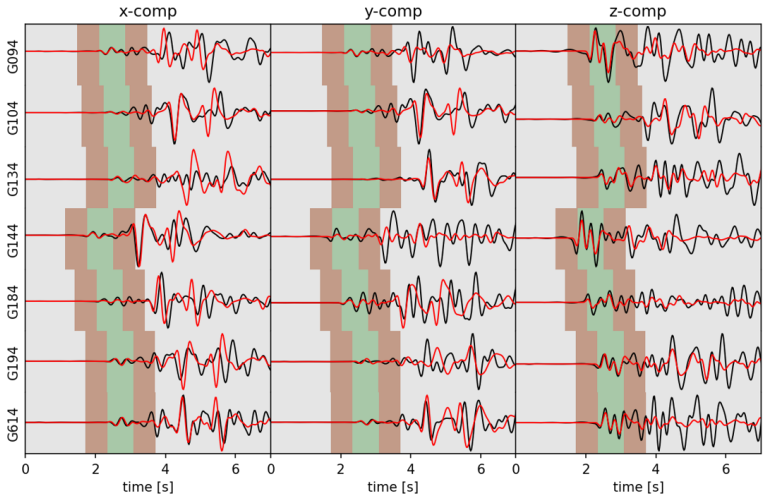

Figure 4.12: Waveform fitting for inversion using the field seismograms. Red traces are waveforms corresponding to the inverted mean CMT. Black traces are the field seismograms from KNMI database. The green-shaded time windows correspond to P waveform. In this part, the amplitude is not tapered for the input. On both sides of this window, we use tapering (the brown-shaded parts) to reduce the amplitude for the input. Data outside the colour-shaded parts is not used in the inversion. The earliest time (the beginning of the left brown-shaded part) is determined from velocity and source-receiver location using an eikonal solver (Masfara et al., 2022).

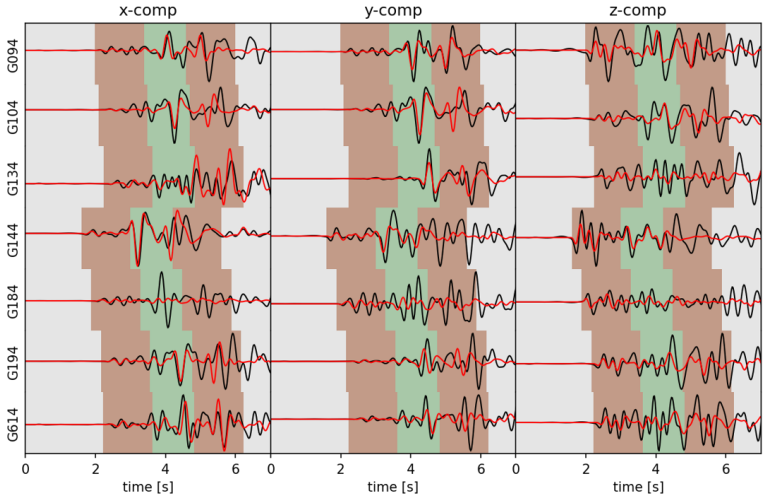

Figure 4.13: Waveform fitting for inversion using the field seismograms. Red traces are waveforms corresponding to the inverted mean CMT. Black traces are the field seismograms from KNMI database. The green-shaded time windows correspond to S waveform. In this part, the amplitude is not tapered for the input. On both sides of this window, we use tapering (the brown-shaded parts) to reduce the amplitude for the input. Data outside the colour-shaded parts is not used in the inversion. The earliest time (the beginning of the left brown-shaded part) is determined from velocity and source-receiver location using an eikonal solver (Masfara et al., 2022).

vides a DC component which conforms with the orientation of the simulated rupture and the hypocentre location.

4.5. DISCUSSION

4.5.1. 1-D LAYERED VELOCITY MODEL OR INACCURATE S-WAVE VELOCITY MODEL?

The phase difference in the S-wave arrivals across the receivers, as shown in Fig. 4.4, could be caused by the 1-D layered velocity model or by an inaccurate S-wave velocity model. It is difficult to determine which one is the main contributor. In Fig. 4.14, we show a comparison between seismograms simulated using 1-D and 3-D velocity models. Minor arrival time differences between the two (1-D and 3-D models) are observed at some receivers, whereas the shear wave arrival time difference is much more significant.

Because the chosen borehole receivers are located within a few kilometres from the hypocentre, the shear waves are very sensitive to the rupture movement and to the vertical heterogeneity in seismic wave velocity. In case there is little uncertainty in the velocity model, as happens for synthetic seismograms generated by a geomechanical rupture model, the obtained posterior distribution from the inversion of synthetic waveforms is reliable. This is reflected by the small standard deviation that we observe in the distribution of the source parameters. When inverting the field seismograms using a highly unreliable velocity model, fitting of full waveforms is difficult due to the phase mismatch between P and S waveforms (Fig. 4.4).

For inversion of field seismograms, we believe that the CMT inversion that fits the P waveforms is more credible because the P-wave velocity model is more reliable. Compared to the result of inversion of S-wave data, the moment tensor and the hypocentre inverted from P-wave data resemble the simulated rupture better in terms of rupture movement and location.

4.5.2. RUPTURE INHOMOGENEITY AND FREQUENCY

The slip along the rupture zone generally varies in space and time. This is captured in geomechanical simulation. For example, the time evolution of the rupture velocity may differ greatly across the nodes located on the slip patch, leading to variations not only in the final slip amplitude but also in the frequency spectrum of the displacement at different nodes across the slip patch. The impact of this inhomogeneity and the small dimension of a finite rupture on the inverted point source remains uncertain. This uncertainty arises because of the approximation of a finite rupture by a point source. This is a valid approximation, given the significant scale difference between the size of the rupture zone and the source–receiver distance. Based on our experience during this research project, we think that the spatio-temporally inhomogeneous rupture velocity and the frequency band chosen for inversion do influence the location of the inverted hypocentre.

We used the 1–4 Hz frequency band for inversion of both synthetic and field data, primarily because of the substantial computational cost associated with simulating the high-frequency seismic signals. For the same reason, the inversion was carried out for a horizontally layered earth model. The frequency range of 1–4 Hz aligns with the prior

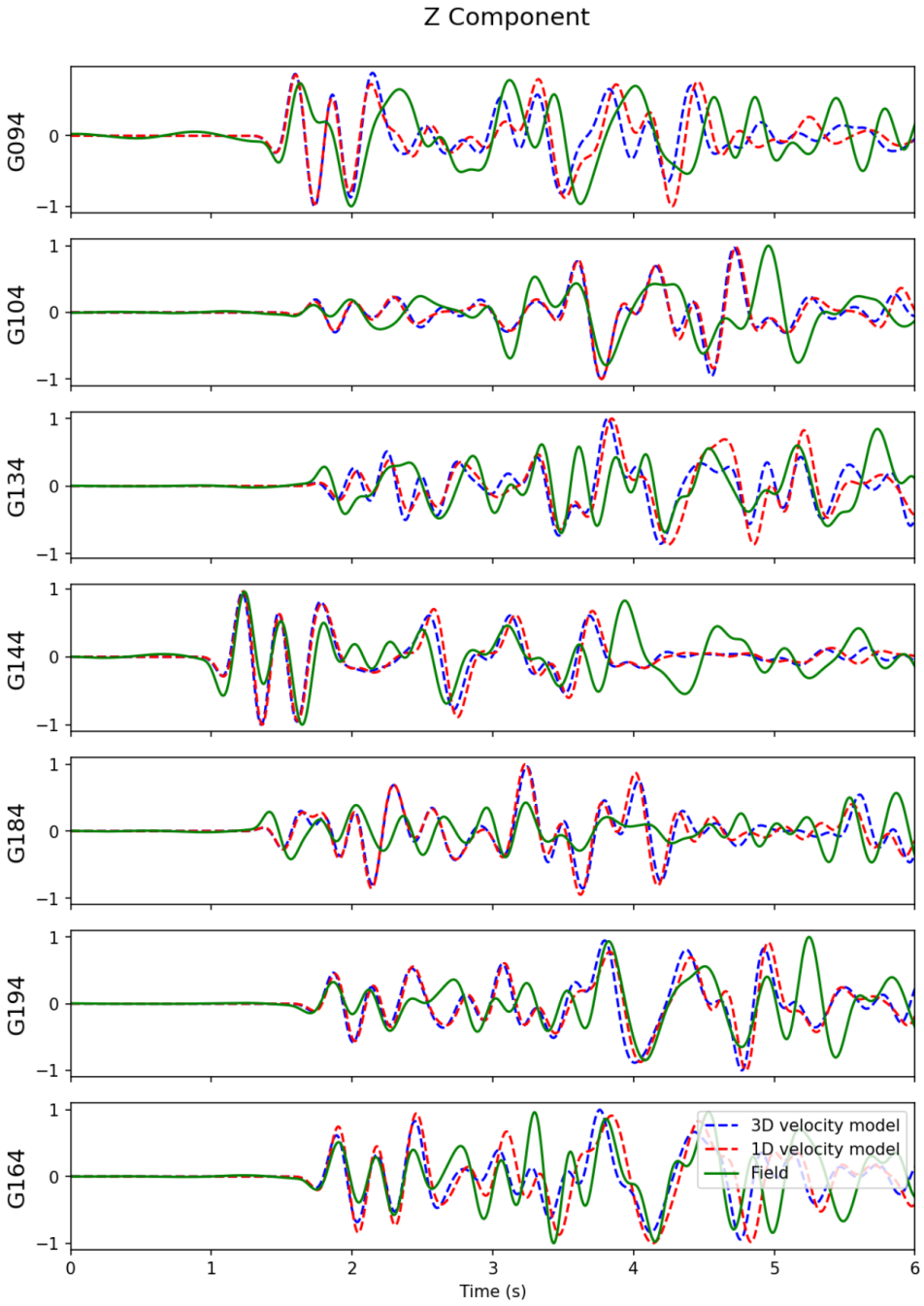

Figure 4.14: Comparison of the waveforms simulated with a 1-D horizontally layered velocity model (red) and 3-D velocity model (blue).

inversion studies conducted in this area (Dost et al., 2020; KNMI, 1993). These prior works encountered similar computational challenges, and those authors opted for a comparable frequency band in the seismic data. For a low-frequency band (larger wavelengths), the difference between using a detailed 3-D velocity model and a 1-D layered-earth model is small.

In this frequency band, the smallest wavelength from the source region (≈ 500 m) is still larger than the length of the finite rupture (≈ 250 m). The posterior distribution of the inversion using synthetic seismograms shows a hypocentre located at the centre of the simulated slip patch. During fault reactivation, the slip amplitude is maximum at this location, and not at the initial slip location.

For the CMT of field seismograms, the hypocentre is located very close to the simulated rupture. Given the uncertainty in the velocity model and the long wavelength, the simulated rupture could indeed represent the dynamic slip that occurred during the 2018 M_L 3.4 Zeerijp earthquake. Any possible relationship between the seismic wavelength and the deduced location of a finite rupture underscores the importance of further investigation into point-source inversion methodologies that employ different seismic frequency bands. This will be further explored in Chapter 5.

The connection between inhomogeneity in the rupture zone and the non-DC component in the inverted moment tensor remains inconclusive. Parameters such as the curvature of the slip patch and the spatio-temporal differences in slip vectors, can contribute to the non-DC components. In our simulations, the slip patch exhibits a centralised distribution with a relatively homogeneous slip amplitude in space in the final stage. Consequently, the inversion using synthetic data reveals a minor (approximately 30%) non-DC component.

4.6. CONCLUSION

We have presented the results of 3-D simulation of the 2018 M_L 3.4 Zeerijp earthquake in Groningen and the resulting synthetic seismograms at seven borehole receivers located near the Zeerijp region in Groningen. We have calculated the synthetic seismograms from the geomechanically simulated rupture. The seismic velocity used for wavefield simulation is sampled at the location of the hypocentre as previously inverted from field seismic data (Dost et al., 2020). Field seismograms at the seven borehole receivers are taken from the KNMI database.

First, we directly compare the synthetic seismograms with the field seismograms. Then both synthetic and field data are used separately for the centroid moment tensor (CMT) inversion assuming a point source. From a comparison of the seismograms and the inverted point sources, we can draw the following conclusions regarding the geomechanical simulation of the fault rupture:

- The filtered synthetic and field seismograms show excellent similarity. This indicates that the rupture movement of the simulated fault is close to that of the actual earthquake. However, there is a phase difference between the S waveforms at some receiver locations. We argue that the phase difference between synthetic and field seismograms is due to the use of an inaccurate S-wave velocity model.

- The inverted CMT of the synthetic seismic data predominantly shows a double-

couple moment tensor with strike, dip and rake similar to those of the geomechanically simulated rupture. The CMT obtained from the field seismic data also shows a similar double-couple component but it is closer to a dip-slip event. The similarity of the DC component between the two CMTs again suggests that our simulated rupture movement is probably close to that of the actual earthquake.

- Both of our inverted CMTs are located at the mFS7-Fault-54 fault, which is the host fault for the simulated rupture. While the CMT obtained from the inversion of the synthetic seismic data is located at the centre of the simulated rupture, the CMT obtained from inversion of the field data shows a location which is slightly east of the simulated rupture. The inverted hypocentres suggest that mFS7-Fault-54 was the host fault for the actual earthquake. The difference in the hypocentre location could be related to the used velocity model, the reservoir geometry, and the initial stress.

- Mean CMTs obtained from both inversions show excellent waveform fitting with the synthetic and the field seismograms. The seismograms obtained from the synthetic-data-derived CMT are nearly identical to the original synthetic seismograms. For the field-data-derived CMT, the waveform fitting is good for both P and S waveforms, but with different phase differences at some of the receivers. This difference is also due to the inaccuracy in the S-wave velocity model that is used in forward simulation.

The similarities between the synthetic and field seismograms and between the corresponding CMTs suggest that our geomechanical simulation of the 2018 M_L 3.4 Zeerijp earthquake is successful in providing an extensive description of the physical model for the reservoir-depletion-induced fault rupture that nicely matches with the seismic observations at the nearby borehole receivers.

5

INVESTIGATING FAULT RUPTURE DYNAMICS THROUGH MOMENT-TENSOR INVERSION USING DIFFERENT FREQUENCY BANDS

Seismic moment-tensor inversion is commonly used in the study of induced seismicity to investigate fault movement during earthquakes, providing a focal mechanism description based on field-observed seismograms. Traditionally, the inverted moment tensor represents a seismic point source. However, this simplified point-source assumption fails to capture critical rupture characteristics, such as the spatial and temporal distribution of the slip across the fault plane. In this study, we demonstrate that by analysing different frequency bands of the seismograms, probabilistic moment-tensor inversion can provide detailed insights into the displacement distribution within the slip patch. We conduct probabilistic inversion on seismograms generated from geomechanical simulations of the earthquake rupture. Our findings indicate that the hypocentre distribution varies with the selected frequency band, effectively reflecting the slip history of the rupture. The patterns observed in the hypocentre distribution exhibit strong similarities between the synthetic seismograms, generated from finite fault simulations and the field-recorded seismograms of the 2018 M_L 3.4 Zeerijp earthquake in Groningen. Notably, by incorporating higher frequencies in the probabilistic moment-tensor inversion, the spatial distribution of the hypocentre shifts from regions of lower slip rates to those of higher slip rates. This finding suggests that probabilistic moment-tensor inversion across different frequency bands provides a novel approach to imaging the rupture process in both space and time. The

This content of this chapter has been submitted to Geophysical Journal International.

insights gained from this approach can significantly enhance our ability to characterise fault behaviour in induced seismic events, offering a more comprehensive understanding of rupture dynamics beyond conventional point-source assumptions.

5.1. INTRODUCTION

Induced earthquakes, often triggered by human activities such as fluid injection or fluid extraction, present significant challenges to the society due to their human, infrastructural, and financial impact. To study induced earthquakes, seismic moment-tensor inversion is widely used. The centroid moment tensors (CMT) derived from the field seismograms offer insights into the focal mechanisms of the earthquake. In traditional moment-tensor inversion, the assumption of a point source on a planar fault is made. However, this assumption has limitations. Due to over-simplification, the moment tensors fail to capture important details of the seismic rupture, such as the spatial and temporal distribution of the slip across the fault.

Building on the findings presented in Chapters 2 and 3, where we simulated geomechanically the induced seismicity incorporating also the 3-D structural complexity in the fault zone, we examine in this chapter the rupture process through moment-tensor inversion. We perform probabilistic moment-tensor inversion across different frequency bands of the seismograms. By analysing the frequency-dependent displacement distribution at the slip patch, we try to obtain deeper insights into the rupture process associated with an induced earthquake.

Several prior studies have highlighted the importance of frequency-dependent analyses in revealing the intricate rupture characteristics of an earthquake. For example, Uchida and Matsuzawa (2013) and Huang et al. (2018) demonstrated that high-frequency components of seismograms can provide useful information about the rupture velocity and slip distribution. Based on dynamic fracture mechanics, Madariaga (1977), Achenbach and Harris (1978) and Beresnev (2017) noted that the radiation from a fault is entirely controlled by the slip velocity field in the ruptured portion of the fault. It was proposed that the radiation of high-frequency waves is controlled by the motion of the slip velocity concentration. Abrupt changes in rupture velocity or stress intensity produce corresponding sharp high-frequency waves. Field seismograms were reported to be dominated by these impulsive waves (Das & Aki, 1977; Madariaga, 1977; Okuwaki et al., 2014; Rudnicki & Kanamori, 1981).

Whereas frequency-dependent analysis of large-scale earthquakes is known to reveal the details and movement of the rupture (e.g., Koper et al. (2011), Yin et al. (2017),Weng and Yang (2018),Liu et al. (2021)), its usefulness for induced earthquakes is less obvious. To this end, we apply our method to both synthetic data from a geomechanically simulated earthquake and the field seismograms from the 2018 ML 3.4 Zeerijp earthquake. This approach allows us to validate the methodology and assess its potential for obtaining greater insights into the slip dynamics.

5.2. RELATIONSHIP BETWEEN RUPTURE MOVEMENT AND RADIATION FREQUENCY

Beresnev (2017) provided an exact formulation for the wavefield generated by a displacement discontinuity in an elastic medium, as described by Aki and Richards (2002):

$$\begin{aligned}\boldsymbol{u}_i(\mathbf{x},t) = \frac{\mu}{4\pi\rho}\iint\Big[&\frac{30\boldsymbol{\gamma}_i\boldsymbol{n}_p\boldsymbol{\gamma}_p\boldsymbol{\gamma}_q\boldsymbol{v}_q - 6\boldsymbol{v}_i\boldsymbol{n}_p\boldsymbol{\gamma}_p - 6\boldsymbol{n}_i\boldsymbol{\gamma}_q\boldsymbol{v}_q}{R^4}\int_{R/\alpha}^{R/\beta} t'\,\Delta\boldsymbol{u}(\boldsymbol{\xi},t-t')\,dt' \\ &+\frac{12\boldsymbol{\gamma}_i\boldsymbol{n}_p\boldsymbol{\gamma}_p\boldsymbol{\gamma}_q\boldsymbol{v}_q - 2\boldsymbol{v}_i\boldsymbol{n}_p\boldsymbol{\gamma}_p - 2\boldsymbol{n}_i\boldsymbol{\gamma}_q\boldsymbol{v}_q}{\alpha^2R^2}\Delta\boldsymbol{u}(\boldsymbol{\xi},t-\tfrac{R}{\alpha}) \\ &-\frac{12\boldsymbol{\gamma}_i\boldsymbol{n}_p\boldsymbol{\gamma}_p\boldsymbol{\gamma}_q\boldsymbol{v}_q - 3\boldsymbol{v}_i\boldsymbol{n}_p\boldsymbol{\gamma}_p - 3\boldsymbol{n}_i\boldsymbol{\gamma}_q\boldsymbol{v}_q}{\beta^2R^2}\Delta\boldsymbol{u}(\boldsymbol{\xi},t-\tfrac{R}{\beta}) \\ &+\frac{2\boldsymbol{\gamma}_i\boldsymbol{n}_p\boldsymbol{\gamma}_p\boldsymbol{\gamma}_q\boldsymbol{v}_q}{\alpha^3R}\Delta\dot{\boldsymbol{u}}(\boldsymbol{\xi},t-\tfrac{R}{\alpha}) \\ &-\frac{2\boldsymbol{\gamma}_i\boldsymbol{n}_p\boldsymbol{\gamma}_p\boldsymbol{\gamma}_q\boldsymbol{v}_q - \boldsymbol{v}_i\boldsymbol{n}_p\boldsymbol{\gamma}_p - \boldsymbol{n}_i\boldsymbol{\gamma}_q\boldsymbol{v}_q}{\beta^3R}\Delta\dot{\boldsymbol{u}}(\boldsymbol{\xi},t-\tfrac{R}{\beta})\Big]\,d\sum(\boldsymbol{\xi})\end{aligned} \tag{5.1}$$

The function $\mathbf{u}_i(\mathbf{x},t)$ represents the i-th component of the radiated displacement at the observation point $\mathbf{x}$, while ξ denotes the location of a point on the fault surface. The displacement discontinuity across the fault is given by $\Delta\mathbf{u}(\xi,t) = \mathbf{u}(\xi,t)\big|_{\Sigma^+} - \mathbf{u}(\xi,t)\big|_{\Sigma^-}$, where Σ^+ and Σ^- represent the two sides of the fault plane. The slip function, defined as $\Delta\mathbf{u}(\xi,t) = \mathbf{n}\cdot\Delta\mathbf{u}(\xi,t)$, characterises the relative displacement between these two sides, and its time derivative, $\Delta\dot{\mathbf{u}}(\xi,t)$, represents the slip rate. Here, $\mathbf{n}$ is the unit vector indicating the slip direction, while ν is the unit vector normal to the fault, oriented from Σ^- to Σ^+. The distance between the observation point and the fault element is given by $R = |\mathbf{x}-\xi|$, and the corresponding unit vector is $\gamma = (\mathbf{x}-\xi)/R$. The parameters α and β denote the propagation speeds of P-waves and S-waves, respectively, while μ and ρ represent the shear modulus and density of the elastic medium.

To analyse the frequency-dependent behaviour of the radiated wavefield, Beresnev (2017) derived the Fourier transform of Eq. 5.1:

$$\begin{aligned}\boldsymbol{u}_i(\mathbf{x},\omega) = \frac{\mu}{4\pi\rho}\Delta\boldsymbol{u}(\omega)\iint U(\boldsymbol{\xi})e^{-i\omega\frac{R}{v}}\Big[&\frac{30\boldsymbol{\gamma}_i\boldsymbol{n}_p\boldsymbol{\gamma}_p\boldsymbol{\gamma}_q\boldsymbol{v}_q - 6\boldsymbol{v}_i\boldsymbol{n}_p\boldsymbol{\gamma}_p - 6\boldsymbol{n}_i\boldsymbol{\gamma}_q\boldsymbol{v}_q}{R^4}t_1(\omega) \\ &+\frac{12\boldsymbol{\gamma}_i\boldsymbol{n}_p\boldsymbol{\gamma}_p\boldsymbol{\gamma}_q\boldsymbol{v}_q - 2\boldsymbol{v}_i\boldsymbol{n}_p\boldsymbol{\gamma}_p - 2\boldsymbol{n}_i\boldsymbol{\gamma}_q\boldsymbol{v}_q}{\alpha^2R^2}e^{-i\omega\frac{R}{\alpha}} \\ &-\frac{12\boldsymbol{\gamma}_i\boldsymbol{n}_p\boldsymbol{\gamma}_p\boldsymbol{\gamma}_q\boldsymbol{v}_q - 3\boldsymbol{v}_i\boldsymbol{n}_p\boldsymbol{\gamma}_p - 3\boldsymbol{n}_i\boldsymbol{\gamma}_q\boldsymbol{v}_q}{\beta^2R^2}e^{-i\omega\frac{R}{\beta}} \\ &+\frac{2\boldsymbol{\gamma}_i\boldsymbol{n}_p\boldsymbol{\gamma}_p\boldsymbol{\gamma}_q\boldsymbol{v}_q}{\alpha^3R}i\omega e^{-i\omega\frac{R}{\alpha}} \\ &-\frac{2\boldsymbol{\gamma}_i\boldsymbol{n}_p\boldsymbol{\gamma}_p\boldsymbol{\gamma}_q\boldsymbol{v}_q - \boldsymbol{v}_i\boldsymbol{n}_p\boldsymbol{\gamma}_p - \boldsymbol{n}_i\boldsymbol{\gamma}_q\boldsymbol{v}_q}{\beta^3R}i\omega e^{-i\omega\frac{R}{\beta}}\Big]\,d\sum(\boldsymbol{\xi})\end{aligned} \tag{5.2}$$

Eq. 5.2 highlights that the primary source of high-frequency radiation from the fault is the source time function, while the static slip distribution $\mathbf{U}(\xi)$, which is the Fourier transform of the slip function $\Delta\mathbf{u}(\xi, t)$, primarily acts as a modulating factor. However, the exact extent of $\mathbf{U}(\xi)$'s influence can only be determined through precise numerical integration.

5.3. FREQUENCY BAND USED IN CMT INVERSION AND THE HYPOCENTRE DISTRIBUTION

In Chapter 4, we discussed the result of probabilistic moment-tensor inversion for the centroid moment tensor (CMT) of the 2018 M_L 3.4 Zeerijp event using synthetic seismograms at borehole receiver locations generated by a geomechanical simulation. Then we conducted moment-tensor inversion using the field seismograms recorded at the same borehole receivers. A frequency filter of 1–4 Hz was applied before inversion. The inversion results from the synthetic seismograms revealed a CMT distribution centred within the simulated slip patch, whereas the inversion of field seismograms indicated a CMT distribution located slightly outside the slip patch but still along the same fault.

The primary source of the seismic signal in our studies is attributed to fault reactivation associated with the induced earthquake. Our investigation of the Zeerijp event found that this simulated fault reactivation is in agreement with the moment magnitude, depletion values, and the event location of the actual 2018 M_L 3.4 Zeerijp earthquakes. The simulated seismic event initiates near the top of the reservoir and propagates downwards, with the slip amplitude increasing towards the centre of the fault patch before gradually decreasing toward the lower boundary.

In this chapter we further investigate if the slip history, which affects the frequency spectrum of the radiation, can be addressed through CMT inversion using different frequency bands of the seismograms. To that end, we first conduct an investigation using synthetic seismograms generated from the geomechanical simulation of the 2018 M_L 3.4 Zeerijp event, which also takes the 3-D fault-zone complexity obtained from earlier seismic inversion into account. The seismic source is the geomechanically simulated seismic slip. Next, we extend this investigation to CMT inversion using field seismograms to examine the correlation with the results obtained from the synthetic data from the geomechanically simulated rupture.

5.3.1. CMT INVERSION USING SYNTHETIC SEISMOGRAMS FROM THE SIMULATED RUPTURE

For this inversion, we select a lower frequency of 0.1 Hz, while the upper frequency ranges from 1.5 Hz to 4.0 Hz. With the chosen grid spacing and time step in the wavefield simulation, the synthetic seismograms were generated with a maximum frequency of 80 Hz. However, due to computational constraints, the elementary seismograms were limited to a maximum frequency of 15 Hz. The upper limit of 4.0 Hz for CMT inversion is thus adequate, ensuring comprehensive coverage of the relevant frequency ranges. We taper the seismograms with a 4-second time window, beginning at the first P-wave arrival and extending to the end of the surface-reflected S-wave.

We follow the same workflow for CMT inversion as used in Chapter 4. Fig. 5.1 shows

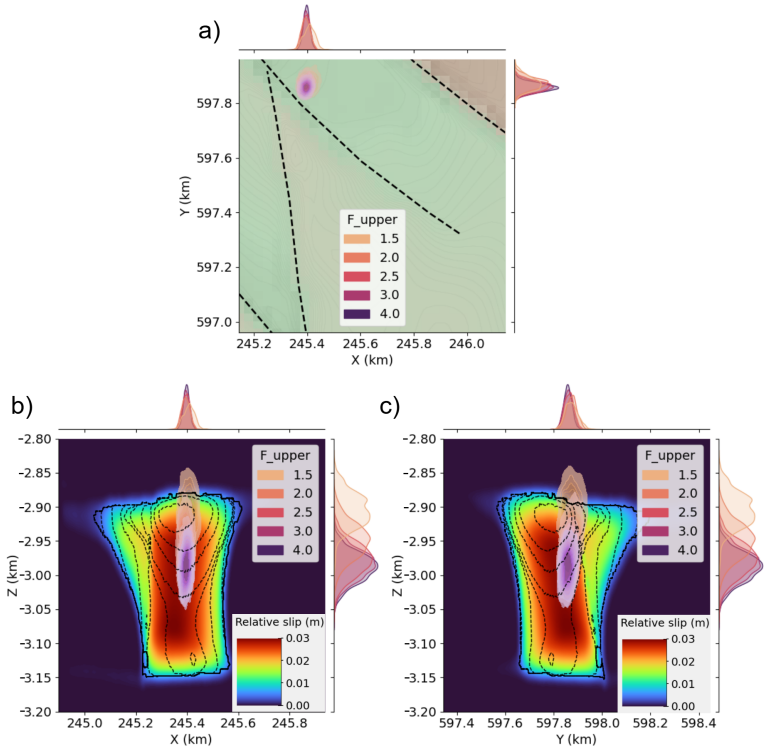

Figure 5.1: a): Inverted hypocentre for the Zeerijp event using synthetic seismograms shown in map view with reservoir depth as background. b) and c): Inverted hypocentre for the Zeerijp event using field seismograms shown on XZ- and YZ-fault plane with relative slip amplitude as background. The contour lines depict the progression of the rupture front over time, spanning from 0 to 1 second in intervals of 0.05 seconds. The background colour of b) and c) represents the final relative slip at the main fault. Results are shown for different upper frequency (F_upper) values: 1.5 Hz, 2.0 Hz, 2.5 Hz , 3.0 Hz, 4.0 Hz. X is east, Y is North, Z is depth. The colour-scale shown for F_upper refers to the distribution of the hypocentres, while the colour-scale marked for relative slip refers to the slip distribution.

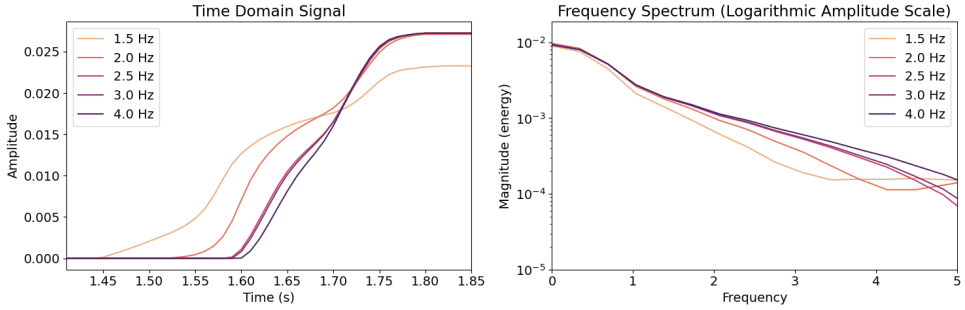

Figure 5.2: Left: Relative slip amplitude. Right: the corresponding frequency spectrum at the mean hypocentre inverted from the synthetic seismograms of the Zeerijp event using different upper frequencies.

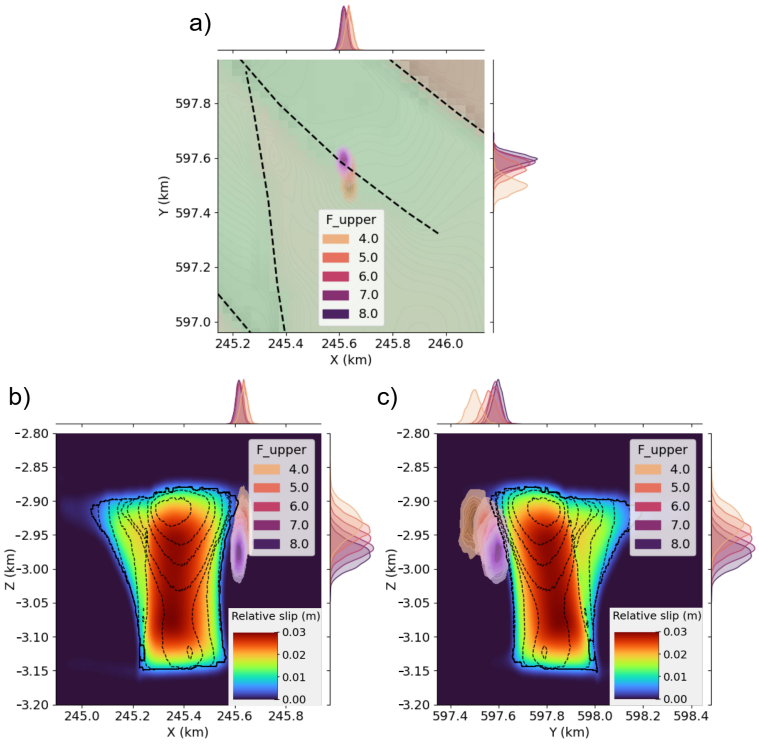

Figure 5.3: Same as Fig. 5.1 but for the field seismograms instead of the synthetic data.

the results. We notice that, with increasing higher frequencies, the hypocentre distribution shifts from the initial slip location to the centre of the slip patch. This can be explained by the fact that the high-frequencies wave generated by the rapid slip at the centre of the slip patch, as supported by Eq. 5.2. This is also captured by incorporating higher frequencies in the CMT inversion. Figure 5.2 shows the relative slip and the corresponding frequency spectrum at the hypocentres from the mean CMT solutions.

5.3.2. CMT INVERSION USING FIELD-OBSERVED SEISMOGRAMS

Here, we use seismograms recorded by borehole receivers at 200-m depth. The data were obtained from the KNMI database for the 2018 ML 3.4 induced earthquake in the Zeerijp region.

Most of the energy from the local earthquakes is concentrated in the frequency range of 1 to 10 Hz (van Ginkel et al., 2022). For field seismograms, we use a lower frequency cutoff of 1 Hz and the upper frequency ranges between 4.0 and 8.0 Hz. Setting an upper frequency less than 4.0 Hz, as was done for CMT inversion of the synthetic seismograms, does not provide enough information for accurate inversion. For example, a frequency band of 1 to 1.5 Hz fails to offer sufficient resolution to capture the fault movement during the seismic event. Here we use a 4-second time window to taper the field seismo-

grams. This window extends from the first P-wave arrival to the surface-reflected S-wave arrival, thus incorporating most of the relevant information and ensuring accurate fitting with the calculated Green's function.

The probabilistic distribution of the CMT obtained from inversion using different upper frequency values is shown in Figure 5.3. Similar to the results presented in Chapter 4, the inverted hypocentres are located slightly outside the slip patch. As the upper frequency limit increases from 4.0 Hz to 8.0 Hz, the hypocentre shifts from the location near the initial slip patch to close to the centre of the slip patch. This pattern of movement of the inverted hypocentre is same as that found on the synthetic seismograms for the simulated rupture (Fig. 5.1).

The correlation between the hypocentre distribution and the upper frequency value is consistent for both synthetic and field seismograms. In both cases, the distribution shifts from near the initial slip patch to the centre of the slip patch. This finding suggests that our geomechanical simulation captures rupture dynamics during induced earthquake, including the pattern of rupture propagation and the resulting slip.

5.3.3. WAVEFORM FITTING RESULT

We examine the quality of waveform fitting for both synthetic data from geomechanically-simulated rupture and field seismic data, for the upper frequency value of 4 Hz and 8 Hz. The results are shown in Figs. 5.4 and 5.5. Both waveform fits exhibit excellent agreement across all receivers. This confirms that our CMT inversion accurately captures the source dynamics. The CMT inversion results for synthetic and observed data demonstrate an excellent match in waveform fitting within the 4-second time window. For the fitting of the synthetic waveforms, the fit remains highly consistent beyond this window. The CMT inversion results for synthetic and observed data show an excellent match in waveform fitting within the 4-second time window. However, for field-observed waveforms, the similarity decreases after the first S-wave arrival. This discrepancy is attributed to the complexity of the near-surface seismic velocity model, which affects the arrival of surface-reflected waves and subsequent waveform characteristics.

5.4. RUPTURE PROPAGATION VERSUS SLIP DIRECTION

Schmedes and Archuleta (2008) noted that, for a given seismic station and a specific point on the fault, the arrival time — also referred to as the isochrone time — is the sum of two components: the time required for the rupture front to reach that point on the fault, and the seismic wave travel time from that point to the receiver.

Based on this principle, for a fault dipping at 66°, rupture propagation in the lateral direction is expected to be more easily resolved by the surface receivers than propagation in the dip direction, assuming similar rupture front velocities. This is because the lateral rupture leads to a longer rupture front propagation time relative to the receiver layout.

To investigate how rupture propagation direction influences our inversion results, we simulate four dynamic rupture scenarios. Each model combines different slip directions and rupture front orientations, allowing us to explore their respective effects on the resulting seismic waveforms.

We initiate the simulation by manually assigning the shear and the normal stress on

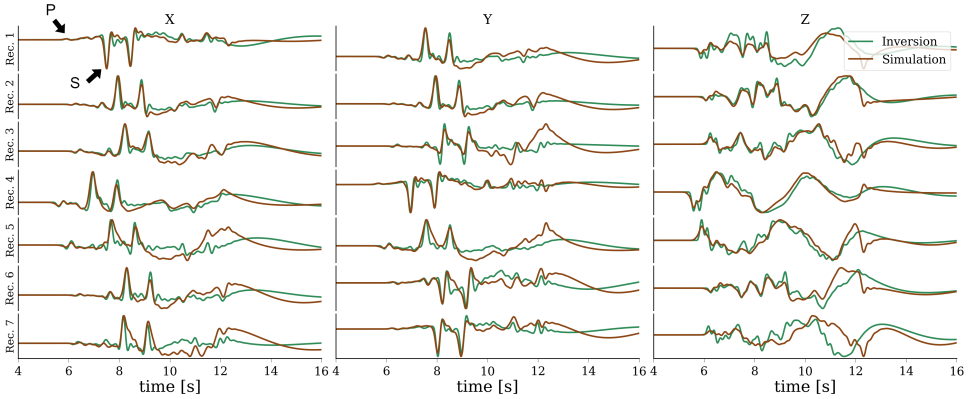

Figure 5.4: Waveform fitting for CMT inversion using synthetic seismograms (0.1 – 4 Hz). Green traces represent waveforms from the mean inverted CMT, while brown traces show synthetic seismograms from the geomechanically simulated finite rupture.

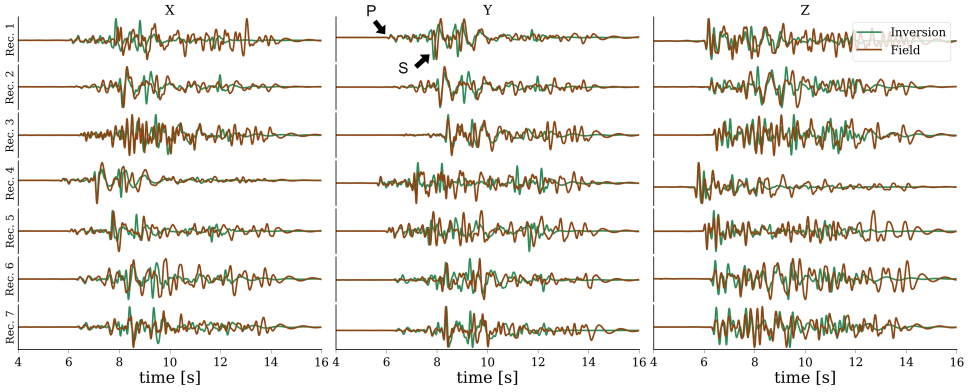

Figure 5.5: Waveform fitting for inversion using field seismograms (1 – 8 Hz). Green traces represent waveforms from the mean inverted CMT, while brown traces show the field (borehole) seismograms.

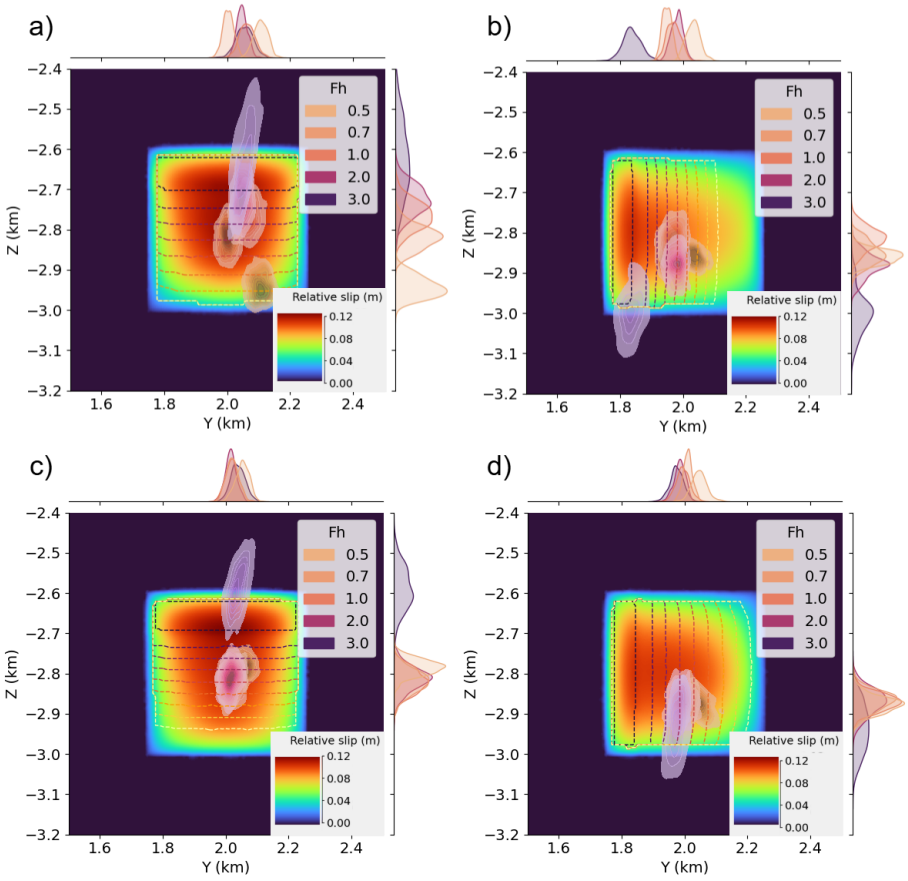

Figure 5.6: Inverted hypocentre for the simplified geomechanical model using synthetic seismograms. Results are shown for different upper frequency (Fh) value with relative slip amplitude as background and rupture propagation as dashed contours. The contour lines, shaded from dark to light, represent the progression of the rupture front over time, spanning from 0 to 0.2 seconds in intervals of 0.02 seconds. a) Dip slip with propagation in the dip direction. b) Dip slip with propagation in the strike direction. c) Strike slip with propagation in the dip direction. d) Strike slip with propagation in the strike direction.

a predefined 400 m × 400 m slip patch located at the centre of the fault. To control slip and rupture propagation, a 100 m-wide boundary region on the slip patch is assigned a critical stress condition to initiate the rupture. The remaining area within the slip patch is set to a near-critical state. In the area, the shear-capacity-utilization (SCU) value gradually decreases from 0.95 to 0.85 as it approaches the opposite boundary. To prevent fault slip outside the defined patch, we impose near-zero shear stress in the surrounding regions.

The rupture propagation and slip directions can be either down-dip or lateral, resulting in four possible combinations. In each scenario, the simulated rupture starts at the predefined slip patch and terminates at the patch boundary, producing a time- and space-dependent distribution of the slip amplitude. Figure 5.6 illustrates the rupture propagation and the final slip amplitude on the fault plane. The nearly constant velocity of the rupture front is evident from the density of the dashed contour lines. The initial slip patch exhibits the largest slip amplitude.

Figure 5.6 illustrates the distribution of the inverted hypocentres, for different higher frequency limits, derived from the seismograms generated from four different geomechanically-simulated rupture patterns. For all cases, increasing the maximum frequency results in the hypocentre shifting closer to the initial slip patch. This trend mirrors the correlation observed in the 2018 Zeerijp earthquake CMT inversion (Figure 5.3), where higher frequencies correspond to hypocentres moving toward areas with faster slip.

From the results, the difference in rupture propagation direction does not appear to influence significantly the shift of the inferred hypocentre. At the very least, no clear or consistent trend is observed. One possible explanation for this subtlety is the relatively small fault area involved, especially when compared to the full simulation domain. Additionally, the seismic receivers are distributed laterally at a depth of 200 m near the epicentre. This configuration offers limited vertical coverage and, therefore, reduced sensitivity to the rupture propagation in the vertical direction.

5.5. CONCLUSION

In this study, we have investigated the effect of frequency ranges used in the CMT inversion on the spatial distribution of the inverted hypocentre. We observe that by including higher frequencies in the inversion, the hypocentre distribution shifts from regions with a lower slip rate to areas with higher slip rates. This correlation was consistently observed for the CMT inversion of both synthetic and field seismograms for the 2018 M_L 3.4 Zeerijp event.

Through additional CMT inversions using seismograms generated from different rupture patterns with uniform rupture velocity, we confirm the effect of slip velocity on the inverted hypocentre. Our findings suggest that neither the rupture propagation direction nor the slip orientation significantly influences the inverted hypocentre. Instead, the shift observed when higher frequencies are used can be attributed to the fact that fast slip generates seismic sources with higher frequency components as postulated in prior theoretical studies (e.g., Madariaga (1977)). Inversions using both P and S waves tend to fit the waveforms better when the hypocentre is placed closer to the high-frequency source region.

These observations provide new insights on how the rupture process can be investigated through field seismic observations by altering the frequency composition of the used seismic waves used in the CMT inversion. By focusing on higher frequency bands in inversion, it is possible to determine more accurately the spatial distribution of slip during an earthquake.

6

CONCLUSIONS AND SUGGESTIONS FOR FUTURE WORK

6.1. CONCLUSIONS

This thesis presents an extensive investigation into the effects of reservoir structures and fault intersections on the occurrence of induced earthquakes through a series of 3-D geomechanical simulations. By systematically analysing their influence on the induced stress distribution and the resulting rupture pattern, we have reached an improved understanding of how the reservoir geometry controls the occurrence of the induced earthquakes after reservoir depletion, for example, in the Groningen gas field.

In Chapter 2, we investigated the role of 3-D reservoir geometry, focusing on the horst structures formed by two intersecting faults. Our analysis revealed that the intersection angle of these faults significantly affects the induced stress field and the subsequent dynamic rupture process. We found that smaller intersection angles concentrate shear stress in the dip direction, increasing the likelihood of rupture initiation at the lower reservoir juxtaposition. The dynamic simulations further showed that the intersection angle of the faults determines the induced stress heterogeneity at the intersection, influencing the slip pattern and the maximum slip location. These findings highlight the need to account for complex geological features in the geomechanical models in order to reliably predict the seismic behaviour.

In Chapter 3, we explored the potential for rupture migration across intersecting faults by implementing the crosslink constraint method in 3-D geomechanical simulations. Our study showed that the interaction is governed by the orientation of the faults and their relative stress states, with rupture migration occurring more readily at smaller intersection angles. We also analysed the impact of different boundary conditions and fault friction properties on the migration process. Our findings suggest that the rupture transfer could lead to cascading fault reactivations in regions with complex fault networks, emphasizing the importance of understanding the fault connectivity in seismic hazard assessments.

It is not possible to directly validate the geomechanical simulation of an induced earthquake, since there is no direct observation of the underground rupture. However, indirect validation is possible through the use of exploration seismic data. The simulated seismic data from the geomechanical simulation of a prior seismic event can be used to compare with the field observed seismograms.

In Chapter 4, by combining seismic wave propagation simulation caused by dynamic rupture and seismic moment-tensor inversion, we established a workflow to validate a geomechanical simulation. As a case study, we validated our geomechanical model on the 2018 M_L 3.4 Zeerijp earthquake. A comparison of the synthetic seismograms generated from our 3-D simulations with the field-recorded data showed a strong correlation in waveform patterns, peak amplitudes, and arrival times. Furthermore, both synthetic and observed waveforms were used for seismic moment-tensor inversion, resulting in a high degree of similarity in terms of double-couple orientations and hypocentre locations. Both inverted moment tensors correspond to the fault mFS7-Fault-54, which is the host (main) fault in the geomechanical simulation, as also suggested in previous moment-tensor inversion studies for this earthquake.

To further explore the relationship between moment-tensor inversion and finite rupture behaviour, Chapter 5 investigates the influence of frequency content on both moment-tensor inversion and hypocentre estimation. We perform inversions using both synthetic seismograms from geomechanically simulated rupture and field-observed waveforms from the 2018 M_L 3.4 Zeerijp earthquake, applying different upper-frequency limits. The results show that the inverted hypocentre location shifts toward the initial slip patch when higher frequency bands are used. This region is associated with higher slip rates, consistent with predictions from previous theoretical studies.

Specifically, the higher frequency bands tend to shift the hypocentre towards the centre of the rupture area, which has a faster rupture-front velocity as well as a larger slip amplitude, whereas the lower frequency components locate the hypocentre closer to the initial slip region, which has a slower rupture-front velocity as well as a smaller slip amplitude. This behaviour was observed in both the synthetic data from geomechanical simulation and the field data, confirming that the frequency range of the seismic waves used in moment-tensor inversion plays a critical role in hypocentre determination. Our study also examined the relationship between rupture propagation direction and slip orientation, revealing that these factors have a minor influence on the inverted hypocentre location compared to the frequency content of the seismic signals. Similar to the relationship identified in strong tectonic earthquakes, these findings reveal the possibility of estimating the finite rupture process through seismic moment-tensor inversion by fitting seismic waveforms across different frequency ranges, also for the induced earthquakes of smaller magnitudes.

6.2. SUGGESTIONS FOR FUTURE INVESTIGATION

Geomechanical simulation of induced earthquakes generally involves information on underground structures. Depending on the resolution of the application, the currently available data are insufficient for accurate simulation of the induced earthquakes. For example, when we simulate the 2018 M_L 3.4 Zeerijp event, we implement the initial stress based on the regional stress. However, this is an extremely simplified and linear

implementation, as this does not take into account the tectonic history of the region, as well as the generation of the faults and the subsequent reactivation, which are highly nonlinear. Furthermore, fault reactivation in case of induced earthquakes requires an adequate length (or size) for the aseismic slip patch to be generated by long-term pore-pressure depletion. However, initial stress also plays a very important role in triggering the reactivation. Therefore, in order to simulate a prior seismic event or predict an induced earthquake due to production activities, it is necessary to have a reliable and detailed initial stress model.

In this thesis, we adopted the linear slip-weakening law, as it has been extensively used in previous 2-D numerical modelling studies of induced seismicity in the Groningen gas field. Our primary focus in this study was on the effects of 3-D fault geometry and on dynamic rupture simulation. To minimize the uncertainties from additional sources, we chose to implement the slip-weakening law as a foundation for our analysis. While the linear slip-weakening law provides a simplified representation of the fault behaviour, the rate-and-state friction law is increasingly being used in induced seismicity simulations. Originally developed for studying tectonic earthquakes, rate-and-state friction has gained popularity in modelling induced seismicity, both in individual physical simulations and in large-scale statistical assessments of production regions. Its growing application highlights the importance of capturing the time-dependent and evolving nature of fault slip in response to reservoir depletion and fluid extraction.

While an increasing number of laboratory studies have been conducted on the frictional behaviour of fractures, greatly contributing to the validation of frictional fault simulations, experimental studies involving two or more intersecting fractures remain scarce. Since faults typically occur as part of complex fault zones containing intersecting structures, conducting such experiments would provide valuable insights into fault interactions. This, in turn, would facilitate the validation of simulations involving fault intersections and ultimately improve the accuracy of 3-D geomechanical simulations of induced seismicity.

3-D geomechanical simulation of dynamic rupture and moment-tensor inversion provides a powerful tool for studying the relationship between point-source representation and finite-rupture sources. In this thesis, we establish a workflow to explore this relationship, with a particular focus on the hypocentre distribution and the frequency content of the input seismograms. Further research should be conducted to deepen the understanding of this relationship, including investigations into moment-tensor composition and the rupture homogeneity, directivity, and the influence of slip patch size and shape.

Furthermore, boreholes that penetrate the reservoir can, in principle, provide near-field seismograms that can be directly compared with simulated seismograms. This additional data source offers an opportunity to introduce additional constraints for waveform fitting in moment-tensor inversion, enhancing the accuracy and reliability of the inversion results.

The Groningen gas field benefits from a dense network of borehole geophones, providing extensive borehole data that have been available since 2017 following the installation of the G-network. This network, operated by KNMI, consists of 79 stations, including 69 borehole stations, offering a comprehensive dataset for studying induced earth-

quakes in Groningen. The wealth of recorded data from induced earthquakes presents significant opportunities for conducting numerous case studies. These studies can further refine the proposed workflow and contribute to a deeper understanding of the mechanisms driving induced seismicity, ultimately improving seismic hazard assessment and mitigation strategies.

ACKNOWLEDGEMENTS

This research was part of the "DeepImage" project, funded by NWO Science domain (NWO-ENW), project DEEP.NL.2018.048. This project aims to improve the forecasting of ground motion in Groningen, caused by possible future earthquakes.

I have had a great time throughout my PhD research and while completing my thesis. This period has been profoundly meaningful for me, allowing me to develop essential skills like critical thinking, independence, and resourcefulness. I now realize that these qualities are highly applicable and valuable, both in my professional career and in my daily life.

I also gained valuable scientific knowledge, learned new methods, and adopted fresh ways of thinking from the many colleagues I had the good fortune to work with during my research. Moreover, I benefitted greatly from the unwavering support of the people around me during this period. This backing was truly essential for me to continue with my work and overcome all challenges. I cannot express sufficiently with words my profound gratitude to them.

Above all, I would like to express my deepest gratitude to my promotors, **Ranajit Ghose** and **Wim Mulder**, for their kind and continuous guidance. In all these years, I was encouraged to strive such that impact and innovations were at the core of the work, an attitude that has been extremely helpful for me.

Next I would like to thank **Chunfang Meng**, who provided a great amount of help with the simulation tool (Defmod-OpenSWPC) that is used in this research. It is a fantastic tool for earthquake simulation which was crucial to my modelling work.

I would like to extend my sincere gratitude to my colleagues in the DeepNL office for sharing so many fun memories and kindness, and for supporting each other. I thank **Iban** for the expert guidance and assistance with the moment tensor inversion. My thanks also go to **Aleks** and **Hamed** for their significant help with the simulations and invaluable advice on numerical problems. I am also grateful to **Aukje** and **Faezeh** for the morning coffee session. I thank **Milad** not only for his expertise in the laboratory experiments on rock behaviour but also for being a great friend who encouraged me to become better. My appreciation also goes out to the many colleagues in other DeepNL projects for generously sharing their knowledge and providing valuable feedback.

I also extend my sincere gratitude to the faculty of Civil Engineering and Geosciences. Many thanks to **Kees Wapenaar**, **Kees Weemstra**, and **Jan-Dirk Jansen** for sharing their valuable knowledge and expertise. Additionally, many thanks go to the support staff whose dedicated efforts are greatly appreciated.

Finally, I would like to express my deepest gratitude to my parents for their support throughout this journey. My heartfelt thanks also go to **Olga** for her patience and encouragement during the last phase of the PhD journey.

BIBLIOGRAPHY

Achenbach, J., & Harris, J. (1978). Ray method for elastodynamic radiation from a slip zone of arbitrary shape. *Journal of Geophysical Research: Solid Earth*, *83*(B5), 2283–2291.

Aki, K., & Richards, P. G. (2002). *Quantitative seismology*.

Beresnev, I. A. (2017). Factors controlling high-frequency radiation from extended ruptures. *Journal of Seismology*, *21*, 1277–1284.

Biot, M. A. (1941). General theory of three-dimensional consolidation. *Journal of applied physics*, *12*(2), 155–164.

Buijze, L., Van den Bogert, P., Wassing, B., & Orlic, B. (2019). Nucleation and arrest of dynamic rupture induced by reservoir depletion. *Journal of Geophysical Research: Solid Earth*, *124*(4), 3620–3645.

Candela, T., Osinga, S., Ampuero, J.-P., Wassing, B., Pluymaekers, M., Fokker, P. A., van Wees, J.-D., de Waal, H. A., & Muntendam-Bos, A. G. (2019). Depletion-induced seismicity at the Groningen gas field: Coulomb rate-and-state models including differential compaction effect. *Journal of Geophysical Research: Solid Earth*, *124*(7), 7081–7104.

Cotton, F., & Coutant, O. (1997). Dynamic stress variations due to shear faults in a plane-layered medium. *Geophysical Journal International*, *128*(3), 676–688.

Das, D., & Mallik, J. (2020). Koyna earthquakes: A review of the mechanisms of reservoir-triggered seismicity and slip tendency analysis of subsurface faults. *Acta Geophysica*, *68*(4), 1097–1112.

Das, S., & Aki, K. (1977). A numerical study of two-dimensional spontaneous rupture propagation. *Geophysical journal international*, *50*(3), 643–668.

Day, S. M., Dalguer, L. A., Lapusta, N., & Liu, Y. (2005). Comparison of finite difference and boundary integral solutions to three-dimensional spontaneous rupture. *Journal of Geophysical Research: Solid Earth*, *110*(B12).

DeDontney, N., & Lele, S. (2018). *Impact of production fluctuations on Groningen seismicity-geomechanical modelling using rate and state friction* (tech. rep.). Nederlandse Aardolie Maatschappij BV. https://nam-onderzoeksrapporten.data-app.nl/reports/download/groningen/en/6b2e9b94-a995-4089-864a-67ec5ffda839

DIANA. (2016). *DIANA – Finite Element Analysis, User's Manual Release 10.1*. Delft, The Netherlands. https://dianafea.com

Dieterich, J. H. (1979). Modeling of rock friction: 1. experimental results and constitutive equations. *Journal of Geophysical Research: Solid Earth*, *84*(B5), 2161–2168.

Dost, B., Edwards, B., & Bommer, J. J. (2018). The relationship between M and M_L: A review and application to induced seismicity in the Groningen gas field, the Netherlands. *Seismological Research Letters*, *89*(3), 1062–1074.

Dost, B., van Stiphout, A., Kühn, D., Kortekaas, M., Ruigrok, E., & Heimann, S. (2020). Probabilistic moment tensor inversion for hydrocarbon-induced seismicity in

the Groningen gas field, the Netherlands, Part 2: Application. *Bulletin of the Seismological Society of America*, *110*(5), 2112–2123.

Engelder, T., & Fischer, M. P. (1994). Influence of poroelastic behavior on the magnitude of minimum horizontal stress, s h in overpressured parts of sedimentary basins. *Geology*, *22*(10), 949–952.

Fukuyama, E. (2015). Dynamic faulting on a conjugate fault system detected by near-fault tilt measurements. *Earth, Planets and Space*, *67*, 1–10.

Galis, M., Pelties, C., Kristek, J., Moczo, P., Ampuero, J.-P., & Mai, P. M. (2015). On the initiation of sustained slip-weakening ruptures by localized stresses. *Geophysical Journal International*, *200*(2), 890–909.

Geuzaine, C., & Remacle, J.-F. (2009). Gmsh: A 3-D finite element mesh generator with built-in pre-and post-processing facilities. *International Journal for Numerical Methods in Engineering*, *79*(11), 1309–1331.

Hincks, T., Aspinall, W., Cooke, R., & Gernon, T. (2018). Oklahoma's induced seismicity strongly linked to wastewater injection depth. *Science*, *359*(6381), 1251–1255.

Huang, Z., Li, X., Li, S., Zhao, K., & Zhang, R. (2018). Investigation of the hydraulic properties of deep fractured rocks around underground excavations using high-pressure injection tests. *Engineering Geology*, *245*, 180–191.

Hunfeld, L. B., Niemeijer, A. R., & Spiers, C. J. (2017). Frictional properties of simulated fault gouges from the seismogenic Groningen gas field under in situ P–T-chemical conditions. *Journal of Geophysical Research: Solid Earth*, *122*(11), 8969–8989.

Jansen, J.-D., & Meulenbroek, B. (2022). Induced aseismic slip and the onset of seismicity in displaced faults. *Netherlands Journal of Geosciences*, *101*.

KNMI. (1993). Netherlands seismic and acoustic network. Royal Netherlands Meteorological Institute (KNMI). *Other/Seismic Network*.

Koper, K. D., Hutko, A. R., Lay, T., Ammon, C. J., & Kanamori, H. (2011). Frequency-dependent rupture process of the 2011 Mw 9.0 Tohoku earthquake: Comparison of short-period P wave backprojection images and broadband seismic rupture models. *Earth, planets and space*, *63*, 599–602.

Kühn, D., Hainzl, S., Dahm, T., Richter, G., & Rodriguez, I. V. (2022). A review of source models to further the understanding of the seismicity of the Groningen field. *Netherlands Journal of Geosciences*, *101*.

Li, J., Kuehl, H., Droujinine, A., & Blokland, J.-W. (2016). Microseismic and induced seismicity simultaneous location and moment tensor inversion: Moving beyond picks with a robust full-waveform method. In *Seg technical program expanded abstracts 2016* (pp. 2535–2539). Society of Exploration Geophysicists.

Lin, A., & Chiba, T. (2017). Coseismic conjugate faulting structures produced by the 2016 mw 7.1 Kumamoto earthquake, Japan. *Journal of Structural Geology*, *99*, 20–30.

Liu, W., Yao, H., & Wei, S. (2021). Frequency-dependent rupture characteristics of the 30 october 2016 Mw 6.5 Norcia, Italy earthquake inferred from joint multi-scale slip inversion. *Journal of Geophysical Research: Solid Earth*, *126*(5), e2020JB–020706.

Madariaga, R. (1977). High-frequency radiation from crack (stress drop) models of earthquake faulting. *Geophysical Journal International*, *51*(3), 625–651.

Maeda, T., Takemura, S., & Furumura, T. (2017). *OpenSWPC: An open-source integrated parallel simulation code for modeling seismic wave propagation in 3D heterogeneous viscoelastic media* (tech. rep.). Springer.

Maerten, L., Willemse, E. J., Pollard, D. D., & Rawnsley, K. (1999). Slip distributions on intersecting normal faults. *Journal of Structural Geology*, *21*(3), 259–272.

Mahmoud, A. A., Elkatatny, S., Ali, A., & Moussa, T. (2019). Estimation of static young's modulus for sandstone formation using artificial neural networks. *Energies*, *12*(11), 2125.

Masfara, L. O. M., Cullison, T., & Weemstra, C. (2022). An efficient probabilistic workflow for estimating induced earthquake parameters in 3D heterogeneous media. *Solid Earth*, *13*(8), 1309–1325.

Masfara, L. O. M., & Weemstra, C. (2024). Hamiltonian monte carlo to characterize induced earthquakes: Application to a M_L 3.4 event in the Groningen gas field and the role of prior. *Earth and Space Science*, *11*(1), e2023EA003184.

Meng, C. (2017). Benchmarking Defmod, an open source FEM code for modeling episodic fault rupture. *Computers & Geosciences*, *100*, 10–26.

Meng, C., & Hager, B. (2020). A crosslink constraint method for modeling episodic dynamic rupture on intersecting faults. *Seismological Research Letters*, *91*(2A), 1030–1041.

Meng, C., & Wang, H. (2018). A finite element and finite difference mixed approach for modeling fault rupture and ground motion. *Computers & Geosciences*, *113*, 54–69.

NAM. (2020). Petrel geological model of the Groningen gas field, the Netherlands. https://public.yoda.uu.nl/geo/UU01/1QH0MW.html

Okuwaki, R., Yagi, Y., & Hirano, S. (2014). Relationship between high-frequency radiation and asperity ruptures, revealed by hybrid back-projection with a non-planar fault model. *Scientific reports*, *4*(1), 7120.

Romijn, R. (2017). Groningen velocity model 2017—Groningen full elastic velocity model September 2017. *Technical Rept.*

Ross, Z. E., Idini, B., Jia, Z., Stephenson, O. L., Zhong, M., Wang, X., Zhan, Z., Simons, M., Fielding, E. J., Yun, S.-H., et al. (2019). Hierarchical interlocked orthogonal faulting in the 2019 Ridgecrest earthquake sequence. *Science*, *366*(6463), 346–351.

Ruan, J., Ghose, R., & Mulder, W. A. (2023). 3D geomechanical modeling of induced seismic slips considering realistic reservoir geometry with intersecting faults. *Authorea Preprints*.

Rudnicki, J., & Kanamori, H. (1981). Effects of fault interaction on moment, stress drop, and strain energy release. *Journal of Geophysical Research: Solid Earth*, *86*(B3), 1785–1793.

Ruina, A. (1983). Slip instability and state variable friction laws. *Journal of Geophysical Research: Solid Earth*, *88*(B12), 10359–10370.

Schmedes, J., & Archuleta, R. J. (2008). Near-source ground motion along strike-slip faults: Insights into magnitude saturation of pgv and pga. *Bulletin of the Seismological Society of America*, *98*(5), 2278–2290.

Spetzler, J., & Dost, B. (2017). Hypocentre estimation of induced earthquakes in Groningen. *Geophysical Journal International*, *209*(1), 453–465.

Uchida, N., & Matsuzawa, T. (2013). Pre-and postseismic slow slip surrounding the 2011 Tohoku-oki earthquake rupture. *Earth and Planetary Science Letters*, *374*, 81–91.

Uenishi, K., & Rice, J. R. (2003). Universal nucleation length for slip-weakening rupture instability under nonuniform fault loading. *Journal of Geophysical Research: Solid Earth*, *108*(B1).

Van den Bogert, P. A. J. (2018). *Depletion-induced fault slip and seismic rupture. 2D geomechanical models for the Groningen field, The Netherlands* (tech. rep.). Nederlandse Aardolie Maatschappij BV. Assen, The Netherlands. https://nam-onderzoeksrapporten.data-app.nl/reports/download/groningen/en/d77787dc-4e7d-4c1f-b6ee-eec29762c3b6

Van Wees, J.-D., Fokker, P. A., Van Thienen-Visser, K., Wassing, B. B., Osinga, S., Orlic, B., Ghouri, S. A., Buijze, L., & Pluymaekers, M. (2017). Geomechanical models for induced seismicity in the Netherlands: Inferences from simplified analytical, finite element and rupture model approaches. *Netherlands Journal of Geosciences*, *96*(5), s183–s202.

van Ginkel, J., Ruigrok, E., Stafleu, J., & Herber, R. (2022). Development of a seismic site-response zonation map for the netherlands. *Natural Hazards and Earth System Sciences*, *22*(1), 41–63. https://doi.org/10.5194/nhess-22-41-2022

Weng, H., & Yang, H. (2018). Constraining frictional properties on fault by dynamic rupture simulations and near-field observations. *Journal of Geophysical Research: Solid Earth*, *123*(8), 6658–6670.

Wentinck, H. (2018). *Dynamic modelling of large tremors in the Groningen field using extended seismic sources* (tech. rep.). Nederlandse Aardolie Maatschappij BV. Assen, The Netherlands. https://nam-onderzoeksrapporten.data-app.nl/reports/download/groningen/en/063425b3-f3e0-4c6f-9d85-c5fe6f0eca07

Willacy, C., van Dedem, E., Minisini, S., Li, J., Blokland, J.-W., Das, I., & Droujinine, A. (2019). Full-waveform event location and moment tensor inversion for induced seismicity. *Geophysics*, *84*(2), KS39–KS57.

Woo, J.-U., Kim, M., Sheen, D.-H., Kang, T.-S., Rhie, J., Grigoli, F., Ellsworth, W. L., & Giardini, D. (2019). An in-depth seismological analysis revealing a causal link between the 2017 Mw 5.5 Pohang earthquake and EGS project. *Journal of Geophysical Research: Solid Earth*, *124*(12), 13060–13078.

Yamashita, S., Yagi, Y., Okuwaki, R., Shimizu, K., Agata, R., & Fukahata, Y. (2021). Consecutive ruptures on a complex conjugate fault system during the 2018 Gulf of Alaska earthquake. *Scientific Reports*, *11*(1), 5979.

Yin, J., Yao, H., Yang, H., Liu, J., Qin, W., & Zhang, H. (2017). Frequency-dependent rupture process, stress change, and seismogenic mechanism of the 25 April 2015 Nepal Gorkha Mw 7.8 earthquake. *Science China Earth Sciences*, *60*, 796–808.

Zbinden, D., Rinaldi, A. P., Urpi, L., & Wiemer, S. (2017). On the physics-based processes behind production-induced seismicity in natural gas fields. *Journal of Geophysical Research: Solid Earth*, *122*(5), 3792–3812.

CURRICULUM VITÆ

Jingming RUAN (阮景明)

02-08-1994	Born in Guangdong, China.

EDUCATION

2019–2025	PhD in Geophysics Delft University of Technology, Netherlands *Thesis:* From Finite Fault Slip to Seismic moment tensor: Induced seismicity simulation and Moment Tensor Inversion *Promotor:* Dr. R. Ghose Prof. dr. W. A. Mulder
2017–2019	Master of Science in Earth Sciences Utrecht University, Netherlands
2012–2016	Bachelor of Science in Marine Science Sun Yat-sen University, China

LIST OF PUBLICATIONS

6. **J. Ruan**, R. Ghose, W. A. Mulder, *3D geomechanical modeling of induced seismic slips considering realistic reservoir geometry with intersecting faults*, ESS Open Archive, August 04, **2023**. (Under revision)

5. **J. Ruan**, R. Ghose, W. A. Mulder, *Fault intersection and induced seismicity: The effects on the induced stress field and the dynamic rupture, and their implications*, SEG Technical Program Expanded Abstracts, pp. 909–913 (**2023**).

4. **J. Ruan**, R. Ghose, W. A. Mulder, *3D geomechanical modelling of induced seismicity including intersecting faults and reservoir compartments*, 84th EAGE Annual Conference & Exhibition **2023**(1), 1–5.

3. M. Ravasi, **J. Ruan**, I. Vasconcelos, *Multichannel wavefield reconstruction using smooth slope information from multicomponent data*, 84th EAGE Annual Conference & Exhibition **2023**(1), 1–5.

2. **J. Ruan**, L. O. M. Masfara, R. Ghose, W. A. Mulder, *Linking geomechanical simulation of induced seismicity to surface seismic observations: Simulated finite fault rupture to moment tensor inversion*, SEG Technical Program Expanded Abstracts, pp. 1541–1545 (**2022**).

1. **J. Ruan**, I. Vasconcelos, *Data- and prior-driven sampling and wavefield reconstruction for sparse, irregularly-sampled, higher-order gradient data*, SEG Technical Program Expanded Abstracts, pp. 4515–4519 (**2019**).